Nuclear Astrophysics and Nuclei Far from Stability

Karlheinz Langanke[1], Friedrich-Karl Thielemann[2], and Michael Wiescher[3]

[1] Institute for Physics and Astronomy, University of Aarhus, 8000 Aarhus, Denmark,
[2] Department of Physics and Astronomy, University of Basel, 4056 Basel, Switzerland,
[3] Department of Physics, University of Notre Dame, IN 46556, USA

Abstract. This lecture concentrates on nucleosynthesis processes in stellar evolution and stellar explosions, with an emphasis on the role of nuclei far from stability. A brief initial introduction is given to the physics in astrophysical plasmas which governs composition changes. We present the basic equations for thermonuclear reaction rates, nuclear reaction networks and burning processes. The required nuclear physics input is discussed for cross sections of nuclear reactions, photodisintegrations, electron and positron captures, neutrino captures, inelastic neutrino scattering, and for beta-decay half-lives. We examine the present state of uncertainties in predictions in general as well as the status of experiments far from stability. It follows a discussion of the fate of massive stars, core collapse supernova explosions (SNe II), and novae and X-ray bursts (explosive hydrogen and helium burning on accreting white dwarfs or neutron stars in binary stellar systems). We address also the production of heavy elements in the r-process up to Th, U and beyond and their possible origin from stellar explosion sites.

1 Thermonuclear Rates and Reaction Networks

In this section we want to outline the essential features of thermonuclear reaction rates and nuclear reaction networks. This serves the purpose to define a unified terminology to be used throughout this lecture [105,106,76,326,10, 198].

1.1 Thermonuclear Reaction Rates

The nuclear cross section for a reaction between target j and projectile k is defined by

$$\sigma = \frac{\text{number of reactions per sec and target } j}{\text{flux of incoming projectiles } k} = \frac{r/n_j}{n_k v}. \tag{1}$$

The second equality holds for the case that the relative velocity between targets with the number density n_j and projectiles with number density n_k is constant and has the value v. Then r, the number of reactions per cm^3

K. Langanke, F.-K. Thielemann, M. Wiescher, Nuclear Astrophysics and Nuclei far from Stability, Lect. Notes Phys. **651**, 383–467 (2004)
http://www.springerlink.com/

and sec, can be expressed as $r = \sigma v n_j n_k$. More generally, when targets and projectiles follow specific distributions, r is given by

$$r_{j,k} = \int \sigma |\vec{v}_j - \vec{v}_k| d^3 n_j d^3 n_k. \tag{2}$$

The evaluation of this integral depends on the type of particles and distributions which are involved.

Maxwell-Boltzmann Distributions. For nuclei j and k in an astrophysical plasma, obeying a Maxwell-Boltzmann distribution,

$$d^3 n_j = n_j (\frac{m_j}{2\pi kT})^{3/2} \exp(-\frac{m_j v_j^2}{2kT}) d^3 v_j, \tag{3}$$

Equation (2) simplifies to $r_{j,k} =< \sigma v >_{j,k} n_j n_k$. The thermonuclear reaction rates have the form [105,76]

$$< j,k >:=< \sigma v >_{j,k}= (\frac{8}{\mu\pi})^{1/2} (kT)^{-3/2} \int_0^\infty E\sigma(E) \exp(-E/kT) dE. \tag{4}$$

Here μ denotes the reduced mass of the target-projectile system and the integral extends over the projectile energy range.

Experimental nuclear rates for light nuclei have been discussed in detail in many reviews for charged-particle reactions [327,99,65,411,5] as well as neutron captures [20,27,428,21]. Rates for unstable (light) nuclei came from a number of sources [246,247,414–417,419,420,418,400,380,381,310,336,173]. A survey of experimental approaches and efforts towards nuclei far from stability is given in Sect. 2.

For the vast number of medium and heavy nuclei which exhibit a high density of excited states at capture energies, Hauser-Feshbach (statistical model) calculations are applicable and have been available for some time [166, 430,371,80]. Improvements in level densities [311], alpha potentials, and the consistent treatment of isospin mixing has led to the next generation of theoretical rate predictions [313,312,130,315,266]. Some of it will be discussed Sect. 3.

In astrophysical plasmas with high densities and/or low temperatures, effects of electron screening become highly important. This means that the reacting nuclei, due to the background of electrons and nuclei, feel a different Coulomb repulsion than in the case of bare nuclei in a vacuum. Under most conditions (with non-vanishing temperatures) the generalized reaction rate integral can be separated into the traditional expression without screening (4) and a screening factor [332,184,141,3,185,175,178,179,379,118,186,343, 176,180,71,205,48,136,423,346]

$$< j,k >^* = f_{scr}(Z_j, Z_k, \rho, T, Y_i) < j,k > . \tag{5}$$

This screening factor is dependent on the charge of the involved particles, the density, temperature, and the composition of the plasma. Here Y_i denotes the abundance of nucleus i defined by $Y_i = n_i/(\rho N_A)$, where n_i is the number density of nuclei per unit volume and N_A Avogadro's number. At high densities and low temperatures screening factors can enhance reactions by many orders of magnitude and lead to *pycnonuclear ignition*. In the extreme case of very low temperatures, where reactions are only possible via ground state oscillations of the nuclei in a Coulomb lattice, (5) breaks down, because it was derived under the assumption of a Boltzmann distribution [118,186, 343,176,71,177,26,139].

Planck Distributions in Photodisintegrations. When in (2) particle k is a photon, the relative velocity is always c and quantities in the integral are not dependent on d^3n_j. Thus it simplifies to $r_j = \lambda_{j,\gamma} n_j$ and $\lambda_{j,\gamma}$ results from an integration of the photodisintegration cross section over a Planck distribution for photons of temperature T

$$d^3n_\gamma = \frac{1}{\pi^2(c\hbar)^3}\frac{E_\gamma^2}{\exp(E_\gamma/kT)-1}dE_\gamma \tag{6a}$$

$$r_j = \lambda_{j,\gamma}(T)n_j = \frac{\int d^3n_j}{\pi^2(c\hbar)^3}\int_0^\infty \frac{c\sigma(E_\gamma)E_\gamma^2}{\exp(E_\gamma/kT)-1}dE_\gamma. \tag{6b}$$

There exist a number of recent attempts to evaluate experimental photodisintegration cross sections and determine photodisintegration rates [273,274, 349,396]. Due to detailed balance, these rates can also be expressed by the capture cross sections for the inverse reaction $l + m \to j + \gamma$ [105] via

$$\lambda_{j,\gamma}(T) = (\frac{G_l G_m}{G_j})(\frac{A_l A_m}{A_j})^{3/2}(\frac{m_u kT}{2\pi\hbar^2})^{3/2} < l,m > \exp(-Q_{lm}/kT). \tag{7}$$

This expression depends on the reaction Q-value Q_{lm}, the inverse reaction rate $< l,m >$, the partition functions $G(T) = \sum_i(2J_i+1)\times\exp(-E_i/kT)$ and the mass numbers A of the participating nuclei in a thermal bath of temperature T.

Fermi Distributions in Weak Interactions. A procedure similar to (6) is used for electron captures on nuclei $e^- + (Z,A) \to (Z-1,A) + \nu_e$. Because the electron is about 2000 times less massive than a nucleon, the velocity of the nucleus j is negligible in the center of mass system in comparison to the electron velocity ($|\vec{v}_j - \vec{v}_e| \approx |\vec{v}_e|$) and the integral does not depend on d^3n_j. The electron capture cross section has to be integrated over a Boltzmann, partially degenerate, or Fermi distribution of electrons, dependent on the astrophysical conditions. The electron capture rates are a function of T and $n_e = Y_e\rho N_A$, the electron number density. In a neutral, completely ionized plasma, the electron abundance is equal to the total proton abundance in nuclei $Y_e = \sum_i Z_i Y_i$ and

$$r_j = \lambda_{j,e}(T, \rho Y_e) n_j . \tag{8}$$

Theoretical investigations extended from simpler approaches to full shell model calculations for the involved Gamow-Teller and Fermi transitions in weak interaction reactions [113–116,361,289,19,224,225]. The same authors generalized this treatment for the capture of positrons, which are in a chemical equilibrium with photons, electrons, and nuclei. Recent experimental results from charge-exchange reactions like $(d,{}^2\mathrm{He})$ show a good agreement with theory [16]. More details on results from modern shell model calculations are given in Sect. 4.1.

At high densities ($\rho > 10^{12}$ gcm^{-3}) the size of the neutrino scattering cross section on nuclei and electrons ensures that enough scattering events occur to thermalize a neutrino distribution. Then also the inverse process to electron capture (neutrino capture, i.e. charged-current neutrino scattering) can occur and the neutrino capture rate can be expresses similar to (6) or (8), integrating over the neutrino distribution [50,117,319,225]. Also (neutral current) inelastic neutrino scattering on nuclei can be expressed in this form. The latter can cause particle emission, like in photodisintegrations [431,208–210,305,319,334,221,212]. It is also possible that a thermal equilibrium among neutrinos was established at a different location than at the point where the reaction occurs. In such a case the neutrino distribution can be characterized by a chemical potential and a temperature which is not necessarily equal to the local temperature. Further discussions and results are presented in Sect. 4.2.

Decays. Finally, for normal decays, like beta or alpha decays with half-life $\tau_{1/2}$, we obtain an equation similar to (6) or (8) with a decay constant $\lambda_j = \ln 2/\tau_{1/2}$ and

$$r_j = \lambda_j n_j . \tag{9}$$

Beta-decay half-lives $\tau_{1/2}$ for unstable nuclei are either obtained from experiments or have been predicted theoretically in [362,206,363] and more recently [356,357,270,155,358,269,40,41] with improved quasi particle RPA calculations. For calculations in combination with electron capture rates see Sect. 4.1.

1.2 Nuclear Reaction Networks

The time derivative of the number densities of each of the species in an astrophysical plasma (at constant density) is governed by the different expressions for r, the number of reactions per cm^3 and s, as discussed above for the different reaction mechanisms which can change nuclear abundances

$$(\frac{\partial n_i}{\partial t})_{\rho=const} = \sum_j N^i_j r_j + \sum_{j,k} N^i_{j,k} r_{j,k} + \sum_{j,k,l} N^i_{j,k,l} r_{j,k,l}. \tag{10}$$

The reactions listed on the right hand side of the equation belong to the three categories of reactions: (1) decays, photodisintegrations, electron and positron captures and neutrino induced reactions ($r_j = \lambda_j n_j$), (2) two-particle reactions ($r_{j,k} =< j,k > n_j n_k$), and (3) three-particle reactions ($r_{j,k,l} =< j,k,l > n_j n_k n_l$) like the triple-alpha process, which can be interpreted as successive captures with an intermediate unstable target [287,127, 336]. The individual N^i's are given by: $N^i_j = N_i$, $N^i_{j,k} = N_i / \prod_{m=1}^{n_m} |N_{j_m}|!$, and $N^i_{j,k,l} = N_i / \prod_{m=1}^{n_m} |N_{j_m}|!$. The $N_i's$ can be positive or negative numbers and specify how many particles of species i are created or destroyed in a reaction. The denominators, including factorials, run over the n_m different species destroyed in the reaction and avoid double counting of the number of reactions when identical particles react with each other (for example in the $^{12}C+^{12}C$ or the triple-alpha reaction [105]). In order to exclude changes in the number densities $\dot{n}_i$, which are only due to expansion or contraction of the gas, the nuclear abundances $Y_i = n_i/(\rho N_A)$ were introduced. For a nucleus with atomic weight A_i, $A_i Y_i$ represents the mass fraction of this nucleus, therefore $\sum A_i Y_i = 1$. In terms of nuclear abundances Y_i, a reaction network is described by the following set of differential equations

$$\dot{Y}_i = \sum_j N^i_j \lambda_j Y_j + \sum_{j,k} N^i_{j,k} \rho N_A < j,k > Y_j Y_k$$
$$+ \sum_{j,k,l} N^i_{j,k,l} \rho^2 N_A^2 < j,k,l > Y_j Y_k Y_l. \tag{11}$$

Equation (11) derives directly from (10) when the definition for the $Y_i's$ is introduced. This set of differential equations is solved with a fully implicit treatment. Then the stiff set of differential equations can be rewritten ([304], §15.6) as difference equations of the form $\Delta Y_i/\Delta t = f_i(Y_j(t+\Delta t))$, where $Y_i(t+\Delta t) = Y_i(t) + \Delta Y_i$. In this treatment, all quantities on the right hand side are evaluated at time $t+\Delta t$. This results in a set of non-linear equations for the new abundances $Y_i(t+\Delta t)$, which can be solved using a multi-dimensional Newton-Raphson iteration procedure [159].

The total energy generation per gram, due to nuclear reactions in a time step Δt which changed the abundances by ΔY_i, is expressed in terms of the mass excess $M_{ex,i}c^2$ of the participating nuclei [17,18]

$$\Delta\epsilon = -\sum_i \Delta Y_i N_A M_{ex,i} c^2 \tag{12a}$$

$$\dot{\epsilon} = -\sum_i \dot{Y}_i N_A M_{ex,i} c^2. \tag{12b}$$

As noted above, the important ingredients to nucleosynthesis calculations are decay half-lives, electron and positron capture rates, photodisintegrations, neutrino induced reaction rates, and strong interaction cross sections. The determinations from either experiment or theory are discussed in detail in Sects. 2 through 4. For a number of explosive burning environments the understanding of nuclear physics far from stability and the knowledge of nuclear masses is a key ingredient [268,2,17,299,18]. In recent years new Hartree-Fock(-Bogoliubov) or relativistic mean field approaches are addressing this question [73,92,322,28,130,285,132,335,408]. Presently the FRDM model [268] still seems to provide the best reproduction of known masses [130].

1.3 Burning Processes in Stellar Environments

Nucleosynthesis calculations can in general be classified into two categories: (1) nucleosynthesis during hydrostatic burning stages of stellar evolution on long timescales and (2) nucleosynthesis in explosive events (with different initial fuel compositions, specific to the event). In the following we want to discuss shortly reactions of importance for both conditions and the major burning products.

Hydrostatic Burning Stages in Stellar Evolution. The main hydrostatic burning stages and most important reactions are:
H-burning: there are two alternative reaction sequences, the different pp-chains which convert ^{1}H into ^{4}He, initiated by $^1\mathrm{H}(p, e^+\nu_e)^2\mathrm{H}$, and the CNO cycle which converts ^{1}H into ^{4}He by a sequence of (p,γ) and (p,α) reactions on C, N, and O isotopes and subsequent beta-decays. The CNO isotopes are all transformed into ^{14}N, due to the fact that the reaction $^{14}\mathrm{N}(p,\gamma)^{15}\mathrm{O}$ is the slowest reaction in the cycle.
He-burning: the main reactions are the triple-alpha reaction $^4\mathrm{He}(2\alpha,\gamma)^{12}\mathrm{C}$ and $^{12}\mathrm{C}(\alpha,\gamma)^{16}\mathrm{O}$.
C-burning: $^{12}\mathrm{C}(^{12}\mathrm{C},\alpha)^{20}\mathrm{Ne}$ and $^{12}\mathrm{C}(^{12}\mathrm{C},p)^{23}\mathrm{Na}$. Most of the ^{23}Na nuclei will react with the free protons via $^{23}\mathrm{Na}(p,\alpha)^{20}\mathrm{Ne}$.
Ne-Burning: $^{20}\mathrm{Ne}(\gamma,\alpha)^{16}\mathrm{O}$, $^{20}\mathrm{Ne}(\alpha,\gamma)$ ^{24}Mg and $^{24}\mathrm{Mg}(\alpha,\gamma)^{28}\mathrm{Si}$. It is important that photodisintegrations start to play a role when $30kT \approx Q$ (as a rule of thumb), with Q being the Q-value of a capture reaction. For those conditions sufficient photons with energies $>Q$ exist in the high energy tail of the Planck distribution. As $^{16}\mathrm{O}(\alpha,\gamma)^{20}\mathrm{Ne}$ has an exceptionally small Q-value of the order 4 MeV, this relation holds true for $T > 1.5 \times 10^9$ K, which is the temperature for (hydrostatic) Ne-burning.
O-burning: $^{16}\mathrm{O}(^{16}\mathrm{O},\alpha)^{28}\mathrm{Si}$, $^{16}\mathrm{O}(^{16}\mathrm{O},p)^{31}\mathrm{P}$, and $^{16}\mathrm{O}(^{16}\mathrm{O},n)^{31}\mathrm{S}(\beta^+)^{31}\mathrm{P}$. Similar to carbon burning, most of the ^{31}P is destroyed by a (p,α) reaction to ^{28}Si.

Si-burning: Si-burning is initiated like Ne-burning by photodisintegration reactions which then provide the particles for capture reactions. It ends in an equilibrium abundance distribution around Fe (thermodynamic equilibrium). As this includes all kinds of Q-values (on the average 8-10 MeV for capture reactions along the valley of stability), this translates to temperatures in excess of 3×10^9 K, being larger than the temperatures for the onset of Ne-burning. In such an equilibrium (also denoted nuclear statistical equilibrium, NSE) the abundance of each nucleus is only governed by the temperature T, density ρ, its nuclear binding energy B_i and partition function $G_i = \sum_j (2J^i_j + 1)\exp(-E^i_j/kT)$

$$Y_i = (\rho N_A)^{A_i-1} \frac{G_i}{2^{A_i}} A_i^{3/2} (\frac{2\pi\hbar^2}{m_u kT})^{\frac{3}{2}(A_i-1)} \exp(B_i/kT) Y_p^{Z_i} Y_n^{N_i}, \qquad (13)$$

while fulfilling mass conservation $\sum_i A_i Y_i = 1$ and charge conservation $\sum_i Z_i Y_i = Y_e$ (the total number of protons equals the net number of electrons, which is usually changed only by weak interactions on longer timescales). This equation is derived from the relation between chemical potentials (for Maxwell-Boltzmann distributions) in a thermal equilibrium ($\mu_i = Z_i\mu_p + N_i\mu_n$), where the subscripts n and p stand for neutrons and protons. Intermediate quasi-equilibrium stages (QSE), where clusters of neighboring nuclei are in relative equilibrium via neutron and proton reactions, but different clusters have total abundances which are offset from their NSE values, are important during the onset of Si-burning before a full NSE is reached and during the freeze-out from high temperatures, which will be discussed in Sect. 5.

s-process: the slow neutron capture process leads to the build-up of heavy elements during core and shell He-burning, where through a series of neutron captures and beta-decays, starting on existing heavy nuclei around Fe, nuclei up to Pb and Bi can be synthesized. The neutrons are provided by a side branch of He-burning, $^{14}N(\alpha,\gamma)^{18}F(\beta^+)^{18}O(\alpha,\gamma)\,^{22}Ne(\alpha,n)^{25}Mg$. An alternative stronger neutron source in He-shell flashes is the reaction $^{13}C(\alpha,n)^{16}O$, which requires admixture of hydrogen and the production of ^{13}C via proton capture on ^{12}C and a subsequent beta-decay.

Extensive overviews exist over the major and minor reaction sequences in all burning stages in massive stars [11,369,438,10,157,165,314,148]. For less massive stars which burn at higher densities, i.e. experience higher electron Fermi energies, electron captures are already important in O-burning and lead to a smaller Y_e or larger neutron excess $\eta = \sum_i (N_i - Z_i) Y_i = 1 - 2Y_e$. For a general overview of the s-process see [196,197,428,120,199,62,398,399].

Most reactions in hydrostatic burning stages proceed through stable nuclei. This is simply explained by the long timescales involved. For a $25M_\odot$ star, which is relatively massive and therefore experiences quite short burning phases, this still amounts to: H-burning 7×10^6 y, He-burning 5×10^5 y, C-burning 600 y, Ne-burning 1 y, O-burning 180 d, Si-burning 1 d. Because all these burning stages are long compared to beta-decay half-lives, with a few exceptions of long-lived unstable nuclei, nuclei can decay back to stability before undergoing the next reaction. Examples of such exceptions are the s-process branchings with a competition between neutron captures and beta-decays of similar timescales [120,198].

Nuclear Burning in Explosive Events Many of the hydrostatic burning processes discussed above can occur also under explosive conditions at much higher temperatures and on shorter timescales (see Figs. 7 and 8 in Sect. 5). The major reactions remain still the same in many cases, but often the beta-decay half-lives of unstable products are longer than the timescales of the explosive processes under investigation. This requires in general the additional knowledge of nuclear cross sections for unstable nuclei.

Extensive calculations of *explosive carbon, neon, oxygen, and silicon burning*, appropriate for supernova explosions, have already been performed in the late 60s and early 70s with the accuracies possible in those days and detailed discussions about the expected abundance patterns [388,392]. The context of stellar models could only be given after their existence [389,9,438,377,165, 314,148].

Besides minor additions of ^{22}Ne after He-burning (or nuclei which originate from it in later burning stages), the fuels for explosive nucleosynthesis consist mainly of alpha-particle nuclei like ^{12}C, ^{16}O, ^{20}Ne, ^{24}Mg, or ^{28}Si. Because the timescale of explosive processing is very short (a fraction of a second to several seconds), in most cases only few beta-decays can occur during explosive nucleosynthesis events, resulting in heavier nuclei, again with N≈Z. However, even for a fuel with a total $N/Z \approx 1$ (or $Y_e \approx 0.5$) a spread of nuclei around a line of N=Z is involved and many reaction rates for unstable nuclei have to be known. Dependent on the temperature, explosive burning produces intermediate to heavy nuclei. We will discuss the individual burning processes in Sect. 5.

Two processes differ from the above scenario for initial fuel compositions with extreme overall N/Z-ratios, where either a large supply of neutrons or protons is available, the *r-process* and the *rp-process*, denoting rapid neutron or proton capture (the latter also termed *explosive hydrogen burning*). The proton supply in the rp-process results from the accretion of unburned H and He in novae and X-ray bursts [194,195,336,337]. Electron captures in supernova explosions of both types (Ia and II) can reduce Y_e drastically, i.e. enhance the overall N/Z ratio. Neutrino-induced reactions can act in addition in type II supernovae. The astrophysical site which provides the neutron-rich conditions for the r-process is still debated, involving type II supernovae or neutron star mergers [368,383]. In the r- or rp-process nuclei close to the neutron and proton drip lines can be prodruced and beta-decay timescales can be short in comparison to the process timescales.

2 Experimental Nuclear Astrophysics with Radioactive Beams

Experimental nuclear astrophysics provides reaction or decay data for simulating nucleosynthesis or energy generation patterns in stable or explosive stellar scenarios. These data are mostly determined in accelerator based experiments in the energy range between 6 keV and 60 GeV, depending on the goal of the experiment. Experimental nuclear astrophysics therefore uses an enormous range of challenging experimental techniques. While the field has been extremely successful over the last few decades in testing and confirming reaction and decay rate predictions for the astrophysics community, it also posed new questions and challenges for this field by determining experimentally reactions which had been neglected or ignored for general nucleosynthesis considerations. Presently experimental nuclear astrophysics is facing three major challenges,

- the study of very low energy reactions at stability to interpret charged particle induced nucleosynthesis processes during stellar evolution
- the measurement of neutron induced processes near stability for the understanding of the s-process
- the study of reaction and decay processes near and far from stability for interpretation of stellar explosion scenarios and the associated nucleosynthesis patterns.

The first subject is mainly concerned with nuclear reactions with charged particles of relevance for stellar hydrogen, helium, and carbon burning. While many of these reactions have been studied over the last four decades, most of the measurements were focused on energies well above the critical energy range of the Gamow window (see Sect. 2.1) because of the rapidly decreasing cross sections towards low energies. The presently used reaction rates (tabulated for example in the NACRE compilation [5]) are mostly based on extrapolation of the higher energy cross sections towards the Gamow range. This procedure can carry considerable uncertainty, in particular when unaccounted for near threshold states can contribute as resonances to the reaction rate. The measurement of neutron capture reactions is of relevance for the study of the s-process during stellar core He burning in massive stars ($M \geq 15 M_\odot$)(weak s-process) and in AGB stars ($M \leq 4 M_\odot$) (strong s-process) [62]. Most of the measurement have been done with the activation technique using neutron beams with an energy distribution simulating a 25 keV Maxwell Boltzmann distribution. New detector technology allowed to also perform in-beam γ spectroscopy [198]. These measurements were often handicapped by the need for large sample masses, which prohibited the study of neutron capture on rare isotopes. Alternative techniques were the use of electron beam induced pulsed neutron sources like ORELA with time of flight analysis [38]. The neutrons are produced by bremsstrahlung from a tantalum radiator. Neutron spallation sources like n-ToF at CERN provide higher intensity white neutron beams which now allow in combination with time of flight analysis to measure the neutron capture cross sections on considerably smaller samples of rare isotopes than previously possible. In this volume we will concentrate on the third item, the important experimental questions and challenges presented by the goal to study reactions or decay processes far off stability using radioactive beam techniques.

2.1 Relevant Energy Ranges for Cross Section Measurements

The nuclear reaction rate per particle pair at a given stellar temperature T is determined by folding the reaction cross section with the Maxwell-Boltzmann (MB) velocity distribution of the projectiles, as displayed in (4). Two cases have to be considered, reactions between charged particles and reactions with neutrons.

The nuclear cross section for charged particles is strongly suppressed at low energies due to the Coulomb barrier. For particles having energies less than the height of the Coulomb barrier, the product of the penetration factor and the MB distribution function at a given temperature results in the so-called Gamow peak, in which most of the reactions will take place. Location and width of the Gamow peak depend on the charges of projectile and target, and on the temperature of the interacting plasma.

When introducing the astrophysical S factor $S(E) = \sigma(E)E\exp(2\pi\eta)$ (with η being the Sommerfeld parameter, describing the s-wave barrier penetration), one can easily see the two contributions of the velocity distribution and the penetrability in the integral

$$< \sigma v >= \left(\frac{8}{\pi\mu}\right)^{1/2} \frac{1}{(kT)^{3/2}} \int_0^\infty S(E) \exp\left[-\frac{E}{kT} - \frac{b}{E^{1/2}}\right], \tag{14}$$

where the quantity $b = 2\pi\eta E^{1/2} = (2\mu)^{1/2}\pi e^2 Z_j Z_k/\hbar$ arises from the barrier penetrability. Taking the first derivative of the integrand yields the location E_0 of the Gamow peak, and the effective width Δ of the energy window can be derived accordingly

$$E_0 = \left(\frac{bkT}{2}\right)^{2/3} = 1.22(Z_j^2 Z_k^2 A T_6^2)^{1/3}\,\mathrm{keV}, \tag{15a}$$

$$\Delta = \frac{16E_0kT}{3}^{1/2} = 0.749(Z_j^2 Z_k^2 A T_6^5)^{1/6}\,\mathrm{keV}, \tag{15b}$$

as shown in [105] and [326], where the charges Z_j, Z_k, the reduced mass A of the involved nuclei in units of m_u, and the temperature T_6 given in 10^6 K, enter.

In the case of neutron-induced reactions the effective energy window has to be derived in a slightly different way. For s-wave neutrons ($l = 0$) the energy window is simply given by the location and width of the peak of the MB distribution function. For higher partial waves the penetrability of the centrifugal barrier shifts the effective energy E_0 to higher energies. For neutrons with energies less than the height of the centrifugal barrier this was approximated by [409]

$$E_0 \approx 0.172 T_9 \left(l + \frac{1}{2}\right) \quad \text{MeV}, \tag{16a}$$

$$\Delta \approx 0.194 T_9 \left(l + \frac{1}{2}\right)^{1/2} \text{MeV}. \tag{16b}$$

The energy E_0 will always be comparatively small in comparison to the neutron separation energy.

2.2 Radioactive Beams

Radioactive beam experiments are necessary for the measurement of reactions and decay processes of radioactive nuclei which can take place at the high temperatures, typical in explosive stellar events. At these conditions the Gamow window represents a much higher energy than for hydrostatic burning stages in stellar evolution. The reaction rates, which for charged particle interactions typically increase exponentially with temperature, become much larger than the decay rates and the reaction path runs far away from the line of stability. Nucleosynthesis simulations of explosive scenarios up to now are mostly based on theoretical predictions for capture and decay rates far off stability e.g. [312,269]. These theoretical input parameters need to be confirmed or complemented by reliable reaction and decay rate measurements. Within the last decade reaction measurements with radioactive beams have been successfully performed, simulating nuclear processes in the Big Bang and for explosive hydrogen and helium burning conditions typical for the thermonuclear runaway in accreting binary star systems or for explosive burning in supernova shock fronts. For neutron induced processes such as the r-process, the particular neutron capture reaction rates are less important since the r-process path is essentially determined by an (n,γ)-(γ,n) chemical equilibrium which depends on the nuclear masses. Therefore an increasing number of studies has focused on the global properties of neutron rich nuclei such as masses, half- lives and neutron decay probabilities. All these are important ingredients for r-process nucleosynthesis models. Neutron capture rates itself will be difficult if not impossible to measure but recent activities focus on the study of neutron transfer measurements on radioactive neutron rich isotopes instead to probe the level density and single particle structure of neutron unbound states in nuclei towards the r-process path [75].

ISOL Facilities. The development of clean radioactive beams presents an enormous technical challenge. For most of the low energy experiments mentioned below, the so-called ISOL technique was applied where the radioactive beam particles were produced by nuclear reactions or spallation processes with high energy primary stable beams in a production target. The fast release of the produced radioisotopes is important for achieving high beam intensities but requires optimization of the chemical and physical characteristics of the isotope/target combination. The released isotopes need to be separated by electric and magnetic mass/charge separation systems and post-accelerated up to the required beam energies. ISOL facilities (like e.g. Louvain-la-Neuve, CERN-Isolde, the Oak-Ridge Holifield Facility) have been used over the years as an excellent tool for the production of radioactive isotopes for decay measurements along the r-process and the rp-process path [217,151]. Capture measurements with radioactive beams in inverse kinematics are among the major goals for radioactive beam facilities. The first pioneering measurements on university based radioactive beam facilities operated with limited beam intensities (on average $\leq 10^7$ ions/s with some beams reaching exceptional intensities of up to 10^9 ions/s). These limitations are due to the cross sections of production reactions, the release time for the radioactive species in the production target and finally the chemistry conditions in the ion source. The experiments were also handicapped by insufficient detector systems with relatively low detection efficiency and limited background reduction capabilities. Nevertheless, these first attempts proved that radioactive beam experiments for nuclear astrophysics can be successfully performed and can provide important data for the nuclear astrophysics community. With the above constraints in mind, only reactions with high cross sections have been successfully measured such as ^{13}N(p,γ)[88], ^{8}Li(α,n) [137], ^{18}F(p,α) [133,320,23], and ^{18}Ne(α,p) [45,135]. The experimental conditions in terms of detector development have improved continuously. The increasing use of large Si-array strip detector systems for low energy (p,α) and (α,p) experiments such as LEDA [86] was a breakthrough in terms of efficiency and solid angle and helped to compensate for the limited beam intensities available. The use of these detectors allowed to investigate resonance states for capture reactions through elastic resonance scattering if the resonance capture cross section was too low for a direct measurement. These elastic scattering studies were in particular successful for ^{17}F(p,p) where they helped to uniquely identify the energy of a missing resonance state [22]. Experimental conditions have been further improved by the design and utilization of recoil-mass-separators. These guarantee a $\leq 10^{-12}$ rejection of the primary beam and further background reduction by particle identification methods while maintaining a high detection efficiency. This was clearly demonstrated in the first successful experiment of low energy resonances in ^{21}Na(p,γ) with the DRAGON separator [36]. Recoil mass separators are also now being commissioned or constructed at other low energy radioactive ion beam facilities such as HRIBF [188] and Louvain la Neuve [78]. These, coupled to a powerful γ-detection array will dominate the future measurements with low energy radioactive beams. A new generation of ISOL based radioactive beam facilities is emerging with the ISAC facility at TRIUMF, Rex-Isolde at CERN, and Spiral at GANIL. They will hopefully provide higher beam intensities of up to 10^{10}-10^{12} atoms/s, depending on the chemical and physical characteristics of the isotope. Optimization of beam intensity mainly requires new and innovative developments in target technology to reduce the ionization and extraction times of the radioactive isotopes. The first capture reaction measurement of ^{21}Na(p,γ) has been successfully completed at ISAC using a surface ionization source [36]. This experiment concentrated on the measurement of two low energy resonances at 205 keV and 821 keV. In particular the lower energy resonance controls the reaction rate at nova temperatures and is therefore critical for the understanding of the production of the long-lived radionuclide ^{22}Na in novae. Future measurements of ^{19}Ne(p,γ) and ^{18}Ne(α,p) are planned using an ECR source. These reactions are closely associated with the break-out from the hot CNO cycles [422] which will be discussed in Sects. 5.1 and 8. Previous attempts at Louvain la Neuve were successful in developing the experimental technique and in measuring the higher energy resonances [294,397]. The study of the resonances within the Gamow range of X-ray burst conditions (see Sect. 8) requires higher beam intensities and novel detection and background reduction schemes to improve over the previously determined upper limits. Similar experiments are planned at Rex-Isolde like the study of resonances in ^{35}Ar(p,γ)^{36}K, a reaction that controls the reaction flow in high temperature novae burning and may limit the production of ^{40}Ca in novae [173]. A simple but efficient technique is the so-called in-beam production of radioactive isotopes which has been the backbone of the radioactive beam programs at Notre Dame and Argonne. The radioactive particles are produced by heavy ion nuclear reactions and separated from the primary beam in flight by the magnetic field structure of superconducting solenoids [230]. The energy of the secondary beam is mainly determined by the kinematics of the production process. The beam intensity is typically limited depending on the cross section of the production process.

In-Flight Separators. In-flight separators present an alternative approach for the production of neutron–rich or neutron–deficient radioactive isotopes between the region of stability and the neutron or proton drip–line. They are mainly based on separating (in flight) high energy radioactive heavy ion reaction or fission products through mass separator systems from the primary beam component (see also the lecture by Morrissey and Sherrill). Depending on magnetic, electric, and absorption conditions in the separator a so-called cocktail beam is produced at the focal plane which consists of particle groups within a certain A,Z range. The various cocktail components are identified by a subsequent energy, energy-loss analysis. Due to the large momentum transfer in the initial production process these beams have a fairly high energy and are typically used for mass or half–life measurements [427,241]. Increasingly also transfer reactions (on stable and radioactive beams) are performed to study the evolution of nuclear structure far from stability. Such nuclear structure results are extremely important since they often provide important complementary information for determining the reaction rates along the r– or rp–process path (e.g. [75,63,321]). Important impact for the description of the r-process but also the rp-process has been provided by the measurements of β-decay or β-delayed particle decay (emission) processes along the process path. In particular these measurements presented a major challenge for studying β^--decays and β-delayed neutron emission for r-process nuclei which were typically located far from stability. In most of these cases the isotopes of interest were separated by ISOL or in-flight separator techniques and implanted into periodically moving tapes to be detected off-line. Pulsed beam techniques from in-flight separator facilities typically implanted the separated short-lived particles into a stack of Si-detectors after particle identification to monitor the decay on-line. These measurement may provide a more sensitive approach for identifying radioactive isotopes far off stability and for reducing the background which often limited the accessibility to very neutron rich isotopes at ISOL beam facilities. Those measurements were often handicapped by background from long lived daughter activities of isobaric impurities in the separated particle groups. Only in a few cases direct measurements on r-process nuclei have been sucessfull like the study of ^{130}Cd in 1986 at ISOLDE/CERN [215], which later could be significantly improved with the use of better isobar separation [91,140]. In particular the development and use of laser ion sources opened new opportunities for removing isobaric impurities from the beam, reducing this kind of background enormously [140,347]. Fragment separator beams have been used in particular for life time and decay studies of radioactive nuclei near the rp-process or r-process path. The high energy radioactive isotopes are directly implanted into stacks of Si detectors or into moving tape systems to measure the accumulated activity off-line. In the recent past in-flight separators have been successfully used to map both masses and life times near the proton drip line. In particular the systematic study of lifetimes in the mass A=35 to 65 along the drip line [241] has provided important information for rp-process simulations and put the previously used theoretical estimates on firm experimental ground. Detailed studies at NSCL/MSU, ORNL and GANIL have focused on the N=Z nuclei above A=64 to investigate the waiting point nuclei ^{64}Ge, ^{68}Se, and ^{72}Kr up to ^{80}Zr [427,325]. These measurements did focus mainly on the lifetime and decay properties of these isotopes but provided also important information about the masses through β-decay endpoint measurements. The use of traps can and will considerably improve the accuracy of such studies in the near future [39,152]. While most of the measurements near the r-process path have been performed at ISOL based facilities, the upgrade of in-flight separator facilities like the coupled cyclotron facility at NSCL/MSU opened new opportunities to provide access to r-process nuclei, first measurements have been successfully completed in the lower mass range of the r-process (e.g. [250]), preferably in the study of the decay properties of neutron rich Ni isotopes. These measurements concentrated both on the study of the β decay as well as the β-delayed neutron decay properties of these isotopes. In view of the recent successes of γ-ray astronomy [342] and the anticipated results of the recently launched new INTEGRAL observatory, life time measurements of long-lived isotopes which contribute to the observed galactic radioactivity are of particular importance. These kind of measurements have been tedious with classical radiochemical methods and have been haunted by considerable experimental uncertainties. The on-line production and counting of long-lived radioactive isotopes at in-flight separator facilities provides an alternative experimental tool to reduce the uncertainties considerably [128]. This laboratory information does provide an important test for model predictions about the actual production rates for long-lived radioactive nuclei in the associated nucleosynthesis event. High energy radioactive beams from in-flight separators are obviously not usable for low energy capture measurements. But they have been used for Coulomb dissociation studies to obtain the capture cross section by applying the detailed balance theorem (7). In particular measurements of ^{8}B(γ,p)^{7}Be have been performed at Notre Dame [207], Riken [276], GSI Darmstadt [344], and the NSCL at Michigan State University [83] to determine the ^{7}Be(p,γ)^{8}B reaction rate. This reaction is critical for the production of high energy neutrinos in our sun and the rate is important for determining the neutrino oscillation parameters [341]. Coulomb dissociation was successfully applied for cases were the cross section was dominated by a single resonance like in ^{13}N(p,γ)^{14}O [203,277] or the direct capture like in ^{7}Be(p,γ)^{8}B, but the interpretation of the Coulomb dissociation spectrum becomes difficult as soon as several resonance and/or reaction components contribute. It also requires a strong known ground state transition branch of the resonance decay for converting correctly the cross section by detailed balance.

3 Cross Section Predictions and Reaction Rates

Explosive nuclear burning in astrophysical environments produces unstable nuclei, which again can be targets for subsequent reactions. In addition, it involves a very large number of stable nuclei, which are not and cannot be fully explored by experiments. Thus, it is necessary to be able to predict reaction cross sections and thermonuclear rates with the aid of theoretical models. Explosive burning in supernovae involves in general intermediate mass and heavy nuclei. Due to a large nucleon number they have intrinsically a high density of excited states. A high level density in the compound nucleus at the appropriate excitation energy allows to make use of the statistical model approach for compound nuclear reactions [143,245,119] which averages over resonances. Here, we want to present recent results obtained within this approach and outline in a clear way, where in the nuclear chart and for which environment temperatures its application is valid. It is often colloquially termed that the statistical model is only applicable for intermediate and heavy nuclei. However, the only necessary condition for its application is a large number of resonances at the appropriate bombarding energies, so that the cross section can be described by an average over resonances. This can in specific cases be valid for light nuclei and on the other hand not be valid for intermediate mass nuclei near magic numbers.

In astrophysical applications usually different aspects are emphasized than in pure nuclear physics investigations. Many of the latter in this long and well established field were focused on specific reactions, where all or most "ingredients", like optical potentials for particle and alpha transmission coefficients, level densities, resonance energies and widths of giant resonances to be implemented in predicting E1 and M1 gamma-transitions, were deduced from experiments. This of course, as long as the statistical model prerequisites are met, will produce highly accurate cross sections. For the majority of nuclei in astrophysical applications such information is not available. The real challenge is thus not the well established statistical model, but rather to provide all these necessary ingredients in as reliable a way as possible, also for nuclei where none of such informations are available. In addition, these approaches should be on a similar level as e.g. mass models, where the investigation of hundreds or thousands of nuclei is possible with managable computational effort.

The statistical model approach has long been employed in calculations of thermonuclear reaction rates for astrophysical purposes [393,264,265,390], who in the beginning only made use of ground state properties. Later, the importance of excited states of the target was pointed out by [12]. The compilations by [166,430,371,80,312] permitted large scale applications in all subfields of nuclear astrophysics, when experimental information is unavailable. Existing global optical potentials, mass models to predict Q-values, deformations etc., but also the ingredients to describe giant resonance properties have been quite successful in the past [80,311,130].

Besides necessary improvements in global alpha potentials [272,315,90], the major remaining uncertainty in all existing calculations stems from the prediction of nuclear level densities, which in earlier calculations gave uncertainties even beyond a factor of 10 at the neutron separation energy [122], about a factor of 8 [430], and a factor of 5 [371] [see Fig. 3.16 in [80]]. In nuclear reactions the transitions to lower lying states dominate due to the strong energy dependence. Because the deviations are usually not as high yet at lower excitation energies, the typical cross section uncertainties amounted to a smaller factor of 2–3.

Novel treatments for level density descriptions [182,181], where the level density parameter is energy dependent and shell effects vanish at high excitation energies, improves the level density accuracy. This is still a phenomenological approach, making use of a back-shifted Fermi-gas model rather than a combinatorial approach based on microscopic single-particle levels. But it was the first one leading to a reduction of the average cross section uncertainty to a factor of about 1.4, i.e. an average deviation of about 40% from experiments, when only employing global predictions for all input parameters and no specific experimental knowledge [311]. As shown by a number of authors [300,293], the combinatorial approach is equivalent to a back-shifted Fermi gas, provided the parameters are determined from consistent physics. Thus, it is not surprising that fully microscopic approaches [89] give similar uncertainties.

3.1 Thermonuclear Rates from Statistical Model Calculations

A high level density in the compound nucleus permits to use averaged transmission coefficients T, which do not reflect a resonance behavior, but rather describe absorption via an imaginary part in the (optical) nucleon-nucleus potential [245]. This leads to the well known expression

$$\sigma_i^{\mu\nu}\,(j,o;E_{ij}) = \frac{\pi\hbar^2/(2\mu_{ij}E_{ij})}{(2J_i^\mu+1)(2J_j+1)} \times \sum_{J,\pi}(2J+1)\frac{T_j^\mu(E,J,\pi,E_i^\mu,J_i^\mu,\pi_i^\mu)T_o^\nu(E,J,\pi,E_m^\nu,J_m^\nu,\pi_m^\nu)}{T_{tot}(E,J,\pi)} \quad (17)$$

for the reaction $i^\mu(j,o)m^\nu$ from the target state i^μ to the exited state m^ν of the final nucleus, with a center of mass energy E_{ij} and reduced mass μ_{ij}. J denotes the spin, E the corresponding excitation energy in the compound nucleus, and π the parity of excited states. When these properties are used without subscripts they describe the compound nucleus, subscripts refer to states of the participating nuclei in the reaction $i^\mu(j,o)m^\nu$ and superscripts indicate the specific excited states. Experiments measure $\sum_\nu \sigma_i^{0\nu}(j,o;E_{ij})$, summed over all excited states of the final nucleus, with the target in the ground state. Target states μ in an astrophysical plasma are thermally populated and the astrophysical cross section $\sigma_i^*(j,o)$ is given by

$$\sigma_i^*(j,o;E_{ij}) = \frac{\sum_\mu(2J_i^\mu+1)\exp(-E_i^\mu/kT)\sum_\nu\sigma_i^{\mu\nu}(j,o;E_{ij})}{\sum_\mu(2J_i^\mu+1)\exp(-E_i^\mu/kT)} \quad . \quad (18)$$

The summation over ν replaces $T_o^\nu(E,J,\pi)$ in (17) by the total transmission coefficient

$$T_o(E,J,\pi) = \sum_{\nu=0}^{\nu_m} T_o^\nu(E,J,\pi,E_m^\nu,J_m^\nu,\pi_m^\nu) + \int_{E_m^{\nu_m}}^{E-S_{m,o}} \sum_{J_m,\pi_m} T_o(E,J,\pi,E_m,J_m,\pi_m)\rho(E_m,J_m,\pi_m)dE_m \quad . \quad (19)$$

Here $S_{m,o}$ is the channel separation energy, and the summation over excited states above the highest experimentally known state ν_m is changed to an integration over the level density ρ. The summation over target states μ in (18) has to be generalized accordingly. It should also be noted at this point that the formulation given here assumes complete mixing of isospin. For reactions with $N = Z \pm 1$, i.e. isospin 0 or $\pm 1/2$ targets, deviations are observed but can be well reproduced in an appropriate approach [312].

In addition to the ingredients required for (17), like the transmission coefficients for particles and photons, width fluctuation corrections $W(j, o, J, \pi)$ have to be employed. They define the correlation factors with which all partial channels for an incoming particle j and outgoing particle o, passing through the excited state (E, J, π), have to be multiplied. This takes into account that the decay of the state is not fully statistical, but some memory of the way of formation is retained and influences the available decay choices. The major effect is elastic scattering, the incoming particle can be immediately re-emitted before the nucleus equilibrates. Once the particle is absorbed and not re-emitted in the very first (pre-compound) step, the equilibration is very likely. This corresponds to enhancing the elastic channel by a factor W_j. In order to conserve the total cross section, the individual transmission coefficients in the outgoing channels have to be renormalized to T'_j. The total cross section is proportional to T_j and, when summing over the elastic channel ($W_j T'_j$) and all outgoing channels ($T'_{tot} - T'_j$), one obtains the condition $T_j = T'_j(W_j T'_j / T'_{tot}) + T'_j(T'_{tot} - T'_j)/T'_{tot}$. We can (almost) solve for T'_j

$$T'_j = \frac{T_j}{1 + T'_j(W_j - 1)/T'_{tot}} \quad . \tag{20}$$

This requires an iterative solution for T' (starting in the first iteration with T_j and T_{tot}), which converges fast. The enhancement factor W_j has to be known in order to apply (20). A general expression in closed form was derived by [402], but is computationally expensive to use. A fit to results from Monte Carlo calculations by [366] gave

$$W_j = 1 + \frac{2}{1 + T_j^{1/2}} \quad . \tag{21}$$

For a general discussion of approximation methods see [119] and [96]. Equations (20) and (21) redefine the transmission coefficients of (17) in such a manner that the total width is redistributed by enhancing the elastic channel and weak channels over the dominant one. Cross sections near threshold energies of new channel openings, where very different channel strengths exist, can only be described correctly when taking width fluctuation corrections into account. The width fluctuation corrections of [366] are only an approximation to the correct treatment. However, [382] showed that they are quite adequate.

The important ingredients of statistical model calculations as indicated in (17) through (19) are the particle and gamma-transmission coefficients T and the level density of excited states ρ. Therefore, the reliability of such calculations is determined by the accuracy with which these components can be evaluated (often for unstable nuclei). In the following we want to discuss the methods utilized to estimate these quantities and recent improvements.

Transmission Coefficients. The transition from an excited state in the compound nucleus (E, J, π) to the state $(E_i^\mu, J_i^\mu, \pi_i^\mu)$ in nucleus i via the emission of a particle j is given by a summation over all quantum mechanically allowed partial waves

$$T_j^\mu(E, J, \pi, E_i^\mu, J_i^\mu, \pi_i^\mu) = \sum_{l=|J-s|}^{J+s} \sum_{s=|J_i^\mu - J_j|}^{J_i^\mu + J_j} T_{j_{ls}}(E_{ij}^\mu). \tag{22}$$

Here the angular momentum $\vec{l}$ and the channel spin $\vec{s} = \vec{J}_j + \vec{J}_i^\mu$ couple to $\vec{J} = \vec{l} + \vec{s}$. The transition energy in channel j is $E_{ij}^\mu = E - S_j - E_i^\mu$.

The individual particle transmission coefficients T_l are calculated by solving the Schrödinger equation with an optical potential for the particle-nucleus interaction. All early studies of thermonuclear reaction rates by [393,265, 12,390,166], and [430] employed optical square well potentials and made use of the black nucleus approximation. Reference [371] employed the optical potential for neutrons and protons [192], based on microscopic infinite nuclear matter calculations for a given density, applied with a local density approximation. However, a specific set obtained from fits to low energies was employed rather than the set given in that paper. This is similar to recent reevaluations [25]. Also included were corrections of the imaginary part by [97] and [244]. The resulting s-wave neutron strength function $< \Gamma^o/D > |_{1\mathrm{eV}} = (1/2\pi) T_{n(l=0)}(1\mathrm{eV})$ is shown and discussed in [373] and [80], where several phenomenological optical potentials of the Woods-Saxon type and the equivalent square well potential used in earlier astrophysical applications are compared. The purely theoretical approach gives the best fit. It is also expected to have the most reliable extrapolation properties for unstable nuclei. Reference [165] shows the ratio of the s-wave strength functions for the Jeukenne, Lejeune, and Mahaux potential over the black nucleus, equivalent square well approach for different energies. A general overview on different approaches can be found in [401].

Deformed nuclei were treated in a very simplified way by using an effective spherical potential of equal volume, based on averaging the deformed potential over all possible angles between the incoming particle and the orientation of the deformed nucleus. In most earlier compilations alpha particles were also treated by square well optical potentials. [371] employed a phenomenological Woods-Saxon potential by [249], based on extensive data from [243]. In general, for alpha particles and heavier projectiles, the best results can probably be obtained with folding potentials [272,315,90,14].

The gamma-transmission coefficients have to include the dominant gamma-transitions (E1 and M1) in the calculation of the total photon width. The smaller, and therefore less important, M1 transitions have usually been treated with the simple single particle approach $T \propto E^3$ of [37], as also discussed in [166]. The E1 transitions are usually calculated on the basis of the Lorentzian representation of the Giant Dipole Resonance (GDR). Within this model, the E1 transmission coefficient for the transition emitting a photon of energy E_γ in a nucleus ${}^A_N Z$ is given by

$$T_{E1}(E_\gamma) = \frac{8}{3} \frac{NZ}{A} \frac{e^2}{\hbar c} \frac{1+\chi}{mc^2} \sum_{i=1}^{2} \frac{i}{3} \frac{\Gamma_{G,i} E_\gamma^4}{(E_\gamma^2 - E_{G,i}^2)^2 + \Gamma_{G,i}^2 E_\gamma^2} \quad . \tag{23}$$

Here $\chi(= 0.2)$ accounts for the neutron-proton exchange contribution and the summation over i includes two terms which correspond to the split of the GDR in statically deformed nuclei, with oscillations along (i=1) and perpendicular (i=2) to the axis of rotational symmetry. Many microscopic and macroscopic models have been devoted to the calculation of the GDR energies (E_G) and widths (Γ_G). Analytical fits as a function of A and Z were also used, e.g. in [166] and [430]. [371] employed the (hydrodynamic) droplet model approach by [280] for E_G, which gives an excellent fit to the GDR energies and can also predict the split of the resonance for deformed nuclei, when making use of the deformation, calculated within the droplet model. In that case, the two resonance energies are related to the mean value calculated by the relations $E_{G,1} + 2E_{G,2} = 3E_G$, $E_{G,2}/E_{G,1} = 0.911\eta + 0.089$ of [82]. η is the ratio of the diameter along the nuclear symmetry axis to the diameter perpendicular to it, and can be obtained from the experimentally known deformation or mass model predictions. Reference [80] also gives a detailed description of the microscopic-macroscopic approach utilized to calculate Γ_G, based on dissipation and the coupling to quadrupole surface vibrations. This is the method applied to predict the gamma-transmission coefficients for the cross section determinations of [312]. An important aspect of the E1 strength is related to so-called pygmy resonances at low energies, not following the Lorentzian distribution [442]. This behavior is under investigation in microscopic treatments, i.e. within relativistic mean field approaches [406,407,285]. The connection of energy and strength of the pygmy resonance as a function of isospin and neutron skin of nuclei is still not fully understood. A full microscopic treatment with large scale QRPA calculations for the E1 strength has also been performed [129] and implemented in statistical model calculations. The accuracy of the extrapolations towards the driplines depends, similar to mass predictions, on the quality of the microscopic model applied.

Level Densities. While the method as such is well seasoned, considerable effort has been put into the improvement of the input for statistical Hauser-Feshbach models. However, the nuclear level density has given rise to the largest uncertainties in cross section determinations of [166,371,80]. For large scale astrophysical applications it is also necessary to not only find reliable methods for level density predictions, but also computationally feasible ones.

Such a model is the non-interacting Fermi-gas model. Most statistical model calculations use the back-shifted Fermi-gas description of [122]. More sophisticated Monte Carlo shell model calculations, e.g. by [87], as well as combinatorial approaches [293], have shown excellent agreement with this phenomenological approach and justified the application of the Fermi-gas description at and above the neutron separation energy. Rauscher, Thielemann, and Kratz [311] applied an energy-dependent level density parameter a together with microscopic corrections from nuclear mass models, which led to improved fits in the mass range $20 \leq A \leq 245$.

The back-shifted Fermi-gas description of [122] assumes an even distribution of odd and even parities.

$$\rho(U,J,\pi) = \frac{1}{2}\mathcal{F}(U,J)\rho(U), \tag{24}$$

with

$$\rho(U) = \frac{1}{\sqrt{2\pi}\sigma}\frac{\sqrt{\pi}}{12a^{1/4}}\frac{\exp(2\sqrt{aU})}{U^{5/4}}\,, \quad \mathcal{F}(U,J) = \frac{2J+1}{2\sigma^2}\exp\left(\frac{-J(J+1)}{2\sigma^2}\right) \tag{25}$$
$$\sigma^2 = \frac{\Theta_{\mathrm{rigid}}}{\hbar^2}\sqrt{\frac{U}{a}}\,, \qquad \Theta_{\mathrm{rigid}} = \frac{2}{5}m_{\mathrm{u}}AR^2\,, \qquad U = E - \delta \quad .$$

The spin dependence $\mathcal{F}$ is determined by the spin cut-off parameter σ. Thus, the level density is dependent on only two parameters: the level density parameter a and the backshift δ, which determines the energy of the first excited state.

Within this framework, the quality of level density predictions depends on the reliability of systematic estimates of a and δ. The first compilation for a large number of nuclei was provided by [122]. They found that the backshift δ is well reproduced by experimental pairing corrections [69]. They also were the first to identify an empirical correlation with experimental shell corrections $S(Z,N)$

$$\frac{a}{A} = c_0 + c_1 S(Z,N), \tag{26}$$

where $S(Z,N)$ is negative near closed shells. The back-shifted Fermi-gas approach diverges for $U=0$ (i.e. $E=\delta$, if δ is a positive backshift). In order to obtain the correct behavior at very low excitation energies, the Fermi-gas description can be combined with the constant temperature formula ([122], [119] and references therein)

$$\rho(U) \propto \frac{\exp(U/T)}{T} \quad . \tag{27}$$

The two formulations are matched by a tangential fit determining T. There have been a number of compilations for a and δ, or T, based on experimental level densities, as e.g. [403,404]. An improved approach has to consider the energy dependence of the shell effects, which are known to vanish at high excitation energies, see e.g. [182]. Although, for astrophysical purposes only energies close to the particle separation thresholds have to be considered, an energy dependence can lead to a considerable improvement of the global fit. This is especially true for strongly bound nuclei close to magic numbers. An excitation-energy dependent description was initially proposed by [181] for the level density parameter a

$$a(U,Z,N) = \tilde{a}(A)\left[1 + C(Z,N)\frac{f(U)}{U}\right] \tag{28a}$$

$$\tilde{a}(A) = \alpha A + \beta A^{2/3} \tag{28b}$$

$$f(U) = 1 - \exp(-\gamma U). \tag{28c}$$

The values of the free parameters α, β and γ are determined by fitting to experimental level density data available over the whole nuclear chart. The shape of the function $f(U)$ permits the two extremes: (i) for small excitation energies the original form of (26) $a/A = \alpha + \alpha\gamma C(Z,N)$ is retained with $S(Z,N)$ being replaced by $C(Z,N)$, (ii) for high excitation energies a/A approaches the continuum value α, obtained for infinite nuclear matter. In both cases β was neglected, which is realistic as discussed below. Previous attempts to find a global description of level densities used shell corrections S derived from comparison of liquid-drop masses with experiment ($S \equiv M_{\rm exp} - M_{\rm LD}$) or the "empirical" shell corrections $S(Z,N)$ given by [122]. A problem connected with the use of liquid-drop masses arises from the fact that there are different liquid-drop model parametrizations available in the literature which produce quite different values for S [255]. However, in addition, the meaning of the correction parameter inserted into the level density formula (28a) has to be reconsidered. The fact that nuclei approach a spherical shape at high excitation energies (temperatures) has to be included. Therefore, the correction parameter C should describe properties of a nucleus differing from the *spherical* macroscopic energy and contain those terms which are finite for low and vanishing at higher excitation energies. The latter requirement is mimicked by the form of (28a). Therefore, the parameter $C(Z,N)$ should rather be identified with the so-called "microscopic" correction $E_{\rm mic}$ than with the shell correction. The mass of a nucleus with deformation ϵ can then be written in two ways

$$M(\epsilon) = E_{\rm mic}(\epsilon) + E_{\rm mac}(\text{spherical}) \tag{29a}$$

$$M(\epsilon) = E_{\rm mac}(\epsilon) + E_{\rm s+p}(\epsilon), \tag{29b}$$

with $E_{\rm s+p}$ being the shell-plus-pairing correction. This confusion about the term "microscopic correction", being sometimes used in an ambiguous way, is also pointed out in [268]. The above mentioned ambiguity follows from the inclusion of deformation-dependent effects into the macroscopic part of the mass formula. Another important ingredient is the pairing gap Δ, related to the backshift δ. Instead of assuming constant pairing as in [323] or an often applied fixed dependence on the mass number via e.g. $\pm 12/\sqrt{A}$, the pairing gap Δ can be determined from differences in the binding energies (or mass differences, respectively) of neighboring nuclei [413].

$$\Delta_{\mathrm{n}}(Z,N) = \frac{1}{2}\left[M(Z,N-1) + M(Z,N+1) - 2M(Z,N)\right], \qquad (30)$$

where Δ_{n} is the neutron pairing gap and $M(Z,N)$ the ground state mass excess of the nucleus (Z,N). Similarly, the proton pairing gap Δ_{p} can be calculated.

This is still a phenomenological rather than a combinatorial approach based on microscopic single-particle levels. As shown by a number of authors [300,293], the combinatorial approach is equivalent to a back-shifted Fermi gas, provided the parameters are determined from consistent physics. Thus, it is not surprising that fully microscopic approaches [89] give similar uncertainties. An important effect at low excitation energies can come from the parity distribution of levels, deviating from the the assumption entering (24). Recent results [284,266,267] are presently implemented into upcoming reaction rate predictions.

Results. Reference [312] utilized the microscopic corrections of the Finite Range Droplet Model FRDM mass formula [268], (using a folded Yukawa shell model with Lipkin-Nogami pairing) in order to determine the parameter $C(Z,N)$=E_{mic}. The backshift δ was calculated by setting $\delta(Z,N)$= $1/2\{\Delta_{\mathrm{n}}(Z,N)+\Delta_{\mathrm{p}}(Z,N)\}$ and using (30). The parameters α, β, and γ were obtained from a fit to experimental data for s-wave neutron resonance spacings of 272 nuclei at the neutron separation energy. The data were taken from the compilation by [182]. Similar investigations were recently undertaken by [255], who made, however, use of a slightly different description of the energy dependence of a and of different pairing gaps.

As a quantitative overall estimate of the agreement between calculations and experiments, one usually quotes the ratio

$$g \equiv \left\langle \frac{\rho_{\mathrm{calc}}}{\rho_{\mathrm{exp}}} \right\rangle = \exp\left[\frac{1}{n}\sum_{i=1}^{n}\left(\ln\frac{\rho^i_{\mathrm{calc}}}{\rho^i_{\mathrm{exp}}}\right)^2\right]^{1/2}, \qquad (31)$$

with n being the number of nuclei for which level densities ρ are experimentally known. As best fit we obtain an averaged ratio $g = 1.48$ with the parameter values $\alpha = 0.1337$, $\beta = -0.06571$, $\gamma = 0.04884$. This corresponds to $a/A = \alpha = 0.134$ for infinite nuclear matter, which is approached for high excitation energies. The ratios of experimental to predicted level densities (i.e. theoretical to experimental level spacings D) for the nuclei considered are shown in Fig. 1. As can be seen, for the majority of nuclei the absolute deviation is less than a factor of 2. This is a satisfactory improvement over

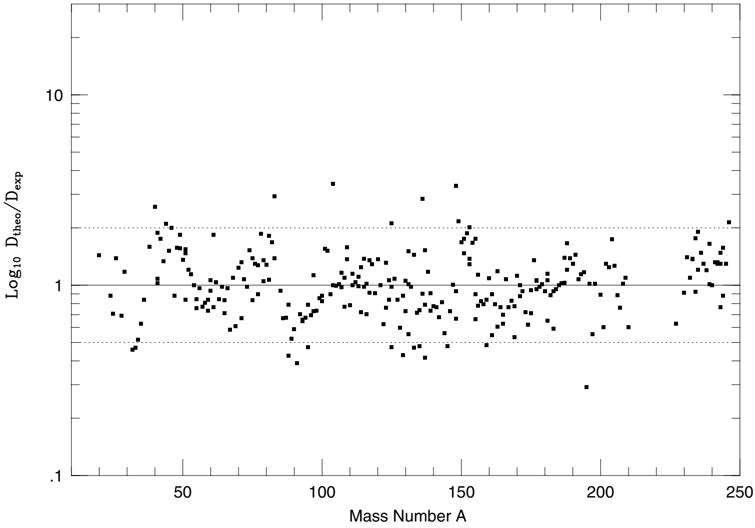

Fig. 1. Ratio of predicted to experimental [182] level densities at the neutron separation energy. The deviation is less than a factor of 2 (dotted lines) for the majority of the considered nuclei.

theoretical level densities used in previous astrophysical cross section calculations, where deviations of a factor 3–4, or even in excess of a factor of 10 were found [for details see [80]]. Such a direct comparison as in Fig. 1 was rarely shown in earlier work. In most cases the level density parameter a, entering exponentially into the level density, was displayed. Although we quoted the value of the parameter β above, it is small in comparison to α and can be set to zero without considerable increase in the obtained deviation. Therefore, actually only two parameters are needed for the level density description [311, 312].

Fully microscopic studies [89] are also becoming available by now. Their agreement is presently comparable to the approach described here. With these improvements, the uncertainty in the level density is now comparable to uncertainties in optical potentials and gamma transmission coefficients which enter the determinations of capture cross sections. The remaining uncertainty of extrapolations is the one due to the reliability of the nuclear structure model applied far from stability which provides the microscopic corrections and pairing gaps.

Applicability of the Statistical Model. Having a reliable level density description also permits to analyze when and where the statistical model approach is valid. Generally speaking, in order to apply the model correctly, a sufficiently large number of levels in the compound nucleus is needed in the relevant energy range, which can act as doorway states to the formation of the

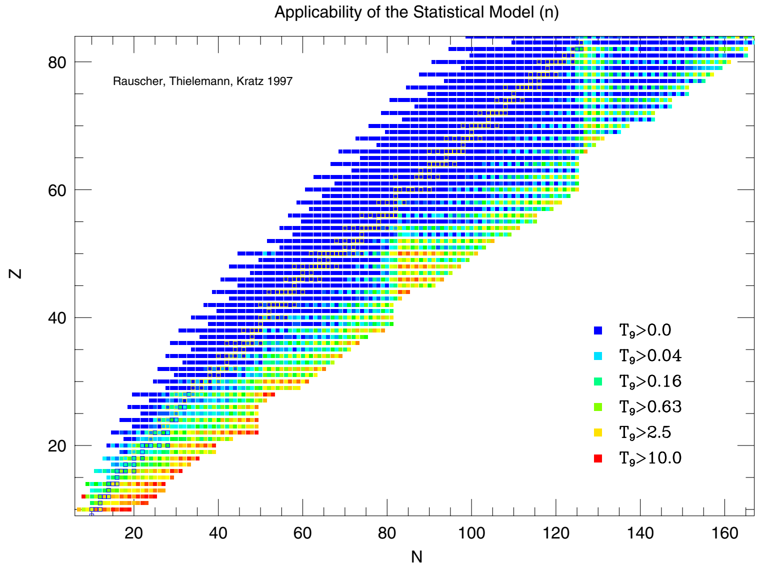

Fig. 2. Stellar temperatures (in 10^9 K) for which the statistical model can be used. Plotted is the compound nucleus of the neutron-induced reaction n+Target. Stable nuclei are marked in the same grey-scale but with a light grey frame.

compound nucleus. In the following this is discussed for neutron-, proton- and alpha-induced reactions with the aid of the level density approach presented above. This section is intended to be a guide to a meaningful and correct application of the statistical model.

Using the above effective energy windows for charged and neutral particle reactions from Sect. 2.1, a criterion for the applicability can be derived from the level density. For a reliable application of the statistical model a sufficient number of nuclear levels has to be within the energy window, thus contributing to the reaction rate. For narrow, isolated resonances, the cross sections (and also the reaction rates) can be represented by a sum over individual Breit-Wigner terms. The main question is whether the density of resonances (i.e. level density) is high enough so that the integral over the sum of Breit-Wigner resonances may be approximated by an integral over the statistcial model expressions of (17), which assume that at any bombarding energy a resonance of any spin and parity is available (see [409]).

Numerical test calculations have been performed by Rauscher et al. (1997) in order to find the average number of levels per energy window which is sufficient to allow this substitution in the specific case of folding over a MB distribution. To achieve 20% accuracy, about 10 levels in total are needed in the effective energy window in the worst case (non-overlapping, narrow resonances). This relates to a number of s-wave levels smaller than 3. Application of the statistical model for a level density which is not sufficiently

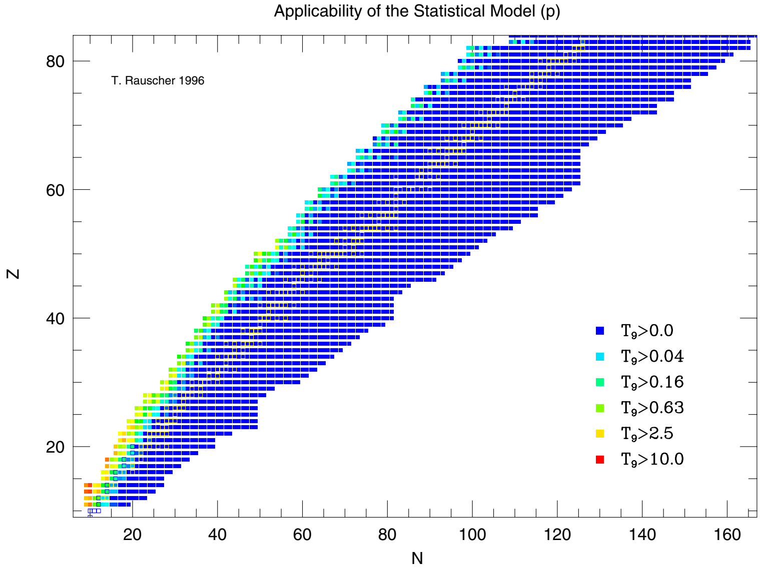

Fig. 3. Stellar temperatures (in 10^9) for which the statistical model can be used. Plotted is the compound nucleus of the proton-induced reaction p+Target. Stable nuclei are marked as in the previous figure.

large, results in general in an overestimation of the actual cross section, unless a strong s-wave resonance is located right in the energy window [see the discussion in [400]]. Therefore, we will assume in the following a conservative limit of 10 contributing resonances in the effective energy window for charged and neutral particle-induced reactions.

To obtain the necessary number of levels within the energy window of width Δ can require a sufficiently high excitation energy, as the level density increases with energy. This combines with the thermal distribution of projectiles to a minimum temperature for the application of the statistical model. Those temperatures are plotted in a logarithmic grey scale in Figs. 2–3. For neutron-induced reactions Fig. 2 applies, Fig. 3 describes proton-induced reactions. Plotted is always the minimum stellar temperature T_9 (in 10^9 K) at the location of the compound nucleus in the nuclear chart. It should be noted that the derived temperatures will not change considerably, even when changing the required level number within a factor of about two, because of the exponential dependence of the level density on the excitation energy.

This permits to read directly from the plot whether the statistical model cross section can be "trusted" for a specific astrophysical application at a specified temperature or whether single resonances or other processes (e.g. direct reactions) have also to be considered. These plots can give hints on when it is safe to use the statistical model approach and which nuclei have to be treated with special attention for specific temperatures. Thus, information on which nuclei might be of special interest for an experimental investigation may also be extracted. The general information can be taken that neutron-induced reactions are problematic close to the neutron drip-line and proton-induced reactions close to the proton drip-line. This is simply due to the very low excitation energy at which the compound nucleus is formed in such reactions. Alpha-induced reactions, not plotted here (but see [311], have very similar reaction Q-values accross the nuclear chart and therefore it is in most cases safe to apply the statistical model.

4 Weak-Interaction Rates

This section presents a discussion on recent progress in electron capture and beta decay rates via large scale shell model calculations and for neutrino-induced reactions in general. Pure decay studies for heavy nuclei, where shell model calculations are presently not yet feasable and large scale QRPA calculations are employed, have been addressed in Sect. 1.1 (decays) and in the experimental Sect. 2 as well.

4.1 Electron Capture and Beta-Decay

For densities $\rho \leq 10^{11}$ g/cm^3, stellar weak-interaction processes are dominated by Gamow-Teller (GT) and, if applicable, by Fermi transitions. (One distinguishes between GT$_+$ transitions, where a proton is changed into a neutron, and GT$_-$ transitions, where a neutron is changed into a proton. Electron capture is sensitive to the GT$_+$ strength, while ordinary β decay depends on the GT$_-$ distribution.) At higher densities forbidden transitions have to be included as well. To understand the requirements for the nuclear models to describe these processes (mainly electron capture), it is quite useful to recognize that electron capture is governed by two energy scales: the electron chemical potential (or Fermi energy) μ_e, which grows like $\rho^{1/3}$, and the nuclear Q-value. As is sketched in Fig. 4, μ_e grows much faster than the Q values of the abundant nuclei. We can conclude that at low densities, where one has $\mu_e \sim Q$ (i.e. during late hydrostatic burning), the capture rate will be very sensitive to the phase space and requires an accurate as possible description of the detailed GT$_+$ distribution of the nuclei involved. Furthermore, the finite temperature in the star requires the implicit consideration of capture on excited nuclear states, for which the GT distribution can be different than for the ground state. As we will demonstrate below, modern shell model calculations are capable to describe GT$_+$ rather well and are therefore the appropriate tool to calculate the weak-interaction rates for those nuclei ($A \sim 50 - 65$) which are relevant at such densities. At higher densities, when μ_e is sufficiently larger than the respective nuclear Q values, the capture rate becomes less sensitive to the detailed GT$_+$ distribution and is mainly only dependent on the total GT strength. Thus, less sophisticated nuclear models might be sufficient. However, one is facing a nuclear structure problem

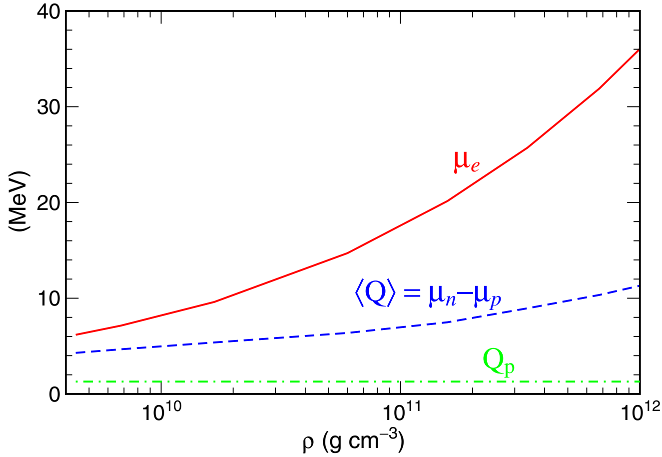

Fig. 4. Sketch of the various energy scales related to electron capture on protons and nuclei as a function of densitiy during a supernova core collapse simulation. Shown are the chemical potential / Fermi energy of electrons, the Q-values for electron capture on free protons (constant) and the average Q-value for electron capture on nuclei for the given composition at each density.

which has been overcome only very recently. We come back to it below, after we have discussed the calculations of weak-interaction rates within the shell model and their implications to presupernova models.

The general formalism to calculate weak interaction rates for stellar environment has been given by Fuller, Fowler and Newman (FFN) [113–116]. These authors also estimated the stellar electron capture and beta-decay rates systematically for nuclei in the mass range $A = 20 - 60$ based on the independent particle model and on data, whenever available. In recent years this pioneering and seminal work has been replaced by rates based on large-scale shell model calculations. At first, Oda *et al.* derived such rates for *sd*-shell nuclei ($A = 17 - 39$) and found rather good agreement with the FFN rates [289]. Similar calculations for *pf*-shell nuclei had to wait until significant progress in shell model diagonalization, mainly due to Etienne Caurier, allowed calculations in either the full *pf* shell or at such a truncation level that the GT distributions were virtually converged. It has been demonstrated in [70] that the shell model reproduces all measured GT_+ distributions very well and gives a very reasonable account of the experimentally known GT_- distributions. Further, the lifetimes of the nuclei and the spectroscopy at low energies is simultaneously also described well. Charge-exchange measurements using the (d,^{2}He) reaction at intermediate energies allow now for an experimental determination of the GT_+ strength distribution with an energy resolution of about 150 keV. Figure 5 compares the experimental GT_+ strength for ^{51}V, measured at the KVI in Groningen [16], with shell model predictions. It can be concluded that modern shell model approaches have the necessary pre-

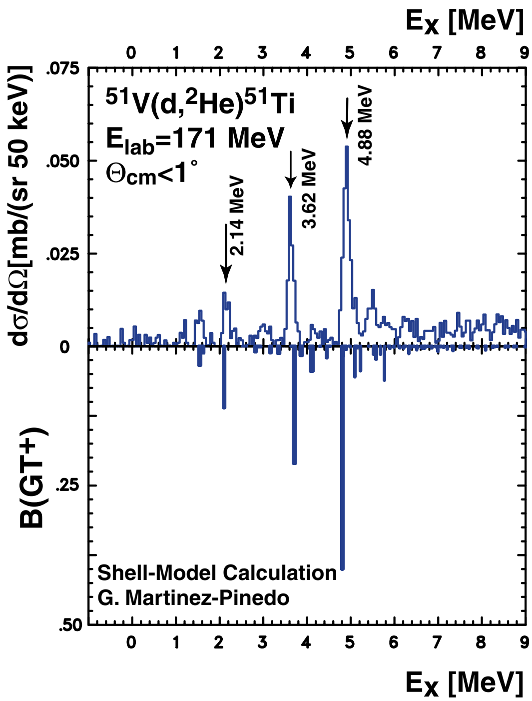

Fig. 5. Comparison of the measured ^{51}V(d,^{2}He)^{51}Ti cross section at forward angles (which is proportional to the GT_+ strength) with the shell model GT distribution in ^{51}V (from [16]).

dictive power to reliably estimate stellar weak interaction rates. Such rates have been presented in [223,224]. for more than 100 nuclei in the mass range A = 45-65. The rates have been calculated for the same temperature and density grid as the standard FFN compilations [114,115]. An electronic table of the rates is available [224]. Importantly one finds that the shell model electron capture rates are systematically smaller than the FFN rates. The difference is particularly large for capture on odd-odd nuclei which have been previously assumed to dominate electron capture in the early stage of the collapse [19]. The differences are related to an insufficient treatment of pairing in the FFN parametrization, as discussed in [223].

4.2 Neutrino-Induced Reactions

While elastic scattering of neutrinos on nuclei is important for neutrino opacities to describe the leakage and escape of neutrinos, neutrino-induced reactions on nuclei can also play a role at high densities during the stellar collapse and explosion phase in causing composition changes [145]. Note that during the collapse only ν_e neutrinos are present. Thus, charged-current reactions

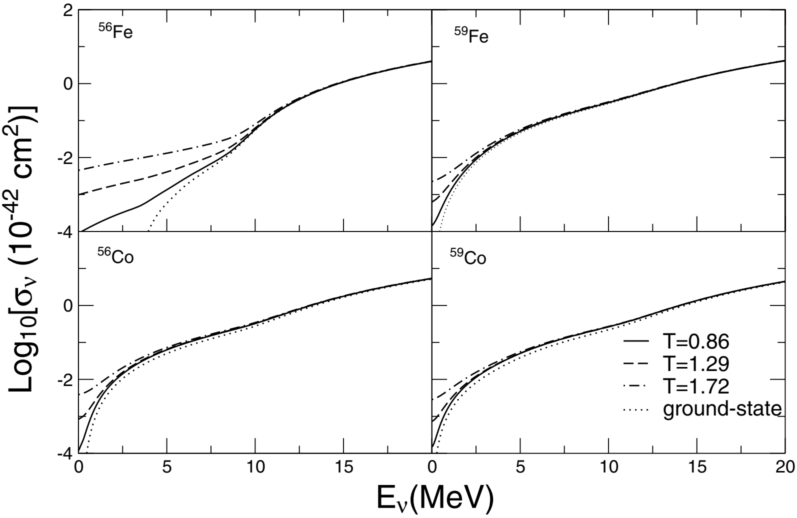

Fig. 6. Cross sections for inelastic neutrino scattering on nuclei at finite temperature. The temperatures are given in MeV (from [334]).

$A(\nu_e, e^-)A'$ are strongly blocked by the large electron chemical potential [50, 333]. Inelastic neutrino scattering on nuclei can compete with $\nu_e + e^-$ scattering at higher neutrino energies $E_\nu \geq 20$ MeV [50]. At such energies forbidden transitions can contribute noticeably to the cross sections. Finite-temperature effects play an important role for inelastic $\nu + A$ scattering below $E_\nu \leq 10$ MeV. This comes about as nuclear states, which are connected to the ground state and low-lying excited states by modestly strong GT transitions and increased phase space, get thermally excited. As a consequence the cross sections are significantly increased for low neutrino energies at finite temperature and might be comparable to inelastic $\nu_e + e^-$ scattering [334]. Thus, inelastic neutrino-nucleus scattering, which is so far neglected in collapse simulations, should be implemented in such studies. This is in particular motivated by the fact that it has been demonstrated that electron capture on nuclei dominates during the collapse and that this mode generates significantly less energetic neutrinos than considered previously (see below). Examples for inelastic neutrino-nucleus cross sections are shown in Fig. 6. A reliable estimate for these cross sections requires the knowledge of the GT_0 strength. Shell model predictions imply that the GT_0 centroid resides at excitation energies around 10 MeV and is independent of the pairing structure of the ground state [387,334]. Finite temperature effects become unimportant for stellar inelastic neutrino-nucleus cross sections once the neutrino energy is large enough to reach the GT_0 centroid, i.e. for $E_\nu \geq 10$ MeV.

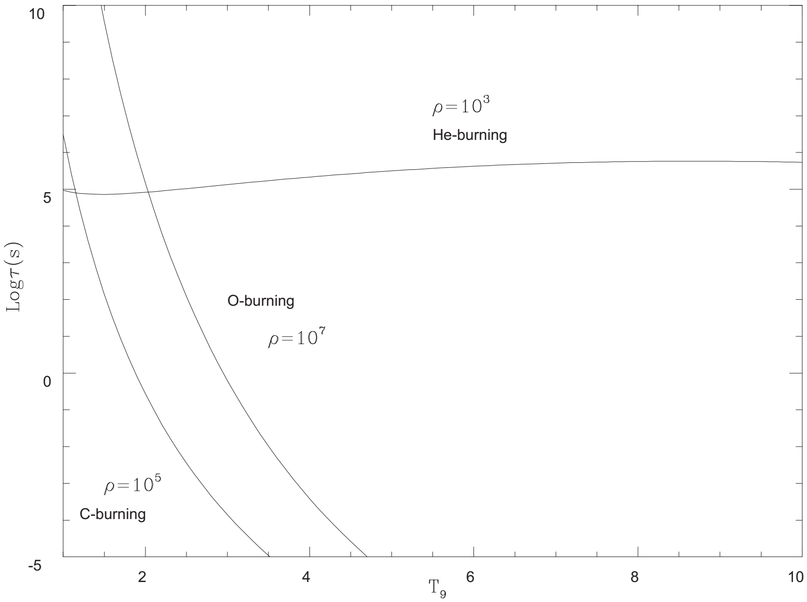

Fig. 7. Burning timescales for fuel destruction of He-, C-, and O-burning as a function of temperature. A 100% fuel mass fraction was assumed. The factor $N^i_{i,i} = N_i/N_i!$ cancels for the destruction of identical particles by fusion reactions, as N_i=2. For He-burning the destruction of three identical particles has to be considered, which changes the leading factor $N^i_{i,i,i}$ to 1/2. The density-dependent burning timescales are labeled with the chosen typical density. They scale linearly for C- and O-burning and quadraticly for He-burning. Notice that the almost constant He-burning timescale beyond T_9=1 has the effect that efficient destruction on explosive timescales can only be attained for high densities.

5 Explosive Burning Processes

General aspects of explosive burning have been already discussed in Sect. 1.3. Before we enter a detailed description of explosive events in single and binary stellar systems in Sect. 8, we want to give a preview of explosive burning processes applicable to such events.

Burning timescales in stellar evolution are dictated by the energy loss timescales of stellar environments. Processes like hydrogen and helium burning, where the stellar energy loss is dominated by the photon luminosity, choose temperatures with energy generation rates equal to the radiation losses. For the later burning stages neutrino losses play the dominant role among cooling processes and the burning timescales are determined by temperatures where neutrino losses are equal to the energy generation rate. Explosive events are determined by hydrodynamics, causing different temperatures and timescales for the burning of available fuel. We can generalize the

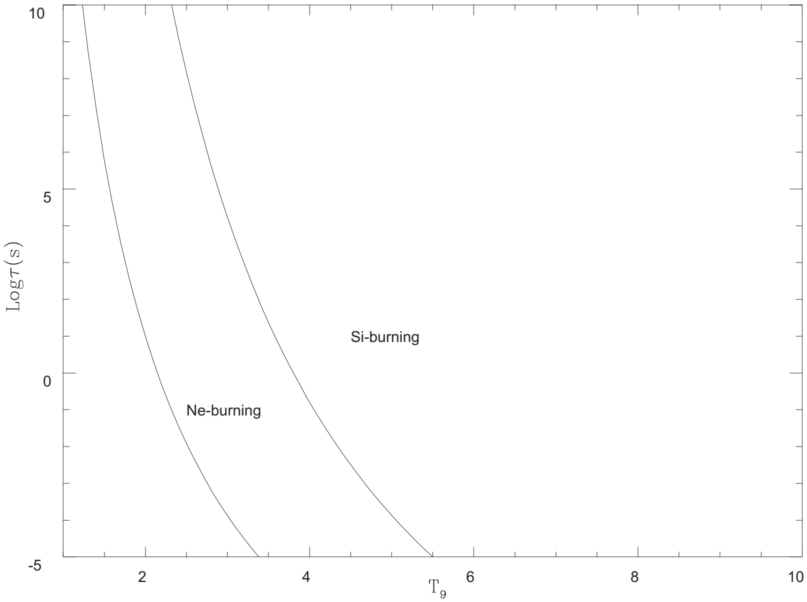

Fig. 8. Burning timescales for fuel destruction of Ne- and Si-burning as a function of temperature. These are burning phases initiated by photodisintegrations and therefore not density-dependent.

question by defining a burning timescale according to (11) for the destruction of the major fuel nuclei i

$$\tau_i = |\frac{Y_i}{\dot{Y}_i}|. \tag{32}$$

These timescales for the fuels ($i \in$ H, He, C, Ne, O, Si) are determined by the major destruction reaction. They are in all cases temperature dependent. If this dominating reaction is a decay or photodisintegration process, the timescale does not depend on density. This applies to Ne- and Si-burning, which are dominated by (γ, α) destructions of ^{20}Ne and ^{28}Si. Here the timescales are only determined by the burning temperatures. If the dominating reaction is (i) a two-particle or (ii) a three-particle fusion reaction, they have an inverse (i) linear or (ii) quadratic density dependence. Thus, in the burning stages which involve a fusion process, the density dependence is linear, with the exception of He-burning, where it is quadratic due to the triple-alpha reaction. The temperature dependences are typically exponential, due to the functional form of the corresponding $N_A < \sigma v >$ expressions. We have plotted these burning timescales as a function of temperature (see Figs. 7 and 8), assuming a fuel mass fraction of 1. The curves for (also) density dependent burning processes are labeled with a typical density. If we take typical explosive burning timescales to be of the order of seconds (e.g. in supenovae), we see that one requires temperatures to burn essential parts of the fuel in excess of 4×10^9 K (Si-burning), 3.3×10^9 K (O-burning), 2.1×10^9 K (Ne-burning), and 1.9×10^9 K (C-burning). Beyond 10^9 K He-burning is determined by an almost constant burning timescale. We see that essential destruction on a time scale of 1s is only possible for densities $\rho>10^5$ gcm^{-3}. This is usually not encountered in He-shells of massive stars. In a similar way explosive H-burning is not of relevance for massive stars, but important for explosive burning in accreted H-envelopes in binary stellar evolution.

5.1 Explosive H-Burning

The major destruction of hydrogen in hydrostatic burning occurs via the pp-chain(s), initiated by ^{1}H$(p,e^+\nu_e)^2$H, and the CNO cycle which converts ^{1}H into ^{4}He by a sequence of (p,γ) and (p,α) reactions on C, N, and O isotopes and subsequent beta-decays. Higher temperatures can enhance the reaction rates of charged-particle captures which depend on the penetration of Coulomb barriers. This can speed up the reactions following ^{1}H$(p,e^+\nu_e)^2$H and convert the pp-chains to the so-called hot pp-chains [419], which convert ^{2}H to CNO isotopes. However, this speeds up only the explosive burning of pre-existing ^{2}H, the destruction of the fuel ^{1}H is dependent on the weak reaction ^{1}H$(p,e^+\nu_e)^2$H which enforces long timecales. In the hydrostatic CNO-cycle the reaction ^{14}N$(p,\gamma)^{15}$O is the slowest reaction. Higher temperatures can speed up this fusion reaction (and the reaction ^{13}N(p,γ)^{14}O which then wins over the ^{13}N beta-decay) and lead to the hot CNO-cycle ^{12}C(p,γ)^{13}N(p,γ)^{14}O$(e^+\nu)^{14}$N(p,γ)^{15}O$(e^+\nu)$. But also this cycle is limited by the beta-decay half-lives of ^{14}O and ^{15}O (of the order of minutes) and does not permit H-destruction on the timescale of seconds. The latter can only occur when nuclei above Ne are produced and a sequence of proton captures and (very fast) beta-decays close to the proton drip-line converts hydrogen to heavy nuclei in the so-called rp-process (rapid proton capture process). Such a process can be ignited in high density environments, where the pressure is dominated by the degenerate electron gas and shows no temperature dependence. This prevents a stable and controlled burning, leading therefore to a thermonuclear runaway. While the ignition is always based on pp-reactions (as in solar hydrogen burning), the runaway leads to the hot CNO-cycle, branching out partially via ^{15}N(p,γ)^{16}O(p,γ) ^{17}F$(e^+\nu)$ ^{17}O(p,γ)^{18}F...

In essentially all nuclei below Ca, a proton capture reaction on the nucleus (Z_{even}–1,N=Z_{even}) produces the compound nucleus above the alpha-particle threshold and permits a (p,α) reaction. This is typically not the case for (Z_{even}–1,N=Z_{even}–1) due to the smaller proton separation energy and leads to hot CNO-type cycles above Ne (see Fig. 11 in [376]). There is one exception, Z_{even}=10, where the reaction ^{18}F(p,α) is possible, avoiding ^{19}F and a possible leak via ^{19}F(p,γ) into the NeNaMg-cycle. This has the effect that only alpha induced reactions like ^{15}O(α,γ) can aid a break-out from the hot CNO-cycle to heavier nuclei beyond Ne [421]. Break-out reactions from the hot CNO-type cycles above Ne proceed typically via proton captures on the nucleus (Z_{even},N=Z_{even}-1) and permits a faster build-up of heavier nuclei [376,324]. They occur at temperatures of about 3×10^8 K, while the alpha-induced break-out from the hot CNO-cycle itself is delayed to about 4×10^8 K. Maximum temperatures of the range 3×10^8 K provide major nucleosynthesis yields of hot CNO-products like ^{15}N and specific nuclei between Ne and Si/S, which are based on the processing of pre-existing Ne (see the discussion in Fig. 9). Once the hot CNO-cycle, and higher cycles beyond Ne, have generated sufficient amounts of energy in order to surpass temperatures of $\sim 4 \times 10^8$ K, alpha-induced reactions lead to a break-out from the hot CNO-cycle. This provides new fuel for reactions beyond Ne, leading to a further increase in temperature and subsequently also helium burns explosively in a thermonuclear runaway [336,337]. In the next stage of the ignition process also He is burned via the 3α-reaction ^{4}He($2\alpha, \gamma$)^{12}C, filling the CNO reservoir, and the αp-process (a sequence of (α,p) and (p,γ) reactions [410]) sets in. It produces nuclei up to Ca and provides seed nuclei for hydrogen burning via the rp-process (proton captures and beta-decays). Processing of the αp-process and rp-process up to and beyond ^{56}Ni is shown in Fig. 25. Certain nuclei play the role of long waiting points in the reaction flux, where long beta-decay half-lives dominate the flow, either competing with slow (α,p) reactions or negligible (p,γ) reactions, because they are inhibited by inverse photodisintegrations for the given temperatures. Such nuclei were identified as ^{25}Si ($\tau_{1/2} = 0.22$ s), ^{29}S (0.187 s), ^{34}Ar (0.844 s), ^{38}Ca (0.439 s). The bottle neck at ^{56}Ni can only be bridged for minimum temperatures around 10^9 K (in order to overcome the Coulomb barrier for proton capture) and maximum temperatures below 2×10^9 K (in order to avoid photodisintegrations), combined with high densities exceeding 10^6 gcm^{-3} which support the capture process [336,321]. If this bottle neck can be overcome, other waiting points like ^{64}Ge (64 s), ^{68}Se (96 s), ^{74}Kr (17 s) seem to be hard to pass. However, partially temperature dependent half-lives (due to excited state population), or mostly 2p-capture reactions via an intermediate proton-unstable nucleus (introduced in [127] and applied in [336]) can help. The final endpoint of the rp-process was found recently [337], to be caused by a closed reaction cycle in the Sn-Sb-Te region due to increasing alpha-instability of heavy proton-rich nuclei.

5.2 Explosive He-Burning

Explosive He-burning is characterized by the same reactions as hydrostatic He-burning, producing ^{12}C and ^{16}O. Figure 7 indicates that even for temperatures beyond 10^9 K high densities ($>10^5$ gcm^{-3}) are required to burn essential amounts of He. This would cause major fuel distruction only in (electron) degenerate high density environments like white dwarfs with unburned He. Such environments are envisioned in sub-Chandrasekhar mass type Ia supernovae [239,131], but observations do not favor such models [161,288,286]. During the passage of a 10^{51}erg (type II) supernova shockfront through the

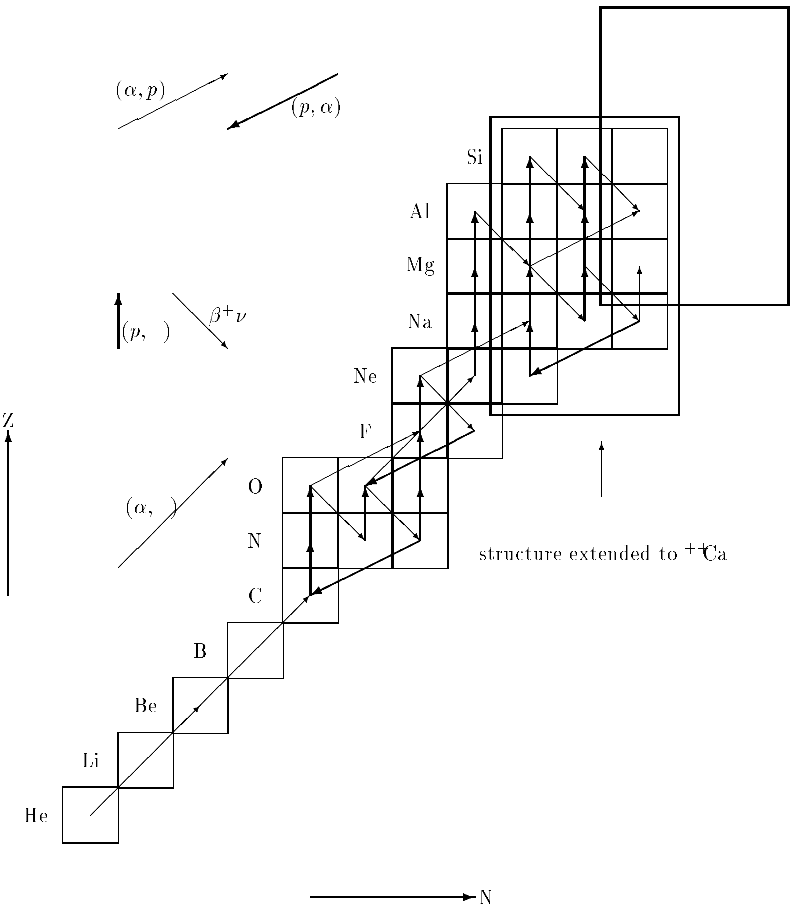

Fig. 9. The hot CNO-cycle incorporates three proton captures, (^{12}C, ^{13}N, ^{14}N), two β^+-decays (^{14,15}O) and one (p, α)-reaction (^{15}N). In a steady flow of reactions the long beta-decay half-lives are responsible for high abundances of ^{15,14}N (from ^{15,14}O decay) in nova ejecta. From Ne to Ca, cycles similar to the hot CNO exist, based always on alpha-nuclei like ^{20}Ne, ^{24}Mg etc. The exception is the (not completed) cycle based on ^{16}O, due to ^{18}F(p,α)^{15}O, which provides a reaction path back into the hot CNO-cycle. Thus, in order to proceed from C to heavier nuclei, alpha-induced CNO break-outs are required. The shown flow pattern, which includes alpha-induced reactions, applies for temperatures in the range 4-8$\times 10^8$ K. Smaller temperatures permit already processing of pre-existing Ne via hot CNO-type cycles. This leads to the typical nova abundance pattern with ^{15,14}N enhancements, combined with specific isotopes up to about Si or even Ca. If the white dwarf is an ONeMg rather than CO white dwarf, containing Ne and Mg in its initial composition resulting from carbon rather than helium burning, the latter feature is specifically recognizable.

He-burning zones of a massive $25M_\odot$ star, maximum temperatures of only (6-9)$\times 10^8$ K are attained and the amount of He burned is negligible. However, neutron sources like ^{22}Ne$(\alpha, n)^{25}$Mg [or ^{13}C$(\alpha, n)^{16}$O], which sustain an s-process neutron flux in hydrostatic burning, release a large neutron flux under explosive conditions. This leads to partial destruction of ^{22}Ne and the build-up of ^{25,26}Mg via ^{22}Ne$(\alpha, n)^{25}$Mg$(n, \gamma)^{26}$Mg. Similarly, ^{18}O and ^{13}C are destroyed by alpha-induced reactions. This releases neutrons with $Y_n \approx 2\times 10^{-9}$ at a density of $\approx 8.3\times 10^3$ gcm^{-3}, corresponding to $n_n \approx 10^{19}$cm^{-3} for about 0.2s, and causes neutron processing [394,370,373,79]. This is, however, not an r-process [168,314].

5.3 Explosive C- and Ne-Burning

The main burning products of explosive neon burning are ^{16}O, ^{24}Mg, and ^{28}Si, synthesized via the reactions ^{20}Ne$(\gamma, \alpha)^{16}$O or ^{20}Ne$(\alpha, \gamma)^{24}$Mg$(\alpha, \gamma)^{28}$Si, similar to the hydrostatic case. The mass zones in supernovae which undergo explosive neon burning must have peak temperatures in excess of 2.1×10^9K. They undergo a combined version of explosive neon and carbon burning (see Figs. 7 and 8). Mass zones which experience temperatures in excess of 1.9×10^9 K will undergo explosive carbon burning, as long as carbon fuel is available. This is often not the case in type II supernovae originating from massive stars. Besides the major abundances, mentioned above, explosive neon burning supplies also substantial amounts of ^{27}Al, ^{29}Si, ^{32}S, ^{30}Si, and ^{31}P. Explosive carbon burning contributes in addition the nuclei ^{20}Ne, ^{23}Na, ^{24}Mg, ^{25}Mg, and ^{26}Mg. Many nuclei in the mass range $20<A<30$ can be reproduced in solar proportions. This was confirmed for realistic stellar conditions [275,438,375,377,314]. As photodisintegrations become important in explosive Ne-burning, also heavier pre-existing nuclei in such burning shells, from previous s- or r-processing (originating from prior stellar evolution or earlier stellar generations), can undergo e.g. (γ, n) or (γ, α) reactions. These can produce rare proton-rich stable isotopes of heavy elements in the so-called p- or gamma-process [435,316,169,317,314,13].

5.4 Explosive O-Burning

Temperatures in excess of roughly 3.3×10^9 K lead to a quasi-equilibrium (QSE) in the lower QSE-cluster which extends over the range 28<A<45 in mass number, while the path to heavier nuclei is blocked by small Q-values and reaction cross sections for reactions out of closed shell nuclei with Z or N=20 [429,157,158]. A full NSE with dominant abundances in the Fe-group cannot be attained. The main burning products are ^{28}Si, ^{32}S, ^{36}Ar, ^{40}Ca, ^{38}Ar, and ^{34}S, while ^{33}S, ^{39}K, ^{35}Cl, ^{42}Ca, and ^{37}Ar have mass fractions of less than 10^{-2}. In zones with temperatures close to 4×10^9K there exists some contamination by the Fe-group nuclei ^{54}Fe, ^{56}Ni, ^{52}Fe, ^{58}Ni, ^{55}Co, and ^{57}Ni.

The abundance distribution within the QSE-cluster is determined by alpha, neutron, and proton abundances. Because electron captures during explosive processing are negligible, the original neutron excess stays unaltered and fixes the neutron to proton ratio. Under those conditions the resulting composition is dependent only on the alpha to neutron ratio at freeze-out. An extensive study [429] noted that with a neutron excess $\eta(=\sum_i (N_i - Z_i)Y_i)$ of 2×10^{-3} the solar ratios of ^{39}K/^{35}Cl, ^{40}Ca/^{36}Ar, ^{36}Ar/^{32}S, ^{37}Cl/^{35}Cl, ^{38}Ar/ ^{34}S, ^{42}Ca/^{38}Ar, ^{41}K/^{39}K, and ^{37}Cl/^{33}S are attained within a factor of 2 for freeze-out temperatures in the range $(3.1 - 3.9) \times 10^9$K. This is the typical neutron excess resulting from solar CNO-abundances, which are first transformed into ^{14}N in H-burning and then into ^{22}Ne in He-burning via $^{14}\mathrm{N}(\alpha,\gamma)^{18}\mathrm{F}(\beta^+)^{18}\mathrm{O}(\alpha,\gamma)^{22}\mathrm{Ne}$, while for lower values of the neutron excess (as expected for stars of lower metallicity) essentially only the alpha nuclei ^{28}Si, ^{32}S, ^{36}Ar, ^{40}Ca are produced in sufficient amounts. This affects element abundances and causes an odd-even staggering in Z. There exist extensive discussions of such results in supernova models [378,375,377,162,187,44,368, 372].

5.5 Explosive Si-Burning

Zones which experience temperatures in excess of 4.0–5.0$\times 10^9$ K undergo explosive Si-burning. For $T > 5 \times 10^9$K essentially all Coulomb barriers can be overcome and a nuclear statistical equilibrium is established. Such temperatures lead to complete Si-exhaustion and produce Fe-group nuclei. The doubly-magic nucleus ^{56}Ni, with the largest binding energy per nucleon for N=Z, is formed with a dominant abundance in the Fe-group in case Y_e is larger than 0.49. Explosive Si-burning can be divided into three different regimes: (i) incomplete Si-burning and complete Si-burning with either (ii) a normal or (iii) an alpha-rich freeze-out. Which of the three regimes is encountered depends on the peak temperatures and densities attained during the passage of a supernova shock/burning front [429] shown in Fig. 10). One recognizes that the mass zones of SNe Ia and SNe II experience different regions of complete Si-burning [378,375,377,162,187,44,368,372].

At high temperatures in complete Si-burning or also during a normal freeze-out, the abundances are in a full NSE and given by (13). An alpha-rich freeze-out is caused by the inability of the triple-alpha reaction $^4\mathrm{He}(2\alpha,\gamma)^{12}\mathrm{C}$, transforming ^{4}He into ^{12}C, and the $^4\mathrm{He}(\alpha n,\gamma)^9\mathrm{Be}$ reaction, to keep light nuclei like n, p, and ^{4}He, and intermediate mass nuclei beyond A=12 in an NSE during declining temperatures, when the densities are small. The latter enter quadratically for these rates, causing during the fast expansion and cooling in explosive events a large alpha abundance after charged particle freeze-out, which shifts the QSE groups to heavier nuclei, tranforming e.g. ^{56}Ni, ^{57}Ni, and ^{58}Ni into ^{60}Zn, ^{61}Zn, and ^{62}Zn [158].

This also leads to a slow supply of carbon nuclei still during freeze-out, leaving traces of alpha nuclei, ^{32}S, ^{36}Ar, ^{40}Ca, ^{44}Ti, ^{48}Cr, and ^{52}Fe, which

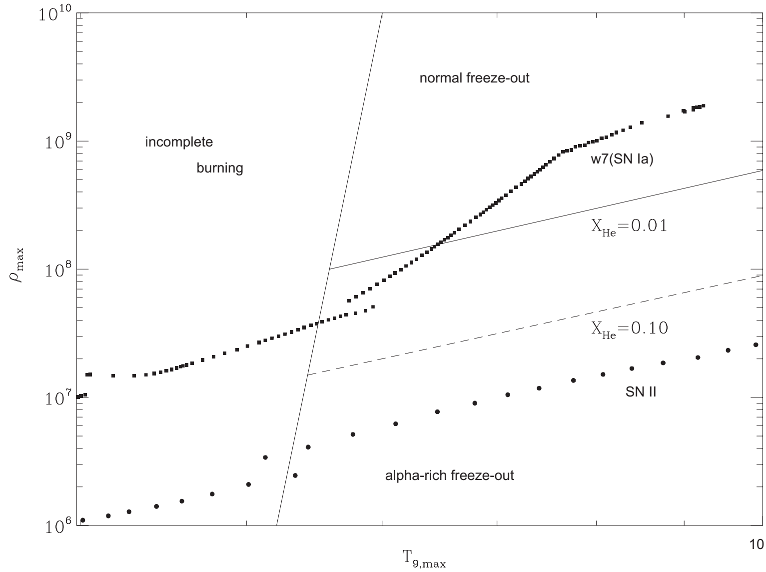

Fig. 10. Division of the $\rho_{max} - T_{max}$-plane for adiabatic expansions from ρ_{max} and T_{max} with an adiabatic index of 4/3 and a hydrodynamic timescale equal to the free fall timescale. Conditions separate into incomplete and complete Si-burning with normal and alpha-rich freeze-out. Contour lines of constant ^{4}He mass fractions in complete burning are given for levels of 1 and 10%. They coincide with lines of constant radiation entropy per gram of matter. For comparision also the maximum $\rho - T$-conditions of individual mass zones in type Ia and type II supernovae are indicated.

did not fully make their way up to ^{56}Ni. Figure 11 shows this effect, typical for SNe II, as a function of remaining alpha-particle mass fraction after freeze-out. The major NSE nuclei ^{56}Ni, ^{57}Ni, and ^{58}Ni get depleted when the remaining alpha fraction increases, while all other species mentioned above increase.

Incomplete Si-burning is characterized by peak temperatures of (4–5) $\times$ 10^9 K. Temperatures are not high enough for an efficient bridging of the bottle neck above the proton magic number $Z = 20$ by nuclear reactions. Besides the dominant fuel nuclei ^{28}Si and ^{32}S we find the alpha-nuclei ^{36}Ar and ^{40}Ca being most abundant. Partial leakage through the bottle neck above Z=20 produces ^{56}Ni and ^{54}Fe as dominant abundances in the Fe-group. Smaller amounts of ^{52}Fe, ^{58}Ni, ^{55}Co, and ^{57}Ni are encountered.

The discussion above focussed mostly on conditions for $Y_e \approx 0.5$. The results can vary strongly with more proton or more neutron rich environments, which also has an influence on Figs. 10 and 11. Explosive Si-burning occurs in type Ia as well as type II supernovae, and both environments encounter physical effects which can alter Y_e drastically (electron captures at high densities and temperatures in SNe Ia as well as II, neutrino-induced reactions

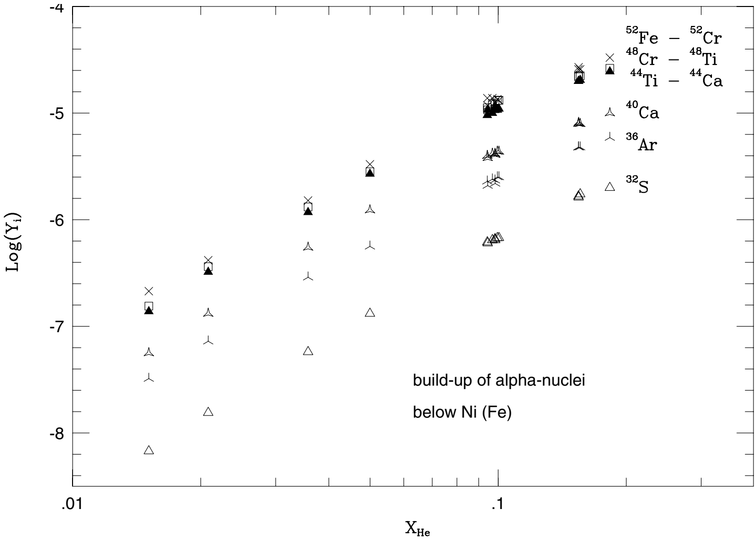

Fig. 11. Display of the composition up to Cr and from Mn to Ni (after decay) as a function of remaining alpha mass-fraction X_{He} from an alpha-rich freeze-out. Lighter nuclei, being produced by alpha-captures from a remaining alpha reservoir, have larger abundances for more pronounced alpha-rich freeze-outs.

on nucleons and nuclei in SNe II). The basic recipe for SN Ia explosions is simple. A white dwarf in a binary system, growing towards the limiting Chandrasekhar mass, contracts and ignites under degenerate (electron gas) conditions, causing a thermonuclear runaway and an explosion and complete disruption of the white dwarf. This topic will not be discussed in this review, as the resulting nucleosynthesis does still lead to nuclei close to the stability line [187,44,372]. All explosive burning phases outlined above will be discussed in more detail for a number of astrophysicsl events in Sects. 6 through 8.

5.6 The r-Process

The r-process is an application of explosive Si-burning for either extreme conditions in Y_e and/or the entropy of the matter involved. The operation of an r-process is characterized by the fact that 10 to 100 neutrons per seed nucleus (in the Fe-peak or somewhat beyond) have to be available to form all heavier r-process nuclei by neutron capture. For a composition of Fe-group nuclei and free neutrons that translates into a neutron excess of $\eta = \sum_i (N_i - Z_i) Y_i = 0.4$-$0.7$ or $Y_e = \sum_i Z_i Y_i = 0.15$–$0.3$. Such a high neutron excess can only by obtained if weak interactions play a major role either via electron capture or neutrino absorption on nucleons and nuclei. In the case of electron capture one needs energetic electrons (on protons or nuclei) which have to overcome large negative Q-values. This can be achieved by degenerate electrons with large Fermi energies and requires a compression to densities of $10^{11} - 10^{12}$ gcm^{-3}, with a beta equilibrium between electron captures and β^--decays [68] as found in neutron star matter [256,109].

Another option is an extremely alpha-rich freeze-out in complete Si-burning with moderate neutron excesses η and Y_e's. After the freeze-out of charged particle reactions in matter which expands from high temperatures but relatively low densities, 70, 80, 90 or 95% of all matter can be locked into ^{4}He with $N{=}Z$. Figure 10 showed the onset of such an extremely alpha-rich freeze-out by indicating contour lines for He mass fractions of 1 and 10%. These contour lines correspond to T_9^3/ρ=const, which is proportional to the entropy per gram of matter of a radiation dominated gas. Thus, the radiation entropy per gram of baryons can be used as a measure of the ratio between the remaining He mass-fraction and heavy nuclei. Similarly, the ratio of neutrons to Fe-group (or heavier) nuclei (i.e. the neutron to seed ratio) is a function of entropy and permits for high entropies, with large remaining He and neutron abundances and small heavy seed abundances, neutron captures which proceed to form the heaviest r-process nuclei [434,258,364,436,163,164, 108,412,383,367]).

A different situation surfaces for maximum temperatures below freeze-out conditions for charged particle reactions with Fe-group nuclei. Then reactions among light nuclei which release neutrons, like (α, n) reactions on ^{13}C and ^{22}Ne, can sustain a neutron flux. The constraint of having 10-100 neutrons per heavy nucleus, in order to attain r-process conditions, can only be met by small abundances of Fe-group nuclei. Such conditions were expected when a shock front passes the He-burning shell and enhances the ^{22}Ne(α, n) reaction by orders of magnitude. However, it was shown [79,314] that this neutron source is not strong enough for an r-process in realistic stellar models. Research, based on additional neutron release via inelastic neutrino scattering [95], can also not produce neutron densities which are required for such a process to operate [431,259].

For a number of years r-process calculations independent of a specific astrophysical site, and just based on the goal to find the required neutron number densities and temperatures which can reproduce the solar abundance pattern of heavy elements, have been performed [214,216,376,73,43,108,81, 301,339]. They, together with applications to the astrophysical sites listed above, will be discussed in Sect. 7.

6 Core Collapse Supernovae

The ^{12}C$(\alpha, \gamma)^{16}$O reaction causes large uncertainties in stellar evolution and for the pre-supernova models [100,66,65,24,51,440,441,15,219,52,53,386,98]. However, also the treatment of convection in stellar evolution is not a settled one, especially the issue of overshooting and semiconvection. This has an influence on the possible growth of the He-burning core, which causes mixing in of fresh He at higher temperatures, and consequently also enhances the O/C ratio. Stellar evolution calculations [228] showed that the total amount of ^{16}O can also vary by almost a factor of 3, for the extreme choices of the semi-convection parameter. The resulting properties in terms of size and composition of the stellar core after He-burning have a strong influence on all subsequent burning stages [314,148,432].

At the end of hydrostatic burning, a massive star consists of concentric shells that are the remnants of its previous burning phases (hydrogen, helium, carbon, neon, oxygen, silicon). Iron is the final stage of nuclear fusion in hydrostatic burning, as the synthesis of any heavier element from lighter elements does not release energy; rather, energy must be used up. If the iron core, formed in the center of the massive star, exceeds the Chandrasekhar mass limit of about 1.44 solar masses (or up to about 30% larger values in case of not fully degenerate conditions in massive stars), electron degeneracy pressure cannot longer stabilize the core and it collapses, starting what is called a core collapse supernova (in most cases if the hydrogen envelope was not lost during stellar evolution this coincides with a type II supernova). In its aftermath a central neutron star or black hole is formed and the surrounding shells are ejected into the Interstellar Medium. Although this general picture has been confirmed by the various observations from supernova SN1987A, simulations of the core collapse and the explosion are still far from being completely understood and robustly modelled. To improve the input which goes into the simulation of type II supernovae and to improve the models and their numerical simulations is a very active research field at various institutions worldwide.

The collapse is very sensitive to the entropy and to the number of leptons per baryon, Y_e [30]. In turn these two quantities are mainly determined by weak interaction processes, electron capture and β decay. First, in the early stage of the collapse Y_e is reduced as it is energetically favorable to capture electrons, which at the densities involved have Fermi energies of a few MeV, on (Fe-peak) nuclei. This reduces the electron pressure, thus accelerating the collapse, and shifts the distribution of nuclei present in the core to more neutron-rich material. Second, many of the nuclei present can also β decay. While this process is quite unimportant compared to electron capture for initial Y_e values around 0.5, it becomes increasingly competative for neutron-rich nuclei due to an increase in phase space related to larger Q_β values.

6.1 General Picture

Electron capture, β decay and photodisintegration cost the core energy and reduce its electron density. As a consequence, the collapse is accelerated. An important change in the physics of the collapse occurs, as the density reaches $\rho_{\rm trap} \approx 4 \cdot 10^{11}$ g/cm^3. Then neutrinos are essentially trapped in the core, as their diffusion time (due to coherent elastic scattering on nuclei) becomes larger than the collapse time [31]. After neutrino trapping, the collapse proceeds homologously [126], until nuclear densities ($\rho_N \approx 10^{14}$ g/cm^3) are reached. As nuclear matter has a finite compressibility, the homologous core decelerates and bounces in response to the increased nuclear matter pressure; this eventually drives an outgoing shock wave into the outer core; i.e. the envelope of the iron core outside the homologous core, which in the meantime has continued to fall inwards at supersonic speed. The core bounce with the formation of a shock wave is believed to be the mechanism that triggers a supernova explosion, but several ingredients of this physically appealing picture and the actual mechanism of a supernova explosion are still uncertain and controversial. If the shock wave is strong enough not only to stop the collapse, but also to explode the outer burning shells of the star, one speaks about the 'prompt mechanism' [424]. However, it appears as if the energy available to the shock is not sufficient, and the shock will store its energy in the outer core, for example, by dissociation of nuclei into nucleons. Furthermore, this change in composition results to additional energy losses, as the electron capture rate on free protons is significantly larger than on neutron-rich nuclei due to the smaller Q-values involved. This leads to a further neutronization of the matter. Part of the neutrinos produced by the capture on the free protons behind the shock leave the star carrying away energy.

After the core bounce, a compact remnant is left behind. Depending on the stellar mass, this is either a neutron star (masses roughly smaller than 30 solar masses) or a black hole. The neutron star remnant is very lepton-rich (electrons and neutrinos), the latter being trapped as their mean free paths in the dense matter is significantly shorter than the radius of the neutron star. It takes a fraction of a second [57] for the trapped neutrinos to diffuse out, giving most of their energy to the neutron star during that process and heating it up. The cooling of the protoneutron star then proceeds by pair production of neutrinos of all three generations which diffuse out. After several tens of seconds the star becomes transparent to neutrinos and the neutrino luminosity drops significantly [56]. In the 'delayed mechanism', the shock wave can be revived by the outward diffusing neutrinos, which carry most of the energy set free in the gravitational collapse of the core [57] and deposit some of this energy in the layers between the nascent neutron star and the stalled prompt shock. This lasts for a few 100 ms, and requires about 1% of the neutrino energy to be converted into nuclear kinetic energy. The energy deposition increases the pressure behing the shock and the respective layers begin to expand, leaving between shock front and neutron star surface a region of low density, but rather high temperature. This region is called the 'hot neutrino bubble'. The persistent energy input by neutrinos keeps the pressure high in this region and drives the shock outwards again, eventually leading to a supernova explosion. It has been found that the delayed supernova mechanism is quite sensitive to physics details deciding about success or failure in the simulation of the explosion. Two quite distinct improvements have been proposed (convective energy transport [58,278] and in-medium modifications of the neutrino opacities [318,59]) which increase the efficiency of the energy transport to the stalled shock. Current one-dimensional supernova simulations, including sophisticated neutrino transport, fail to explode [189,263] (however, see [425]). The interesting question is whether the simulations explicitly requires multi-dimensional effects like rotation, magnetic fields or convection (e.g. [58,278]) or whether the microphysics input in the one-dimensional models is insufficient. It is the goal of nuclear astrophysics to improve on this microphysics input. The next section shows that core collapse supernovae are nice examples to demonstrate how important micro-physics input and progress in nuclear modelling can be. Late-stage stellar evolution is described in two steps. In the presupernova models the evolution is studied through the various hydrostatic core and shell burning phases until the central core density reaches values up to 10^{10} g/cm^3. The models consider a large nuclear reaction network. However, the densities involved are small enough to treat neutrinos solely as an energy loss source. For even higher densities this is no longer true as neutrino-matter interactions become increasingly important. In modern core-collapse codes neutrino transport is described self-consistently by spherically symmetric multigroup Boltzmann simulations. While this is computationally very challenging, collapse models have the advantage that the matter composition can be derived from Nuclear Statistical Equilibrium (NSE) as the core temperature and density are high enough to keep reactions mediated by the strong and electromagnetic interactions in equilibrium. This means that for sufficiently low entropies, the matter composition is dominated by the nuclei with the highest Q-values for a given Y_e. The presupernova models are the input for the collapse simulations which follow the evolution through trapping, bounce and hopefully explosion.

6.2 Weak-Interaction Rates and Presupernova Evolution

The collapse is a competition of the two weakest forces in nature: gravity versus weak interaction, where electron captures on nuclei and protons and, during a period of silicon burning, also β-decay play the crucial roles. Which nuclei are important? Weak-interaction processes become important when nuclei with masses $A \sim 55-60$ (pf-shell nuclei) are most abundant in the core (although capture on sd shell nuclei has to be considered as well). As weak interactions changes Y_e and electron capture dominates, the Y_e value is successively reduced from its initial value ~ 0.5. As a consequence, the abundant nuclei become more neutron rich and heavier, as nuclei with decreasing Z/A ratios are more bound in heavier nuclei. Two further general remarks are useful. There are many nuclei with appreciable abundances in the cores of massive stars during their final evolution. Neither the nucleus with the largest capture rate nor the most abundant one are necessarily the most relevant for the dynamical evolution: What makes a nucleus relevant is the product of rate times abundance.

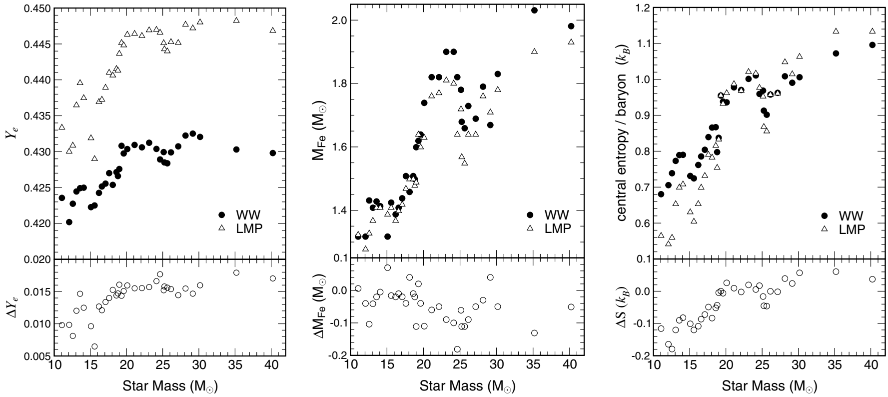

Fig. 12. Comparison of the center values of Y_e (left), the iron core sizes (middle) and the central entropy (right) for $11 - 40 M_\odot$ stars between the WW models, which used the FFN rates, and the ones using the shell model weak interaction rates (LMP).

To study the influence of the shell model rates, described in Sect. 3, on presupernova models Heger *et al.* [146,147] have repeated the calculations of Woosley and Weaver [438] keeping the stellar physics, except for the weak rates, as close to the original studies as possible. Figure 12 examplifies the consequences of the shell model weak interaction rates for presupernova models in terms of the three decisive quantities: the central Y_e value and entropy and the iron core mass. The central values of Y_e at the onset of core collapse increased by 0.01-0.015 for the new rates. This is a significant effect. We note that the new models also result in lower core entropies for stars with $M \leq 20 M_\odot$, while for $M \geq 20 M_\odot$, the new models actually have a slightly larger entropy. The iron core masses are generally smaller in the new models where the effect is larger for more massive stars ($M \geq 20 M_\odot$), while for the most common supernovae ($M \leq 20 M_\odot$) the reduction is by about 0.05 $M_\odot$.

Electron capture dominates the weak-interaction processes during presupernova evolution. However, during silicon burning, β decay (which increases Y_e) can compete and adds to the further cooling of the star. With increasing densities, β-decays are hindered as the increasing Fermi energy of the electrons blocks the available phase space for the decay. Thus, during collapse β-decays can be neglected.

We note that the shell model weak interaction rates predict the presupernova evolution to proceed along a temperature-density-Y_e trajectory where the weak processes are dominated by nuclei rather close to stability. Thus it will be possible, after radioactive ion-beam facilities become operational, to further constrain the shell model calculations by measuring relevant beta decays and GT distributions for unstable nuclei. References [146,147] identify those nuclei which dominate (defined by the product of abundance times rate) the electron capture and beta decay during various stages of the final evolution of a $15M_\odot$, $25M_\odot$ and $40M_\odot$ star.

6.3 The Role of Electron Capture During Collapse

In collapse simulations a very simple description for electron capture on nuclei has been used until recently, as the rates have been estimated in the spirit of the independent particle model (IPM), assuming pure Gamow-Teller (GT) transitions and considering only single particle states for proton and neutron numbers between $N = 20$–40 [49]. In particular this model assigns vanishing electron capture rates to nuclei with neutron numbers larger than $N = 40$, motivated by the observation [112] that, within the IPM, GT_+ transitions are Pauli-blocked for nuclei with $N \geq 40$ and $Z \leq 40$. However, as electron capture reduces Y_e, the nuclear composition is shifted to more neutron rich and to heavier nuclei, including those with $N > 40$, which dominate the matter composition for densities larger than a few 10^{10} gcm^{-3}. As a consequence of the model applied in the previous collapse simulations, electron capture on nuclei ceases at these densities and the capture is entirely due to free protons. This employed model for electron capture on nuclei is too simple and leads to incorrect conclusions, as the Pauli-blocking of the GT_+ transitions is overcome by correlations [222] and temperature effects [112,77]. At first, the residual nuclear interaction, beyond the IPM, mixes the pf shell with the levels of the sdg shell, in particular with the lowest orbital, $g_{9/2}$. This makes the closed $g_{9/2}$ orbit a magic number in stable nuclei ($N = 50$) and introduces, for example, a very strong deformation in the $N = Z = 40$ nucleus $^{80}\mathrm{Zr}$. Moreover, the description of the B(E2,$0^+ \to 2_1^+$) transition in $^{68}\mathrm{Ni}$ requires configurations where more than one neutron is promoted from the pf shell into the $g_{9/2}$ orbit [350], unblocking the GT_+ transition even in this proton-magic $N = 40$ nucleus. Such a non-vanishing GT_+ strength has already been observed for $^{72}\mathrm{Ge}$ ($N = 40$) [405] and $^{76}\mathrm{Se}$ ($N = 42$) [150]. Secondly, during core collapse electron capture on the nuclei of interest here occurs at temperatures $T > 0.8$ MeV, which, in the Fermi gas model, corresponds to a nuclear excitation energy $U \approx AT^2/8 > 5$ MeV; this energy is noticeably larger than the splitting of the pf and sdg orbitals ($E_{g_{9/2}} - E_{p_{1/2},f_{5/2}} \approx 3$ MeV). Hence, the configuration mixing of sdg and pf orbitals will be rather strong in those excited nuclear states of relevance for stellar electron capture. Furthermore, the nuclear state density at $E \sim 5$ MeV is already larger than 100/MeV, making a state-by-state calculation of the rates impossible, but also emphasizing the need for a nuclear model which describes the correlation energy scale at the relevant temperatures appropriately. This model is the Shell Model Monte Carlo (SMMC) approach [193,213] which describes the nucleus by a canonical ensemble at finite temperature and employs a Hubbard-Stratonovich linearization [171] of the imaginary-time many-body propagator to express observables as path integrals of one-body propagators in fluctuating auxiliary fields [193,213]. Since Monte Carlo techniques avoid

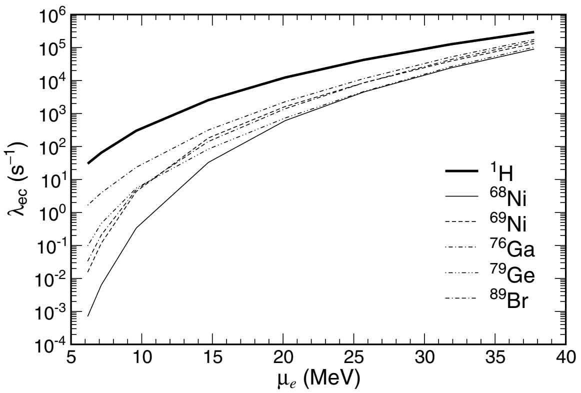

Fig. 13. Comparison of the electron capture rates on free protons and selected nuclei as function of the electron chemical potential along a stellar collapse trajectory taken from [263]. Neutrino blocking of the phase space is not included in the calculation of the rates.

an explicit enumeration of the many-body states, they can be used in model spaces far larger than those accessible to conventional methods. The Monte Carlo results are in principle exact and are in practice subject only to controllable sampling and discretization errors. To calculate electron capture rates for nuclei $A = 65$–112 SMMC calculations have been performed in the full pf-sdg shell, using a residual pairing+quadrupole interaction, which, in this model space, reproduces well the collectivity around the $N = Z = 40$ region and the observed low-lying spectra in nuclei like ^{64}Ni and ^{64}Ge. From the SMMC calculations the temperature-dependent occupation numbers of the various single-particle orbitals have been determined. These occupation numbers then became the input in RPA calculations of the capture rate, considering allowed and forbidden transitions up to multipoles $J = 4$ and including the momentum dependence of the operators. The method has been validated against capture rates calculated from diagonalization shell model studies for ^{64,66}Ni. The model is described in [222]; first applications in collapse simulations are presented in [226,160].

For all studied nuclei one finds neutron holes in the (pf) shell and, for $Z > 30$, non-negligible proton occupation numbers for the sdg orbitals. This unblocks the GT transitions and leads to sizable electron capture rates. Figure 13 compares the electron capture rates for free protons and selected nuclei along a core collapse trajectory, as taken from [263]. Dependent on their proton-to-nucleon ratio Y_e and their Q-values, these nuclei are abundant at different stages of the collapse. For all nuclei, the rates are dominated by GT transitions at low densities, while forbidden transitions contribute sizably at $\rho_{11} > 1$.

Simulations of core collapse require reaction rates for electron capture on protons, $R_p = Y_p\lambda_p$, and nuclei $R_h = \sum_i Y_i\lambda_i$ (where the sum runs over all

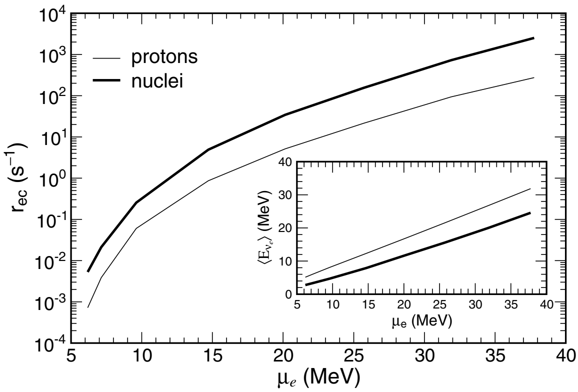

Fig. 14. The reaction rates for electron capture on protons (thin line) and nuclei (thick line) are compared as a function of electron chemical potential along a stellar collapse trajectory. The insert shows the related average energy of the neutrinos emitted by capture on nuclei and protons. The results for nuclei are averaged over the full nuclear composition (see text). Neutrino blocking of the phase space is not included in the calculation of the rates.

the nuclei present and Y_i denotes the number abundance of a given species), over wide ranges in density and temperature. While R_p is readily derived from [49], the calculation of R_h requires knowledge of the nuclear composition, in addition to the electron capture rates described earlier. In [226,160] a Saha-like NSE has been adopted to determine the needed abundances of individual isotopes and to calculate R_h and the associated emitted neutrino spectra on the basis of about 200 nuclei in the mass range $A = 45 - 112$ as a function of temperature, density and electron fraction. The rates for the inverse neutrino-absorption process are determined from the electron capture rates by detailed balance. Due to its much smaller $|Q|$-value, the electron capture rate on the free protons is larger than the rates of abundant nuclei during the core collapse (Fig. 13). However, this is misleading as the low entropy keeps the protons significantly less abundant than heavy nuclei during the collapse. Figure 14 shows that the reaction rate on nuclei, R_h, dominates the one on protons, R_p, by roughly an order of magnitude throughout the collapse when the composition is considered. Only after the bounce shock has formed does R_p become higher than R_h, due to the high entropies and high temperatures in the shock-heated matter that result in a high proton abundance. The obvious conclusion is that electron capture on nuclei must be included in collapse simulations. It is also important to stress that electron capture on nuclei and on free protons differ quite noticeably in the neutrino spectra they generate. This is demonstrated in Fig. 14 which shows that neutrinos from captures on nuclei have mean energies which are significantly less than those produced by capture on protons. Although capture on nuclei

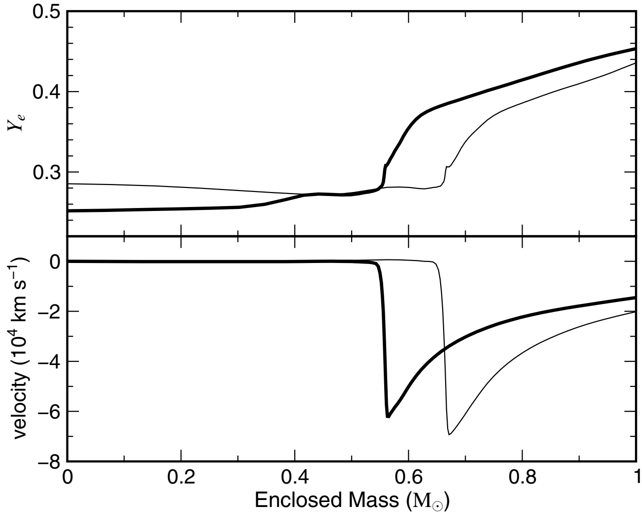

Fig. 15. The electron fraction and velocity as functions of the enclosed mass at bounce for a 15 $M_\odot$ model [146]. The thin line is a simulation using the Bruenn parameterization while the thick line is for a simulation using the combined LMP [224] and SMMC+RPA rate sets. Both models were calculated with Newtonian gravity.

under stellar conditions involves excited states in the parent and daughter nuclei, it is mainly the larger $|Q|$-value which significantly shifts the energies of the emitted neutrinos to smaller values. These differences in the neutrino spectra strongly influence neutrino-matter interactions, which scale with the square of the neutrino energy and are essential for collapse simulations [263, 189] (see below).

The effects of this more realistic implementation of electron capture on heavy nuclei have been evaluated in independent self-consistent neutrino radiation hydrodynamics simulations by the Oak Ridge and Garching collaborations [160,190]. The basis of these models is described in detail in [263] and [189]. Both collapse simulations yield qualitatively the same results. The changes compared to the previous simulations, which adopted the IPM rate estimate from [49] and hence basically ignored electron capturei on nuclei, are significant. Figure 15 shows a key result: In denser regions, the additional electron capture on heavy nuclei results in more electron capture in the new models. In lower density regions, where nuclei with $A < 65$ dominate, the shell model rates [223] result in less electron capture. The results of these competing effects can be seen in the first panel of Fig. 15, which shows the distribution of Y_e throughout the core at bounce (when the maximum central density is reached). The combination of increased electron capture in the interior with reduced electron capture in the outer regions causes the shock to form with 16% less mass interior to it and a 10% smaller velocity difference across the shock. This leads to a smaller mass of the homologuous core (by about 0.1 $M_\odot$). In spite of this mass reduction, the radius from which the shock is launched is actually displaced slightly outwards to 15.7 km from 14.8 km in the old models. If the only effect of the improvement in the treatment of electron capture on nuclei were to launch a weaker shock with more of the iron core overlying it, this improvement would seem to make a successful explosion more difficult. However, the altered gradients in density and lepton fraction also play an important role in the behavior of the shock. Though also the new models fail to produce explosions in the spherical symmetric limit, the altered gradients allow the shock in the case with improved capture rates to reach 205 km, which is about 10 km further out than in the old models. These calculations clearly show that the many neutron-rich nuclei which dominate the nuclear composition throughout the collapse of a massive star also dominate the rate of electron capture. Astrophysics simulations have demonstrated that these rates have a strong impact on the core collapse trajectory and the properties of the core at bounce. The evaluation of the rates has to rely on theory as a direct experimental determination of the rates for the relevant stellar conditions (i.e. rather high temperatures) is currently impossible. Nevertheless it is important to experimentally explore the configuration mixing between pf and sdg shell in extremely neutron-rich nuclei as such understanding will guide and severely constrain nuclear models. Such guidance is expected from future radioactive ion-beam facilities.

6.4 Neutrino-Induced Processes During a Supernova Collapse

While the neutrinos can leave the star unhindered during the presupernova evolution, neutrino-induced reactions become more and more important during the subsequent collapse stage due to the increasing matter density and neutrino energies; the latter are of order a few MeV in the presupernova models, but increase roughly approximately to the electron chemical potential [49,222] (see Fig. 4). Elastic neutrino scattering off nuclei and inelastic scattering on electrons are the two most important neutrino-induced reactions during the collapse. The first reaction randomizes the neutrino paths out of the core and, at densities of a few 10^{11} g/cm^3, the neutrino diffusion time-scale gets larger than the collapse time; the neutrinos are trapped in the core for the rest of the contraction. Inelastic scattering off electrons thermalizes the trapped neutrinos then rather fastly with the matter and the core collapses as a homologous unit until it reaches densities slightly in excess of nuclear matter, generating a bounce and launching a shock wave which traverses through the infalling material on top of the homologous core. In the currently favored explosion model, the shock wave is not energetic enough to explode the star, it gets stalled before reaching the outer edge of the iron core, but is then eventually revived due to energy transfer by neutrinos from the cooling remnant in the center to the matter behind the stalled shock. The trapped ν_e neutrinos will be released from the core in a brief burst shortly after bounce. These neutrinos can interact with the infalling matter just before arrival of the shock and eventually preheat the matter requiring less energy from the shock for dissociation [145]. The relevant preheating processes are charged- and neutral-current reactions on nuclei in the iron and also silicon mass range. So far, no detailed collapse simulation including preheating has been performed. The relevant cross sections can be calculated on the basis of shell model calculations for the allowed transitions and RPA studies for the forbidden transitions [387]. The main energy transfer to the matter behind the shock, however, is due to neutrino absorption on free nucleons. The efficiency of this transport depends strongly on the neutrino opacities in hot and very dense neutronrich matter [319]. It is likely also supported by convective motion, requiring multidimensional simulations [261]. Finally, elastic neutrino scattering off nucleons, mainly neutrons, also influences the efficiency of the energy transfer. A non-vanishing strange axialvector formfactor of the nucleon [279] will likely reduce the elastic neutrino-neutron cross section.

6.5 Type II Supernovae Nucleosynthesis

As discussed in the previous subsections, a number of aspects of the explosion mechanism are still uncertain and depend on Fe-core sizes from stellar evolution, electron capture rates, the supranuclear equation of state, the details of neutrino transport and Newtonian vs. general relativistic calculations, as well as multi-D effects [309,61,263,232,234,226,160,54,384,236,110,204,340, 240]. The present situation in supernova modeling is that self-consistent spherically-symmetric calculations (with the presently known microphysics) do not yield successful explosions based on neutrino energy deposition from the hot collapsed central core (neutron star) into the adjacent layers [309]. Even improvements in neutrino transport, solving the full Boltzmann transport equation for all neutrino flavors [263,384], and a fully general relativistic treatment [232,234,236] did not change this situation (see Fig. 16). Multi-D calculations [262,110,54,340,240], which still have to varify the quality of their neutrino transport schemes did not yet consider the possible combined action of rotation and magnetic fields.

The hope that the neutrino driven explosion mechanism could still succeed is based on uncertainties which affect neutrino luminosities (neutrino opacities with nucleons and nuclei [318,319,235], convection in the hot protoneutron star [201], as well as the efficiency of neutrino energy deposition (convection in the adjacent layers [426]). Figure 17 shows the temporal Y_e and entropy evolution of the innermost zone of a 20 $M_\odot$ SN II simulation [144], based on [232], but with varied neutrino opacities (reducing electron neutrino and antineutron scattering cross sections on nucleons or increasing the neutrino absorption cross sections for $\nu_e + n \to p + e^-$ and $\bar{\nu}_e + p \to n + e^+$) [235]. Such parameter studies permit successful delayed explosions and show options which may lead to success. This tests on the one hand variations in the uncertainty of neutrino cross sections [50,60,302,167] (but probably beyond the

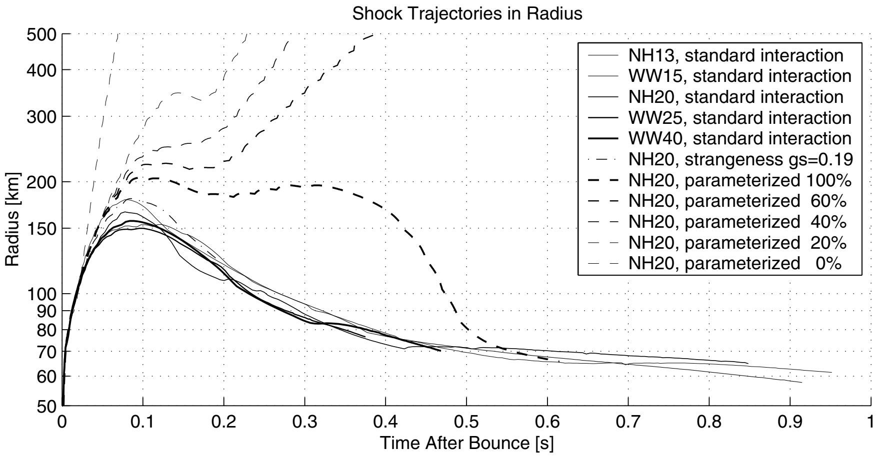

Fig. 16. A sequence of collapse calculations for different progenitor masses, showing in each case the radial position of the shock front after bounce [144]. We see that the shocks are strongest for the least massive stars. But in these 1D calculations all of them stall, recede and turn into accretion shocks, i.e. not causing successfull supernova explosions. A reduction in neutrino-nucleon elastic scattering, leading to higher luminosities, can cause explosions (performed for a $20M_\odot$ star).

permitted range as factors of about 2 are involved). Such tests can, however, also mimic multi-D effects in a spherically symmetric calculation. Decreased neutrino scattering cross sections cause a larger neutrino luminosity, similar to enhanced neutrino transport via proto-neutron star convection. Larger neutrino absorption cross sections act like an increase in energy absorption efficiency, similar to convection beyond the neutrino sphere. The interesting feature of the results is that in successful cases a zone with $Y_e > 0.5$ exists in the innermost ejecta (caused by neutrino interactions, see Fig. 17), leading to a proton-rich and alpha-rich freeze-out of explosive Si-burning with high entropies. This leads similar to the big bang, but on much more minute scales, to unburned He and H in the innermost ejecta (see Fig. 18).

As observations show typical kinetic energies of 10^{51} erg in supernova remnants, in the past light curve as well as explosive nucleosynthesis calculations were performed, even without a correct understanding of the explosion mechanism. They introduced (artificially) a shock of appropriate energy in the pre-collapse stellar model [437,375,438,377,165,395,314] and followed the explosive nucleosynthesis caused by the shock front passing through the layers up to the stellar surface. Such calculations lack self-consistency and cannot predict the ejected ^{56}Ni-masses from the innermost explosive Si-burning layers (powering supernova light curves by the decay chain ^{56}Ni-^{56}Co-^{56}Fe) due to missing knowledge about the detailed explosion mechanism and therefore the mass cut between the neutron star and supernova ejecta. However, the

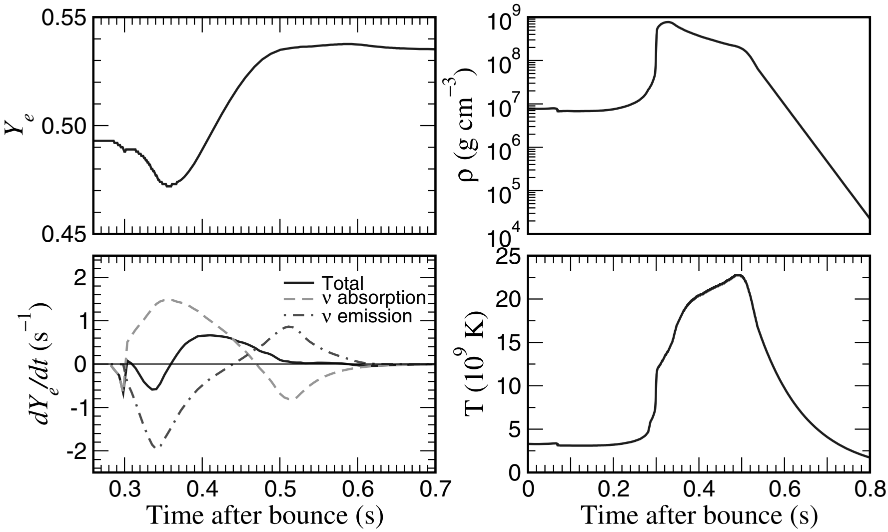

Fig. 17. Hydrodynamic simulations with varied (reduced) neutrino opacities (scattering cross sections on nucleons reduced by 60%) lead to larger neutrino luminosities and make successful supernova explosions possible [144]. Here we see the time evolution after core bounce of the innermost ejected layer from a 20M$_\odot$ supernova progenitor. Y_e=$<Z/A>$) indicates the neutron-richness of ejected matter, dY_e/dt the time derivative due to the different reactions involving free protons and neutrons $\nu_e + n \leftrightarrow p + e^-$ and $\bar{\nu}_e + p \leftrightarrow n + e^+$ in the directions of neutrino (and antineutrino) absorption or emission. $\rho(t)$ and $T(t)$ the indicate density and temperature. What can be noticed is that Y_e is strongly dependent on both neutrino absorption and emission reactions and that apparently in these exploding models Y_e in the innermost zones is larger than 0.5, i.e. proton-rich.

intermediate mass elements Si-Ca are only dependent on the explosion energy and the stellar structure of the progenitor star, while abundances for elements like O and Mg are essentially determined by the stellar progenitor evolution. Thus, when moving in from the outermost to the innermost ejecta of a SN II explosion, we see an increase in the complexity of our understanding, depending (a) only on stellar evolution, (b) on stellar evolution and explosion energy, and (c) on stellar evolution and the complete explosion mechanism (see Fig. 19). The possible complexity of the explosion mechanism, including multi-D effects, should not affect this (spherically symmetric) discussion of explosive nucleosynthesis severely. 2D-calculations [204] led to spherically symmetric shock fronts after the explosion is initiated, thus causing spherical symmetry in explosive nuclear burning when passing through the stellar layers. Only after the passage of the shock front, the related temperatures decline and freeze-out of nuclear reactions, the final nucleosynthesis products can be distributed in non-spherical geometries due to mixing by hydrodynamic instabilities. Thus, the total mass of nucleosynthesis yields shown in Fig. 19 should

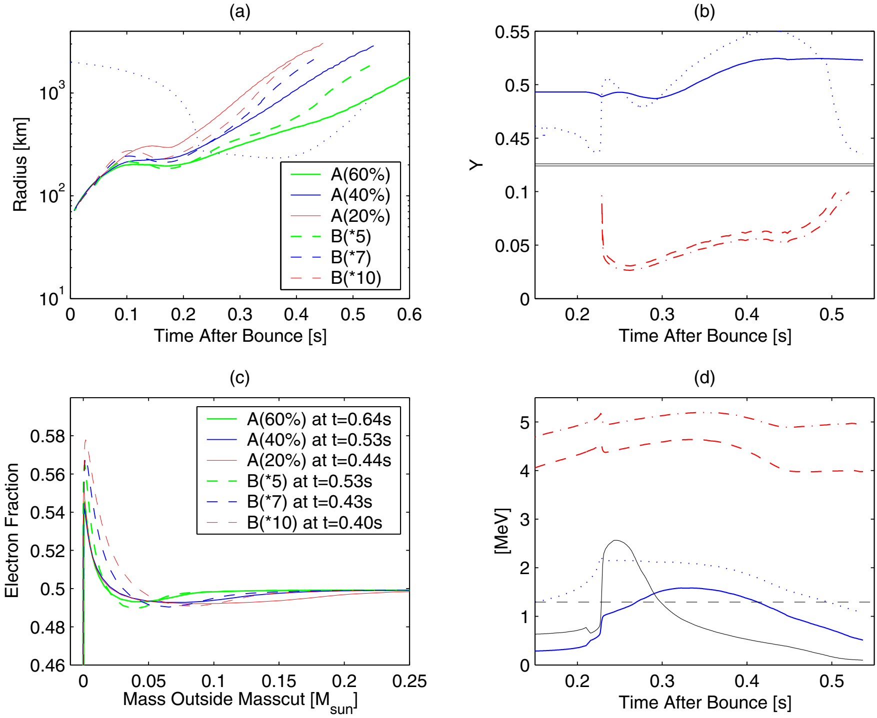

Fig. 18. Details from a core collapse and explosion simulation with six variations in neutrino transport, (A) reduction of neutrino-nucleon scattering cross sections to a given percentage of the literature value, (B) multiplication of the neutrino and antineutrino absorption cross sections on nucleons by a given factor [144]. Shown are (a) the radius of the shock front for the different models, (b) the electron fraction Y_e, i.e. the net electron (or proton) to nucleon ratio, for the innermost ejected mass zone of one simulation as a function of time in comparison to a value where neutrino emission and absorption rates are in a chemical equilibrium, (c) Y_e, measuring the neutron or proton-richness of matter, for a number of ejected mass zones outside the mass cut, (d) the neutrino chemical potential and the matter temperature.

not be changed, only its geometric distribution. An exception is probably related to the very innermost ejected zones where the explosion mechanism is influencing the outcome. The correct prediction of the amount of Fe-group nuclei ejected (which includes also one of the so-called alpha elements, i.e. Ti) and their relative composition depends directly on the explosion mechanism and the size of the collapsing Fe-core. Three types of uncertainties are inherent in the Fe-group ejecta, related to (i) the total amount of Fe (group) nuclei ejected and the mass cut between neutron star and ejecta, mostly measured by ^{56}Ni decaying to ^{56}Fe, (ii) the total explosion energy which influences the entropy of the ejecta and with it the amount of radioactive ^{44}Ti as well as

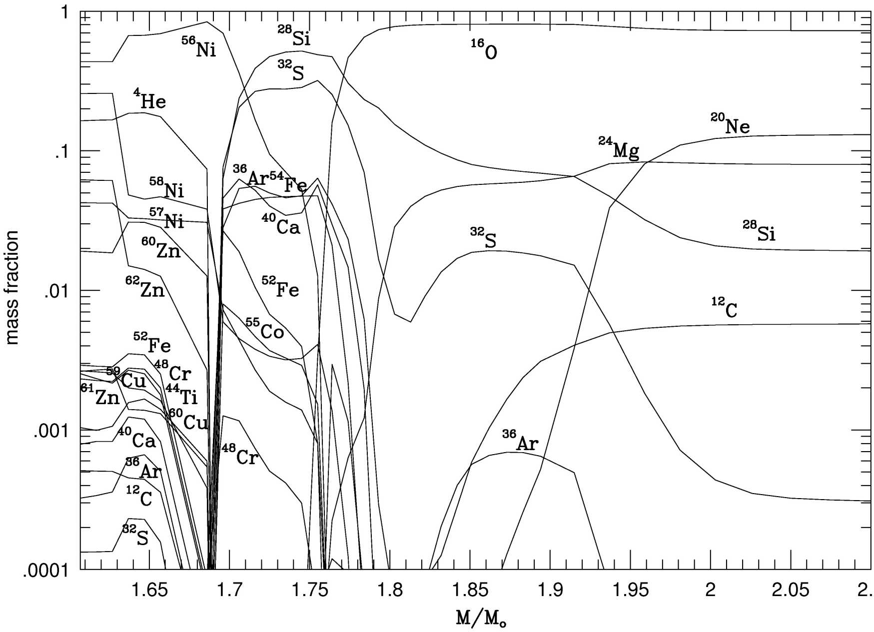

Fig. 19. Isotopic composition for the explosive C-, Ne-, O- and Si-burning layers of a core collapse supernova from a $20M_\odot$ progenitor star with a $6M_\odot$ He-core and an induced net explosion energy of 10^{51} erg, remaining in kinetic energy of the ejecta [377]. $M(r)$ indicates the radially enclosed mass, integrated from the stellar center. The exact mass cut in $M(r)$ between neutron star and ejecta and the entropy and Y_e in the innermost ejected layers depend on the details of the (still open) explosion mechanism. The abundances of O, Ne, Mg, Si, S, Ar, and Ca dominate strongly over Fe (decay product of ^{56}Ni), if the mass cut is adjusted to $0.07M_\odot$ of ^{56}Ni ejecta as observed in SN 1987A.

^{48}Cr, the latter decaying later to ^{48}Ti and being responsible for elemental Ti, and (iii) finally the neutron richness or $Y_e = < Z/A >$ of the ejecta, dependent on stellar structure, electron captures and neutrino interactions. Y_e influences strongly the ratios of isotopes 57/56 in Ni(Co,Fe) and the overall elemental Ni/Fe ratio, the latter being dominated by ^{58}Ni and ^{56}Fe.

In the inner ejecta, corresponding to case (c) in the discussion above, which experience explosive Si-burning, such (not self-consistent) calculations made use of a Y_e of the order 0.4989 to 0.494. This omitted possible alterations of Y_e via neutrino reactions during the explosion. This can cause huge changes in the Fe-group composition [74,237] for ^{56}Ni and the neutron-rich isotopes ^{57}Ni, ^{58}Ni, ^{59}Cu, ^{61}Zn, and ^{62}Zn. The abundances of ^{40}Ca, ^{44}Ti, ^{48}Cr, and ^{52}Fe are affected by the entropy obtained in those mass zones. Present calculations [235] (see also Figs. 16 and 18) show that apparently the innermost zones in successfully exploding models avoid too neutron-rich ejecta when including neutrino-induced reactions. This permits an Fe-group composition consistent with supernova observations [377]. The slightly proton-rich environment leads to an alpha-rich and proton-rich freeze-out. The density is apparently not sufficient for an rp-process and unburned hydrogen survives deep in the ejected envelope. The pending understanding of the explosion mechanism affects the amount of Fe-group nuclei ejected (which includes also one of the so-called alpha elements, i.e. Ti) and possible r-process yields for SNe II (see Sect. 7). The pending understanding of the explosion mechanism also affects possible r-process yields for SNe II [364,436,306,108,254,282,383, 412,354,367,384]. A more detailed discussion is given in Sect. 7.

7 The r-Process

The heavy elements in nature are made by neutron capture [353] and (at least) two types of different environments are required [55,67]. (i) A process with small neutron densities, experiencing long neutron capture timescales in comparison to β-decays ($\tau_\beta < \tau_{n,\gamma}$, slow neutron capture or the s-process), causing abundance peaks in the flow path at nuclei with small neutron capture cross sections, i.e. stable nuclei with closed shells at magic neutron numbers [196,8] (as discussed in Sect. 1.3 as a consequence of (α, n)-reactions in hydrostatic He-burning). (ii) A process with high neutron densities and temperatures, experiencing rapid neutron captures and the reverse photodisintegrations with $\tau_{n,\gamma}, \tau_{\gamma,n} < \tau_\beta$, causing abundance peaks due to long β-decay half-lives where the flow path comes closest to stability (again at magic neutron numbers, but for unstable nuclei). During the latter rapid neutron-capture process (r-process) it is possible that highly unstable nuclei with short half-lives are produced [198], leading also to the formation of the heaviest elements in nature like Th, U, and Pu. The r-process path involves nuclei near the neutron drip-line. Far from stability, neutron shell closures are encountered for smaller mass numbers A than in the valley of stability. Therefore, if r-process peaks are due to long β-decay half-lives of neutron-magic nuclei, the r-process abundance peaks are shifted in comparison to the s-process peaks (which occur for neutron shell closures at the stability line).

Besides this basic understanding, the history of r-process research has been quite diverse in suggested scenarios [345,80,411,198]. If starting with a seed distribution somewhere around A=50-80 before rapid neutron-capture sets in, the operation of an r-process requires 10 to 150 neutrons per seed nucleus to form all heavier r-nuclei. The question is which kind of environment can provide such a supply of neutrons to act before decaying with a 10 min half-life. The logical conclusion is that only explosive environments, producing or releasing these neutrons suddenly, can account for such conditions. Two astrophysical settings are suggested most frequently, related to two entropy options discussed in more detail in the following sections: (i) Type II supernovae (SNe II) with postulated high-entropy ejecta [436,364, 108,282,412,383,367,384,439] and (ii) neutron star mergers or similar events (like axial jets in supernova explosions) which eject neutron star matter with low-entropies [229,256,93,329,109,331,330].

7.1 The Role of Nuclear Physics

The main aspects of an r-process are neutron captures, photodisintegrations, and β-decays. An $(n,\gamma)\rightleftharpoons(\gamma,n)$ equilibrium exists if neutron captures and photodisintegrations are fast in comparison to beta-decays between isotopic chains, leading to a distribution of abundances in each isotopic chain governed by a chemical equilibrium $\mu_n + \mu_{Z,A} = \mu_{Z,A+1}$ in a Boltzmann gas. This causes abundance ratios of neighboring isotopes $Y(Z,A+1)/Y(Z,A) = f(n_n,T,S_n)$ to depend only on neutron density n_n, temperature T, and the neutron separation energy S_n (or reaction Q-value for the appropriate neutron capture) [345,216]. The maximum in each isotopic chain occurs when $Y(Z,A+1)/Y(Z,A)$ changes from a rising to a declining ratio (i.e. from >1 to <1). A ratio of 1 defines a universal $S_{n,max}$ for all maxima, independent of the specific isotopic chain. Thus, the combination of a neutron density n_n and temperature T determines the r-process path (connecting the isotopes with the maximum abundance in each isotopic chain) located at the same neutron separation energy $S_{n,max}$. During an r-process event exotic nuclei with neutron separation energies of 4 MeV and less are important, up to S_n=0, i.e. the neutron drip-line. This underlines that the understanding of nuclear physics far from stability is a key ingredient and the knowledge of S_n (or equivalently nuclear masses) [268,2,17,299,18] determines the r-process path. While in recent years new Hartree-Fock(-Bogoliubov) or relativistic mean field approaches have been addressing this question [73,92,322,28,130,285,132,335, 408], the FRDM model [268] still seems to provide the best reproduction of known masses [130].

The β-decay rates $\lambda_\beta^{Z,A}$ are related to the half-lives of very neutron-rich nuclei via $\lambda_\beta = ln(2)/\tau_{1/2}$. The abundance flow from each isotopic chain to the next is governed by β-decays. We can introduce a total abundance in each isotopic chain $Y(Z)=\sum_A Y(Z,A)$. Process timescales in excess of β-decay half-lives lead to a steady-flow equilibrium $Y(Z)\lambda_\beta(Z) = \mathrm{const}$ [216] shown most clearly in Fig. 2 of [108], where $\lambda_\beta(Z)$ is an abundance averaged half-life. Thus, in that case the knowledge of nuclear masses (S_n), determining the r-process path, and half-lives ($\tau_{1/2}$) [269,94,42,252,41], determining the relative abundances of each isotopic chain, would be sufficient to predict the whole set of abundances [301]. This seems to be the case in the regions between the r-process peaks (neutron magic numbers) and in the low-mass tails of the $A\simeq130$ and $A\simeq195$ peaks of the solar-system r-process abundances [216]. Nuclei in the r-process path with the longest half-lives of the order 0.2-0.3 s, related to the abundance peaks themselves, do not fulfill the steady flow requirement. In this case the coupled set of differential equations $\dot{Y}(Z) = \lambda_\beta(Z-1)Y(Z-1) - \lambda_\beta(Z)Y(Z)$ has to be solved for all isotopic chains Z, if an $(n,\gamma)\rightleftharpoons(\gamma,n)$ equilibrium applies. In the most general case of (astrophysical) environment conditions, one has to solve a full set of differential equations for all nuclei from stability to the neutron drip-line [80,411,108], including individual neutron captures [311,129,406,312, 313], photodisintegrations, and beta-decays. However, from existing results one finds that an $(n, \gamma) \rightleftharpoons (\gamma, n)$ equilibrium is attained before the freeze-out of neutron abundances and photodisintegrations (for decreasing temperatures). For small β-decay half-lives, encountered in between magic numbers and for small Z's at magic numbers, also the steady-flow approximation seems applicable. The freeze-out from equilibrium can follow two extreme options: (i) an instantaneous freeze-out, just followed by the final decay back to stability, where also β-delayed properties (neutron emission and fission) are needed and can depend strongly on the beta strength-function [374,257,80,358,296, 41,297]. (ii) In the more general case of a slow freeze-out also neutron captures can still affect the final abundance pattern [355,108,94]. If the latter is the case, individual neutron capture cross sections are required [258,312,313]. Fission will set in during an r-process, when neutron-rich nuclei are produced at excitation energies beyond their fission barriers [373,374,80]. The role of β-delayed and neutron-induced fission has two aspects. For nuclei with neutron separation energies of the order 2 MeV, neutron capture will produce compound nuclei with much smaller excitation energies than those obtained in β-decay. However, the rates of neutron-induced processes (responsible also for the $(n, \gamma) \rightleftharpoons (\gamma, n)$ equilibrium) are orders of magnitude larger than beta-decay rates. Thus, it is possible that neutron-induced fission can compete with beta-delayed fission (see Fig. 20). Fission determines on the one hand the heaviest nuclei produced in an r-process [374,80,109,281,248] and on the other hand also the fission yields fed back to lighter nuclei [109,296,271].

In some environments, like e.g. in supernovae, a high neutrino flux of different flavors is available. This gives rise to neutral and charged current interactions with nucleons and nuclei, i.e. elastic/inelastic scattering or electron neutrino or antineutrino capture on nuclei, e.g. $\nu_e + (Z, A) \to (Z+1, A) + e^-$, (giving results similar to β transformations). During freeze-out the first mechanism redistributes abundances to nearby mass numbers [209,305,149] similar to spallation. Neutrino capture for high neutrino fluxes could mimic fast β^--decays, possibly accelerating an r-process to heavy elements [283,117,253,307, 260,220]. The effects of exotic neutrino properties are discussed in [211,254, 298]. Site-independent classical analyses [216,81], based on neutron number density n_n, temperature T, and duration time τ, as well as entropy based calculations with the parameters entropy S, Y_e, and expansion timescale τ [164,108] (to be discussed in the following subsection) have shown that the solar r-process can be fit by a continuous superposition of components with neutron separation energies at freeze-out in the range 4-1 MeV [81, 108]. These are the regions of the nuclear chart (extending to the neutron drip-line) where nuclear structure, related to masses far from stability and beta-decay half-lifes [301] has to be investigated. They include predominantly nuclei not accessible in laboratory experiments to date but hopefully in the

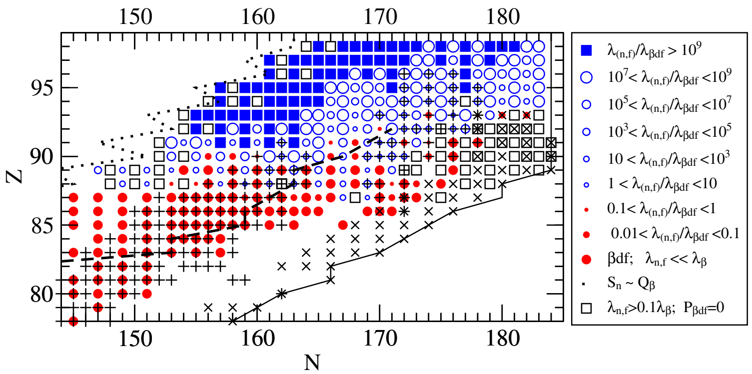

Fig. 20. Ratios of neutron-induced to beta-delayed fission for nuclei of interest in r-process calculations [297]. These exploratory results were obtained with the fission barriers by Howard and Möller [170]. Different barrier heights [281,248] will lead to different total fission rates. However, it was shown here that neutron-induced fission is a viable ingredient for r-process studies and should not be neglected in comparison to beta-delayed fission.

foreseeable future (RIKEN, GSI, RIA). In addition, expanding theoretical efforts with increasingly sophisticated means are required, addressing also neutrino-induced reactions [220,149,225,42] and fission properties [281,248, 296,297]. The actual astrophysical realization of the relevant conditions will be discussed in the following sections.

7.2 Working of the r-Process and Required Environment Properties

The parameter which determines whether an r-process occurs is the neutrons per seed ratio, see e.g. [108]. The r-process requirement of 10 to 150 neutrons per r-process seed (in the Fe-peak or somewhat beyond), permitting to produce nuclei with $A > 200$, can be translated into the parameters entropy S, Y_e and expansion timescale τ of a heated blob of material in astrophysical events, consisting of a net ratio of protons to neutrons (or total nucleons) with a given expansion history. At low entropies (without an alpha-rich freeze-out of charged-particle reactions) this is equivalent to Y_e $=<Z/A>$=0.12-0.3. Such a high neutron excess is only possible for high densities in neutron stars under beta equilibrium ($e^- + p \leftrightarrow n + \nu$, $\mu_e + \mu_p = \mu_n$), based on the high electron Fermi energies which are comparable to the neutron-proton mass difference [256]. Deviations from this straightforward balance are only possible if one stores large amounts of mass in N=Z nuclei with small neutron capture cross sections (e.g. ^{4}He), leaving then all remaining neutrons for a few heavy seed nuclei. This phenomenon is known as an extremely α-rich freeze-out in complete Si-burning and corresponds to a weak link of reactions between the light nuclei (n, p, α) and heavier nuclei at low densities. The links across the particle-unstable A=5 and 8 gaps are only possible via the three-body reactions $\alpha\alpha\alpha$ and $\alpha\alpha n$ to ^{12}C and ^{9}Be, whose reaction rates show a quadratic density dependence. The entropy ($\propto T^3/\rho$ in radiation dominated matter) can be used as a measure of the ratio between the remaining He mass fraction and heavy nuclei. A well known case is the big bang where under extreme entropies essentially only ^{4}He is left as the heaviest nucleus available. Somewhat lower entropies permit the production of (still small) amounts of heavy seed nuclei. Then, even moderate values of Y_e=0.4-0.5 can lead to high ratios of neutrons to heavy nuclei for entropies in excess of 200 k_B per baryon. and neutron captures can proceed to form the heaviest r-process nuclei [434,258, 364,436,164,108].

These two environments represent a normal (low-entropy) and an α-rich (high-entropy) freeze-out from charged-particle reactions before the dominance of neutron-induced reactions. Towards low entropies the transition to a normal freeze-out occurs, leading to a negligible entropy dependence of the neutron to seed ratio.

7.3 r-Process Sites

Type II Supernovae. The apparently most promising mechanism for supernova explosions after Fe-core collapse of a massive star is based on neutrino heating beyond the hot proto-neutron star via the dominant processes $\nu_e + n \rightarrow p + e^-$ and $\bar{\nu}_e + p \rightarrow n + e^+$ with a (hopefully) about 1% efficiency in energy deposition. The neutrino heating efficiency depends on the neutrino luminosity, which in turn is affected by neutrino opacities. Aspects of the explosion mechanism are still uncertain (see Sect. 6).

If SNe II are also responsible for the solar r-process abundances, given the galactic occurance frequency, they would need to eject about 10^{-5} $M_\odot$ of r-process elements per event (if all SNe II contribute equally). The scenario is based on the so-called “neutrino wind”, i.e. a wind of matter from the neutron star surface (within seconds after a successful supernova explosion) caused by neutrinos streaming out from the hot neutron star [436,364,164, 306,260,292,383,367,384,439].

This high entropy neutrino wind is expected to lead to a superposition of ejecta with varying entropies. If a sufficiently high entropy range is available, an abundance pattern as shown in Fig. 21 can be obtained [108]. However, the r-process by neutrino wind ejecta of SNe II faces two difficulties. (i) Whether the required high entropies for reproducing heavy r-process nuclei can really be attained in supernova explosions has still to be verified [282,383,367,384]. Presently it seems that only (unrealistically?) large or compact neutron stars with masses in excess of 2 $M_\odot$ can provide the high entropies required. (ii) The mass region 80–110 experiences difficulties to be reproduced adequately [108,412], reflecting rather abundances determined by alpha separation energies after an alpha-rich freeze-out than neutron separation energies. It has to be seen whether the inclusion of non-standard neutrino properties [254] can

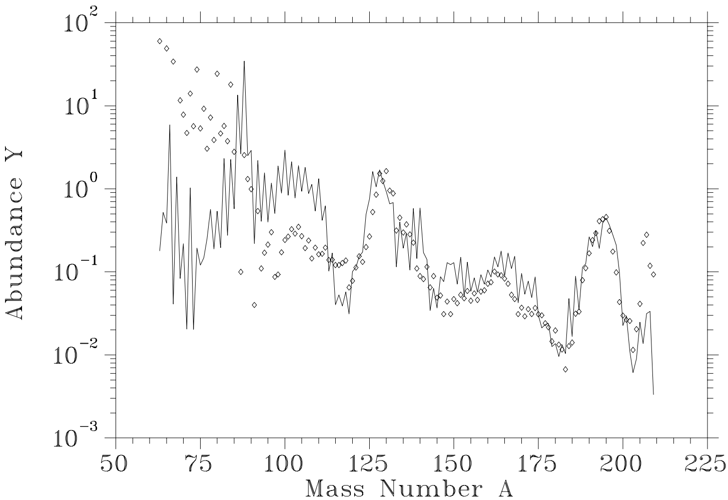

Fig. 21. Fit to solar r-process abundances (open rhombus) with the ETFSI-1 mass formula [2], making use of a superposition of entropies. These calculations were performed with $Y_e = 0.45$, but similar results are obtained in the range $0.30 - 0.49$, only requiring a scaling of entropy. The trough below $A \simeq 130$ can be avoided by the changing of shell effects far from stability. The strong deficiencies in the abundance pattern below $A \simeq 110$ are due to an α-rich freeze-out where essentially no neutrons are left. This is related to the Y_e of the astrophysical scenario rather than to nuclear structure [108].

cure both difficulties or lower Y_e zones can be ejected from SNe II, as recently claimed [354] from assumed prompt explosion calculations, lacking a proper neutrino transport. Present supernova models face the problem that the entropies required seem not yet attainable, unless ad hoc assumptions [367,439] can be verified.

Neutron Star Mergers. An alternative site for the heavy r-process nuclei are neutron-star ejecta, like e.g. in neutron star mergers [229,93,109]. The binary system, consisting of two neutron stars, looses energy and angular momentum through the emission of gravitational waves and merges finally. The measured orbital decay gave the first evidence for the existence of gravitational radiation [365,385,242] and indicates timescales of the order of 10^8 y or less (dependent on the excentricity of the system). The rate of NS mergers has been estimated to be of the order $10^{-6} - 10^{-4}$ y^{-1} per galaxy [93,200]. A merger of two NS can also lead to the ejection of neutron-rich material [191,329,331,330] of the order of $10^{-(2-3)}\mathrm{M}_\odot$ in Newtonian and relativistic calculations [290]. The decompression of cold neutron-star matter has been studied [229,256]; however, a hydrodynamical calculation coupled with a complete r-process calculation has not been undertaken, yet.

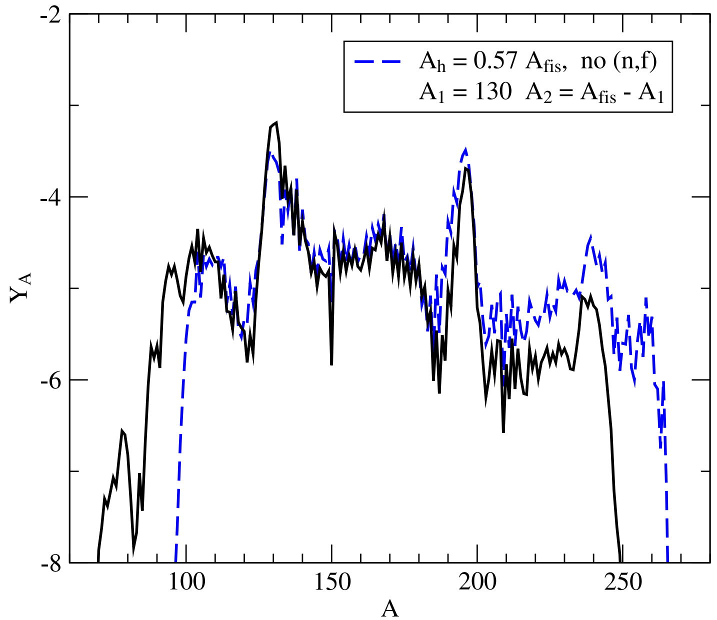

Fig. 22. Composition of ejecta from a neutron star merger event (Σ mass fractions =1) with an average Y_e=0.10. Either only beta-delayed fission or both beta-delayed and neutron-induced fission were employed, varying also the fission yield distribution [297]. The effect of these different treatments is obviously seen for A>240, but more importantly for A<130 and underlines the impact of fission barriers and the fission yield distribution. These effects are directly related to all events with very high neutron densities, i.e. neutron star ejecta in mergers or jets where strong fission cycling takes place.

Figure 22 shows the composition of ejecta from a NS merger [109,329,296, 297]. It is seen that the large amount of free neutrons (up to $n_n \simeq 10^{32}$ cm^{-3}) available in such a scenario leads to the build-up of the heaviest elements and also to fission cycling within very short timescales, while the flow from the Fe-group to heavier elements "dries up". This leads to a composition void of abundances below the A$\simeq$130 peak, which is, however, dependent on detailed fission yield predictions [297].

r-Process Outlook. At present, the suggested r-process sources, supernovae and neutron star mergers, did not yet prove to be "the" main-component r-process source without reasonable doubt. A discussion of the advantages and disadvantages of both possible r-process sources (SNe II vs. neutron star mergers) is given in [308,330]. Self-consistent core collapse supernovae do not give explosions [309,263,232], yet, but parameter studies with neutrino opacities permit to "fit" the correct explosion behavior [233]. Thus, there is no way to predict whether the required entropies for an r-process can be obtained [412,383,367,384,439]. Neutron star merger calculations give the correct mass ejection [329], but relativistic calculations need to be followed up [290,291] and Y_e needs to be treated with weak interactions and neutrino transport included self-consistently.

The two possible sites discussed above (SNe II and neutron star mergers) have different occurance frequencies and different amounts of r-process ejecta, if a successful r-process actually occurs. These properties will enter into the enrichment pattern of r-process elements in galactic evolution. Inhomogeneous galactic evolution models in the very early phases of the Galaxy [183,6,7] will finally indicate that either one of the above mentioned sites or both in combination can meet the observational contraints from the scatter of r-process to Fe ratios in “low metallicity stars” as a function of metallicity, i.e. the $(\mathrm{Fe/H})/(\mathrm{Fe/H})_\odot$ ratio.

Nuclear properties far from stable nuclei are of prime importance in the astrophysical r-process. Due to the (partial) equilibrium nature at high temperatures and neutron densities, the dominant influence is given by nuclear masses and β-decay properties (half-lives, delayed neutron emission and fission). Neutron-induced fission can play a competing role to beta-delayed fission. All these aspects need a better future understanding, including the role of neutrino-induced reactions, as they enter directly in the resulting r-process yields and abundance distributions.

8 Nuclear Processes in Explosive Binary Systems

Over the last twenty years thermonuclear explosions in accreting binary star systems have been an object of considerable attention. The basic concept of the thermonuclear runaway as the driving explosion mechanism seems reasonably well understood but there are still considerable discrepancies between the predicted observables and the actual observations. The proposed mechanism involves binary systems with one (or two) degenerate objects, like white dwarfs or neutron stars and is characterized by the revival of the dormant objects via mass overflow and accretion from the binary companion. This leads to explosive events like novae, type Ia supernovae, X-ray bursts, and X-ray pulsars. The characteristic differences in the luminosity, time scale, and periodicity depend on the accretion rate and on the nature of the accreting object. Low accretion rates lead to a pile-up of unburned hydrogen, causing the ignition of hydrogen burning via pp-chains and CNO-cycles with pycnonuclear enhancements of the reactions after a critical mass layer is attained. On white dwarfs this triggers nova events, on neutron stars it results in X-ray bursts. High accretion rates above a critical limit on the other hand cause high temperatures in the accreted envelope and less degenerate conditions, which result in stable H-burning or only weak flashes. High accretion rates on white dwarfs cause supernovae type Ia events, which are not discussed here in detail as they do not lead to nuclei far from stability (for recent reviews see [372,154]). Accretion rates high enough for stable burning on a highly magnetic neutron star lead to X-ray pulsars. The present modeling of the accretion and thermonuclear runaway process is still in infancy mainly due to the complex aspects of the explosion mechanism which requires three-dimensional modeling techniques for realistic treatment [202, 111]. Besides the complexities of asymmetric ignition and burning front development and the issues of rapid convection and mixing during the explosion large uncertainties are also associated with the microscopic nuclear physics component of the process. The nuclear energy generation provides the observed luminosity of the event, the combination of rapid mixing, convection and far of stability nucleosynthesis is responsible for the observed abundance distribution in the ejected material. These events are the largest thermonuclear explosions in the universe, they may synthesize a number of important isotopes in our universe, and they serve as laboratories for nuclear physics at extreme temperatures and densities.

8.1 Nova Explosions

Novae have been interpreted as thermonuclear runaways on the surface in close binary star systems [391,121]. Accretion processes or mass exchange between the two binary stars can take place when at least one of the stars fills its Roche Lobe which is the gravitational equipotential surface enclosing both stars. The matter of the extended star flows through the Roche Lobe onto the surface of the second companion which represents a deeper gravitational potential. Novae are identified as white dwarfs in binary systems, accreting matter from the binary companion star in a burning stage close to main sequence H-burning which is filling its Roche Lobe. The accreted material forms a thin, but high density electron degenerate envelope at the surface of the white dwarf. Dredge up of white dwarf material (^{4}He, ^{12}C, ^{16}O in the case of an CO-white dwarf, ^{16}O, ^{20}Ne, and ^{24}Mg in the case of an ONeMg-white dwarf) into the envelope leads to an enrichment of the accreted material in heavier isotopes [125]. The exact nature of the mixing mechanism is still under debate but it has recently been suggested that mixing of white dwarf material into the accreted envelope can be sufficiently enhanced by interfacial breaking gravity wave interaction [328,4].

After a "critical" mass has been accreted, thermonuclear ignition takes place at the bottom of the accreted envelope. This depends critically on the mass of the white dwarf and the accretion rate which determines the pressure conditions at the bottom of the envelope. The ignition presumably occurs via the pp-chains, at degenerate electron gas conditions this causes a rapid increase in temperature at constant pressure and density. This "thermonuclear runaway" is further enhanced by the subsequent ignition of the hot CNO cycles on the high abundances of ^{12}C and ^{16}O until the degeneracy is lifted after the Fermi temperature T_F has been reached. The Fermi temperature depends on the electron density $n_e \propto \rho Y_e$

$$T_F = 3.03 \cdot 10^5 \, (\rho Y_e)^{2/3} \,, \tag{33}$$

with ρ in g/cm^3 and T_F in K. Thus, higher densities of the material lead to higher peak temperatures which can be reached in the thermal runaway before degeneracy is lifted. However, if the shell temperature is rising rapidly the peak temperature can exceed the Fermi temperature before the electron gas is sufficiently degenerate to initiate expansion. Due to the rapid temperature increase at the bottom of the envelope a convective zone develops which gradually grows to the surface as the temperature continues to increase. This allows rapid energy transport to the surface within the convective time scale of $t_{conv} \approx 10^2$ s. Within that short timescale also an appreciable fraction of the long-lived β^+ emitters which are produced by the hot CNO cycles is carried to the surface. The release of decay energy further increases the luminosity to values above 10^5 L$_\odot$. The large amount of energy deposited in the outer layers on the short convective time scale, coupled with high luminosity often exceeding the Eddington limit L$_{edd}$ [348] causes rapid expansion of the outer layers and the ejection of the outer shells. (The Eddington limit is the luminosity where the average force from outstreaming photons through matter is equal to the gravitational force acting on the same mass zone.)

Typical novae are characterized by thermal runaways with densities of approximately $\rho \approx 10^3$ g/cm^3 and typical peak temperatures between $1 \cdot 10^8$ K and $4 \cdot 10^8$ K [352]. The main observables for a reliable interpretation of the explosion mechanisms are the nova light curve and the abundance distribution in the ejected material. The luminosity yields information on the total energy release from nuclear reaction and decay processes but it also gives information about the time scale of the thermonuclear runaway. The abundance observation gives evidence for the on-site nucleosynthesis but may also provide a tool for monitoring the rather complex mixing and convective mechanisms prior and during the explosion [328,4]. For a reliable interpretation of such observations improved nuclear physics input in the present nova models is crucial. The actual ignition temperature for novae is well below these peak temperatures. Rates of many nuclear reactions are therefore needed at energies below a few hundred keV to get a complete description of the ignition process in the various accreted layers of material. The main energy generation in nova comes from the hot (or β-limited) CNO cycles ^{12}C(p,γ)^{13}N(p,γ)^{14}O(β,ν)^{14}N(p,α)^{15}O(β,ν)^{15}N(p,α)^{12}C and is determined by the rather long life times of the ^{14}O and ^{15}O oxygen isotopes. This causes enrichment in ^{14}O and ^{15}O which is observed as nitrogen enrichment in the ejected material. The actual energy generation rate is limited by the β-decay rates but is also affected by the hydrogen and CNO fuel available. A more quantitative interpretation of the actual nucleosynthesis therefore requires detailed knowledge of the associated convective processes which may transport freshly produced material out of the actual hot burning zone or may bring more hydrogen fuel into the burning zone. In addition, the fuel balance may also change due to additional proton capture processes on short-lived radioactive nuclei in the CNO range [421]. Of particular relevance are the time scales for reaction sequences like $^{16}O(p,\gamma)^{17}F(p,\gamma)^{18}Ne(\beta,\nu)^{18}F(p,\alpha)^{15}O$ which would control fast additional fuel supply for the hot CNO cycle. Detailed sensitivity studies on explosive hydrogen burning in novae as a function of such nuclear uncertainties have been performed in a number of recent articles (José et al. 1999, Starrfield 1999, Starrfield et al. 2000, Coc et al. 2000, José et al. 2001).

Observations of over-abundances in the Ne to S mass range characterize Ne-novae which are interpreted to be thermonuclear runaways on accreting O-Ne white dwarfs with infusion of oxygen and neon (and magnesium) into the accreting envelope [238,124]. Proton capture reactions on the initial ^{20}Ne and ^{24}Mg lead to the production of heavier isotopes up to ^{32}S. This agrees well with recent observations in nova ejecta of silicon and sulfur [351]. According to theoretical model simulations considerable production of the long-lived radioisotopes ^{22}Na and ^{26}Al is expected [352,194] in Ne novae. However, recent observations of the gamma activity in novae with the COMPTEL observatory gave no indication for ^{22}Na or ^{26}Al activity. There is an order of magnitude discrepancy between predicted and observed intensities of the ^{22}Na gamma ray [303]. Studies of the nuclear reactions crucial to the synthesis of these radioisotopes are therefore particularly important. Recently a series of self-consistent calculations for nova nucleosynthesis have been performed for different sets of nuclear reaction rates [351,102]. The results clearly indicate significant impact of nuclear reaction rates on fast nova nucleosynthesis.

Current nova models predict significantly less mass of ejected material than is observed. Solutions to this problem suggest that peak temperatures in nova explosions may be much higher than (the currently accepted) 400 million degrees K. Such high temperatures imply that break-out of the hot CNO cycle can occur for some novae - agreeing with at least one recent nova observation. The nuclear physics information required to understand this higher-temperature burning includes measurements of nuclear reactions on proton-rich unstable isotopes. These reaction rates still carry considerable uncertainties since they are mostly estimated on the basis of nuclear structure and nuclear level analysis [173]. A recent study of the impact of nuclear reaction rates on nova nucleosynthesis indicated significant uncertainties for abundance predictions of all isotopes above mass A=20. The present reaction rates are reliable only for predictions of Li, Be, C, and N abundances. Many of the reaction rate uncertainties have to be reduced in order to predict more reliable O, F, Ne, Na, Mg, Al, Si, S, Cl, and Ar abundances [172].

8.2 X-Ray Bursts

At present X-ray bursts are explained as thermonuclear runaways in the hydrogen rich envelope of an accreting neutron star [360,231]. Figure 23 shows the observed light curve of a single X-ray burst which rapidly increases within

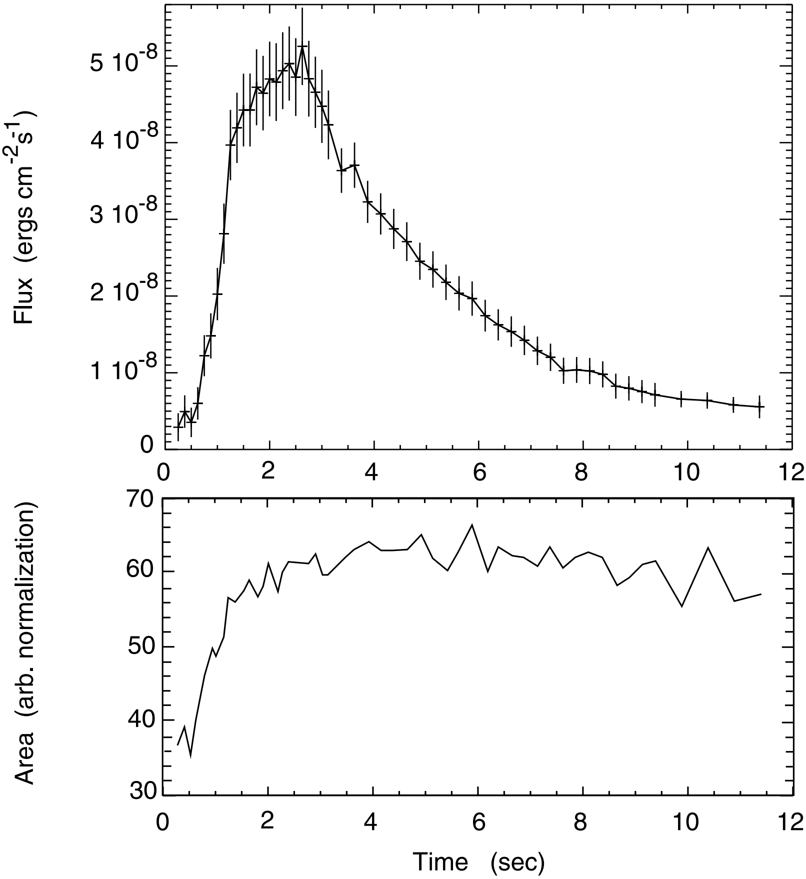

Fig. 23. A thermonuclear X-Ray Burst from the neutron star in the low mass x-ray binary system 4U 1728-34, as observed with the Rossi X-ray Timing Explorer. The top shows the rapid increase of the x-ray flux, followed by a slower decay. The lower panel indicates the change of the x-ray emitting area calculated for blackbody radiation from a specical system. The initial increase of the area provides strong evidence of the spread of the nuclear burning front over the entire surface of the neutron star. (courtesy: Tod Strohmayer)

seconds to maximum intensity. Low accretion rates favor a sudden local ignition of the material with a subsequent rapid spread over the neutron star surface [35]. This is also indicated in Fig. 23 which shows the spreading of the burning front over the entire neutron star surface.

Thermonuclear Runaway. The thermonuclear runaway is triggered by the ignition of the triple-alpha reaction and the break-out reactions from the hot CNO cycles [421]. Therefore the on-set of the X-ray burst critically depends on the rates of the alpha capture reactions on ^{15}O and ^{18}Ne. The rates for these break-out reactions carry still considerable uncertainties [251,127] and are subject to intense experimental studies using a wide variety of techniques with stable and radioactive beams [45,135,84]. The ^{15}O$(\alpha,\gamma)^{19}$Ne(p,γ)^{20}Na reaction sequence represents the main link by which the initial CNO isotopes will be converted towards heavier elements. With the onset of the ^{14}O(α,p)^{17}F reaction [72,142] a continuous flow of ^{4}He towards ^{21}Na via the sequence ^{4}He$(2\alpha,\gamma)^{12}$C(p,γ)^{13}N(p,γ)^{14}O (α,p)^{17}F(p,γ)^{18}Ne(α,p)^{21}Na by-passes the ^{15}O(α,γ) link and ^{18}Ne(α,p)^{21}Na emerges as the main break-out reaction controlling the flow towards heavier masses.

The uncertainty of the ^{15}O$(\alpha,\gamma)^{19}$Ne rate depends on the contribution of a single low energy resonance at 4.033 MeV excitation energy [227] which remains elusive to experimental scrutiny [138,218,85]. Most of the estimates are therefore still based on the α strength of the mirror state in ^{19}F which was determined from ^{15}N(^{6}Li,d)^{19}F transfer measurements [227,251]. The uncertainty in the ^{18}Ne(α,p)^{21}Na rate depends on the contributions of a fairly large number of low energy resonances which have not been studied directly yet [135,64,29]. In particular no clear spin and parity assignment has been made yet. This makes a reliable estimate of the reaction rate rather futile since only natural parity states will be contributing to the ^{18}Ne+α reaction channel.

The thermonuclear runaway itself is driven by the αp-process and the rapid proton-process (short rp-process) which convert the initial material rapidly to ^{56}Ni causing the formation of Ni oceans at the neutron star surface. The αp-process is characterized by a sequence of (α,p) and (p,γ) reactions processing the ashes of the hot CNO cycles ^{14}O and ^{18}Ne up to ^{34}Ar and ^{38}Ca range. Except for ^{14}O(α,p)^{17}F and ^{18}Ne(α,p)^{21}Na the reaction rates are all based on Hauser Feshbach predictions. The validity of the statistical approach in this mass range remains to be tested. This in particular since pronounced α-cluster structure in the T=1 even-even nuclei near the α threshold may lead to the occurrence of pronounced low energy resonances. Waiting points at positions where nuclear reaction flows are halted for beta-decay lifetimes, because (p,γ)- and α-induced reactions are either not competitive or over-balanced by a faster reverse reaction, have the potential to be observed in the detailed peak structure of X-ray lightcurves [104] as shown in Fig. 24.

The rp-Process. The rp-process represents a sequence of rapid proton captures up to the proton drip line and subsequent β-decays of drip line nuclei processing the material from the argon, calcium range up to ^{56}Ni and beyond (see Fig. 25). The flow is halted at ^{56}Ni during peak temperatures of around 2.0 to 3.0 billion degrees because of a $(p,\gamma)-(\gamma,p)$ chemical equilibrium due to a small reaction Q-value. In the subsequent cooling phase of the explosion photodisintegrations are suppressed and the rp-process continues beyond ^{56}Ni. The nucleosynthesis in the cooling phase of the burst alters con-

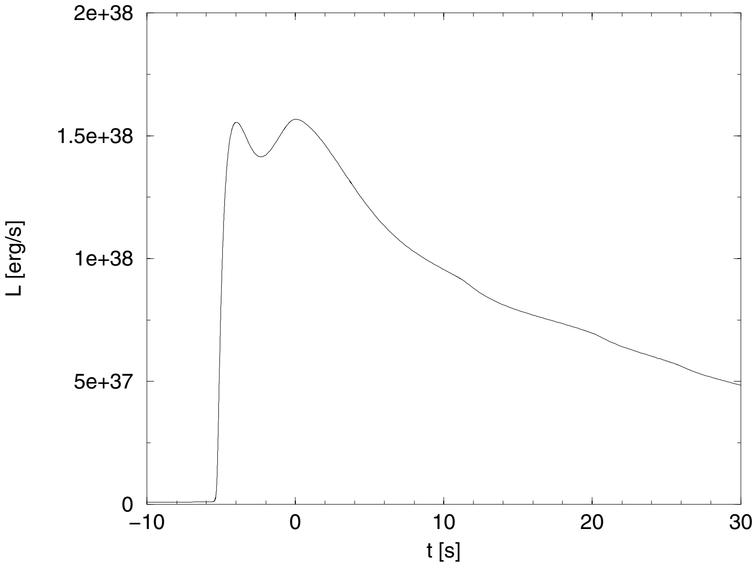

Fig. 24. Luminosity profile of an X-ray burst calculation with a full nuclear network, assuming a neutron star of $1.4M_\odot$ and a mass accretion rate of. The double peak structure (often seen in observations) is here due to the waiting point ^{30}S. Variations in neutron star size and accretion rate can change this structure, producing a regular single burst peak as well.

siderably the abundance distribution in atmosphere, ocean, and subsequently crust of the neutron star. This may have a significant impact on the thermal structure of the neutron star surface and on the evolution of oscillations in the oceans [47,33].

To verify the present models nuclear reaction and structure studies on the neutron deficient side of the line of stability are essential [336]. Measurements of the break-out reactions will set stringent limits on the ignition conditions for the thermonuclear runaway, measurements of alpha and proton capture on neutron deficient radioactive nuclei below ^{56}Ni will set limits on the time-scale for the actual runaway but will also affect other macroscopic observables. Recent simulations of the X-ray burst characteristics with self-consistent multi-zone models suggest indeed a significant impact of proton capture reaction rates between A=20 and A=64 on expansion velocity, temperature and luminosity of the burst [102,103,433]. The presently suggested reaction rates carry enormous uncertainties [336,400,174]. Recent shell model based calculations of proton capture rates in this mass range [153,101] did indeed indicate up to several orders of magnitude discrepancies to the global Hauser Feshbach predictions [336,312]. Clearly, more experimental data are necessary to remove the present uncertainties.

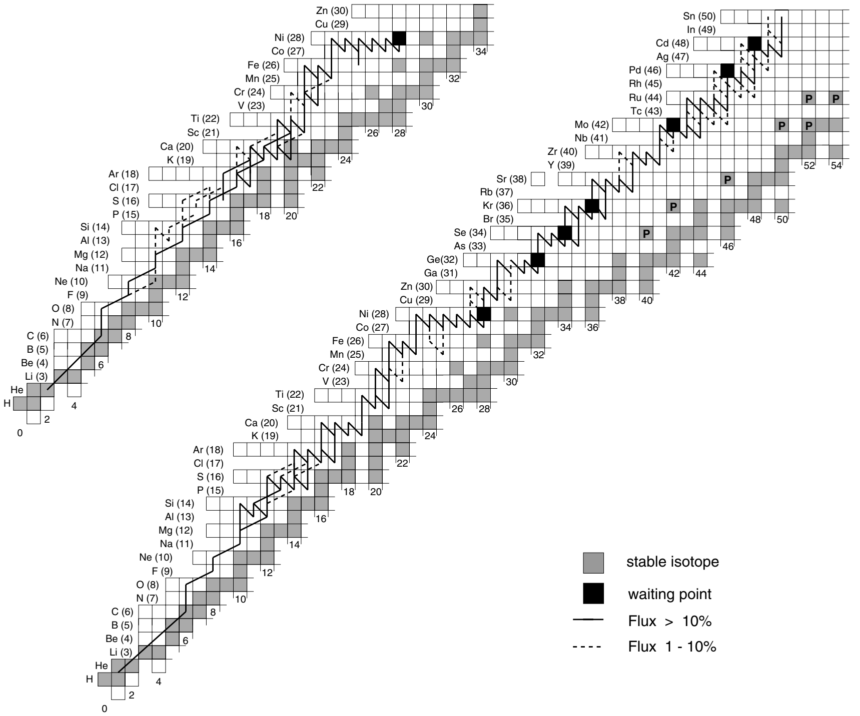

Fig. 25. Rp and αp-process flows up to and beyond Ni. The reaction flows shown in the nuclear chart are integrated reaction fluxes from a time dependent network calculation [422], (a) during the initial burst and thermal runaway phase of about 10s (top left), (b) after the onset of the cooling phase when the proton capture on ^{56}Ni is not blocked anymore by photodisintegrations (extending for about 200s, bottom right). Waiting points above ^{56}Ni are represented by filled squares, stable nuclei by hatched squares, light p-process nuclei below A=100 are indicated by a *P*.

Nuclear structure and nuclear reaction measurements near the double closed shell nucleus ^{56}Ni determine the conditions for the flow to heavier nuclei in the cooling phase. This depends on the actual rate of ^{56}Ni(p,γ) and the Q-value which determine the details of the chemical or (p,γ)-(γ,p) equilibrium. First measurements with ^{56}Ni beams have been performed [321] which lead to improved estimates of the reaction rate but considerable uncertainty still remains. Structure and reaction measurements beyond ^{56}Ni, in particular the experimental study of 2-proton capture reactions bridging the drip-line for even-even $N = Z$ nuclei like ^{64}Ge, ^{68}Se and ^{72}Kr are necessary to determine the final fate of the neutron star crust. The 2p-capture rates depend sensitively on the proton binding energies of the ^{65}As, ^{69}Br and ^{73}Rb nuclei, therefore reliable mass measurements are necessary for nuclei along the proton drip line in this mass range [46]. These mass measurements have to be complemented with decay studies. Of particular importance are beta-decay studies of isomeric and/or thermally populated excited states, which are not accessible for experiment with present equipment. In particular capture reactions on isomeric states may cause a significant change in reaction flow. There is a substantial need for nuclear structure information at the proton drip line, especially in the mass region along the drip line up to the A=100 range [198], to adress the multitude of open questions on the nucleosynthesis path and pattern in the rp-process towards its endpoint. An important question is the one for the endpoint of the rp-process. The endpoint is determined both by the macroscopic time-scale of the burst which depends on the various cooling mechanisms and the microscopic time-scale given by the effective life-times of the waiting point nuclei along the reaction path. For steady state burning scenarios, characterized by long-term high temperature conditions, the endpoint is basically determined by the availability of hydrogen fuel in the accreted layer. All of the predicted reaction and decay rates along the reaction path need to be experimentally tested and verified, yet, the present predictions suggest a reaction flow even beyond ^{100}Sn [336,422]. This raises the question for the actual endpoint. Alpha decay studies in the mass range above ^{100}Sn suggest that the neutron deficient isotopes ^{106}Te to ^{108}Te and ^{108}I predominantly decay into the α channel [295]. The isotope ^{109}I has been identified as a short-lived proton emitter [123]. These observations suggest that the actual endpoint of the rp-process might be associated with rapid back-processing of the material via proton or γ induced α decay in the Sn, Sb, Te range near the proton drip line. The most likely processes are ^{104}Sb$(p,\alpha)^{101}$Sn or ^{105}Te$(\gamma,\alpha)^{101}$Sn, ^{105}Sb$(p,\alpha)^{102}$Sn or ^{106}Te$(\gamma,\alpha)^{102}$Sn, and possibly also ^{106}Sb$(p,\alpha)^{103}$Sn. While some mass models [268,1] predict ^{104}Sb and ^{105}Sb to be proton unbound, the experimental decay-rates are longer than Hauser Feshbach predictions for the (p,α) reaction rates. Only a small amount of ^{106}Te, ^{107}Te is produced by ^{105}Sb(p,γ) and ^{106}Sb(p,γ), respectively and will be rapidly depleted by ^{106}Te$(p,\alpha)^{103}$Sb, and ^{107}Te$(p,\alpha)^{104}$Sb. Detailed reaction flow calculations for the rp-process have been performed to simulate the reaction flow in this mass range. It was clearly shown that multi-cycling emerges in the Sn-Te-I range. This cycle presents a strong impedance for the rp-process and has been identified as the actual end-point for the reaction path [337].

8.3 X-Ray Pulsars

X-ray pulsars are interpreted as accreting neutron stars with high accretion rates and large magnetic fields which funnel the accreted material to the pole cap, thus reaching locally high accretion rates [32]. This causes a steady burning of the accreted material via the αp- and the rp-processes on the surface of the neutron star [103]. Detailed studies of the nucleosynthesis suggest that the accreted material is rapidly converted to heavier elements in the mass 80 to 100 range which changes drastically the composition of the crust and the ocean of the neutron star replacing the original iron crust by a mixture of significantly more massive elements. Thus the composition of the neutron star crust in a binary system is substantially different from the one in a primordial single neutron star. This may have important effects on the thermal and electromagnetic conditions at the neutron star surface. The modified mass composition may also affect the observed decay of the magnetic field of the neutron star and its rotational r-modes due to shear effects. The final composition depends strongly on the nuclear physics associated with the rp-process and the endpoint of the rp-process, which is directly correlated with the accretion rate. For experimental confirmation in the lower mass range, studies similar to those for the X-ray burst simulations are required [338]. However, for accretion in excess of fifty times the Eddington limit the endpoint of the rp-process is expected to lie in the mass 150 range. This requires a new range of nuclear structure data near the limits of stability. Of particular interest are beta-decay lifetimes, and especially processes like direct proton and alpha decays. If these processes dominate, as is expected for the decay of very neutron deficient Tellurium, Iodine, and Xenon isotopes a natural halting point for the rp-process is reached [337].

8.4 Black Hole and Neutron Star Accretion Disks

Many of the accretion processes on neutron stars and black holes take place through accretion disks. Therefore it is necessary to investigate nuclear interaction processes that may occur during the accretion process at the local accretion disk in low density and high temperature conditions. Such processes may be of relevance for modeling X-ray bursts and X-ray pulsar events since such processes may alter the abundance distribution of the accreted material substantially [359]. At the fairly high temperature conditions of an accretion disk a considerable amount of the accreted hydrogen may actually be consumed before entering the neutron star atmosphere. This may affect our current understanding of the nucleosynthesis and energy release following ignition of the accreted material in thermonuclear runaways or steady burning modes. On the other side interaction of the high velocity accreted material with the outer atmospheres of the accreting object may cause spallation and fragmentation of the accreted material which in turn may greatly alter its composition and regenerate part of the pre-consumed hydrogen [34]. Clearly detailed nucleosynthesis studies in the accretion disk and during impact on the outer atmosphere of a neutron star are necessary to address these problems.

9 Outlook

While strong experimental radioactive beam programs in nuclear astrophysics are presently being pursued at all major research facilities, new initiatives to improve beam intensities for already available radioactive beams and to provide opportunities for beam developments closer or even at the drip lines dominate the discussions worldwide. ISAC at TRIUMF, REX ISOLDE at CERN and SPIRAL at GANIL are starting to operate as the most recently completed radioactive beam facilities, while new developments on a larger scale are planned for the future. The upgrade of the RIKEN accelerator facility to a radioactive beam factory RIBF is projected for completion and operation in 2007. The project features a superconducting ring cyclotron and a new projectile fragment separator system to provide high energy radioactive beams. In addition in-flight fission of uranium will be used to produce very neutron rich medium mass nuclei whose study will be important for the interpretation of the r-process. Activities in Europe presently focus on the proposed implementation of new technological developments at GSI in Germany which are centered around the construction of a fast cycling superconducting double-ring synchrotron with a system of storage rings for beam collection and beam cooling. Completion of this project is projected for 2012 and will lead to a unprecedented range of experimental opportunities with fast radioactive beams originating from fragment separation. Nuclear Astrophysics far off the limit of stability is being envisioned as one of the prime research area pursued at the new facility. The projected experiments will most likely focus on nuclear structure measurements - half-lives, masses, decay properties - along the rp-process and the r-process path and may extend to the measurement of p-process reactions using the Coulomb dissociation method. In addition to pure decay or ground state properties on the one hand and reaction cross section measurements on the other hand, there is the chance to investigate also other features like the density of excited states, giant (E1,M1) resonance properties as a function of distance from stability or the Gamow-Teller strength distribution for unstable nuclei. Such measurements can help to constrain the individual ingredients of theoretical predictions for strong, electromagnetic and weak interaction cross sections. Yet, in addition to reaction properties which were at the center of this review relevant to astrophysical issues of radioactive ion beams, the GSI facility will also provide unique opportunities for probing experimentally quark gluon plasma matter close to the conditions of neutron star matter. This aspect is also of significant interest for the nuclear astrophysics community since it may provide novel experimental opportunities to test not only quark-gluon plasma matter at conditions similar to those in the center of a neutron star but also the transition to normal nuclear matter as anticipated for the lower layers of the neutron star crust. This has an impact for a number of environments discussed in this review, type II supernovae, neutron star mergers as well as X-ray bursts. The most ambitious future project yet is RIA, the Rare Isotope Accelerator, a US project which is presently awaiting approval by the US Department of Energy. RIA is centered around a 1.4 GeV multi-beam LINAC driver accelerator capable of providing beams from protons to uranium at energies of at least 400 MeV per nucleon, with beam power in excess of 100 kW. With this flexibility, the production reaction can be chosen to optimize the yield of a desired isotope. In comparison to the two main competing in-flight facilities, the Radioactive Ion Beam Factory at RIKEN and the next-generation GSI facility, RIA has two advantages. RIA seeks to combine both technological methods of producing radioactive beams by providing low energy ISOL separated beams and fast energy fragment separated radioactive beams. RIA's capability for post acceleration of ISOL based radioactive particles is not included in either of the other two projects. This dual-concept approach allows to develop maximum intensity beams over the entire nuclear chart using the most advantageous production mode, will allow a wider range of experimental studies. These will expand to the direct measurement of nuclear reactions at astrophysical energies beyond the measurements of nuclear structure characteristics relevance for astrophysics which is the main focus for experiments with fragment separated high energy beams.

References

1. Y. Aboussir, J.M. Pearson, A.K. Dutta, F. Tondeur: Nucl.Phys. A **549**, 155 (1992)
2. Y. Aboussir et al.: At. Data Nucl. Data Tables **61**, 127 (1995)
3. A. Alastuey, B. Jancovici: Astrophys. J. **226**, 1034 (1978)
4. A. Alexakis, A.C. Calder, A. Heger, E.F. Brown, L.J. Dursi, J.W. Truran, R. Rosner, D.Q. Lamb, F.X. Timmes, B. Fryxell, M. Zingale, P.M. Ricker, K. Olson: eprint arXiv:astro-ph/0307126 (2003) and Astrophys. J. **602**, 931 (2004)
5. C. Angulo et al.: Nucl.Phys. A **656**, 3 (1999)
6. D. Argast, et al.: Astr. and Astrophys. **388**, 842 (2002)
7. D. Argast, et al.: Astr. and Astrophys., in press (2004)
8. C. Arlandini et al.: Astrophys. J. **525**, 886 (1999)
9. Arnett, W.D.: Ann. Rev. Astron. Astrophys. **33**, 115 (1995)
10. Arnett, W.D.: *Nucleosynthesis and Supernovae*, (Princeton Univ. Press 1996)
11. W.D. Arnett, F.-K. Thielemann: Astrophys. J. **295**, 589 (1985)
12. M. Arnould: Astr. and Astrophys. **19**, 92 (1972)
13. M. Arnould, S. Goriely: Phys. Rep. **384**, 1 (2003)
14. M. Avrigeanu, W. von Oertzen, AJM. Plompen, V. Avrigeanu: Nucl. Phys. **A723**, 104 (2003)
15. R. Azuma et al.: Phys. Rev. C **50**, 1194 (1994)
16. C. Bäumer et al.: Phys. Rev. C **68**, 031303 (2003)
17. G. Audi et al.: Nucl. Phys. A **624**, 1 (1997)
18. G. Audi, AH. Wapstra, C. Thibault: Nucl. Phys. A **729**, 337 (2003); AH. Wapstra, G. Audi: Nucl. Phys. A **729**, 129 (2003)
19. M.B. Aufderheide, I. Fushiki, S.E. Woosley, D.H. Hartmann: Astrophys. J. Supplement **91**, 389 (1994)
20. Z. Y. Bao, F. Käppeler: At. Data Nucl. Data Tables **36**, 411 (1987)
21. Z. Y. Bao, H. Beer, F. Käppeler et al.: At. Data Nucl. Data Tables **76**, 70 (2000)

22. D.W. Bardayan et al.: Phys. Rev. Lett. **83**, 45 (1999)
23. D.W. Bardayan et al.: Phys. Rev. C **63**, 065802 (2001)
24. F.C. Barker, T. Kajino: Aust. J. Phys. **44**, 369 (1991)
25. E. Bauge, JP. Delaroche, M.Girod: Phys. Rev. C **63**, 4607 (2001)
26. M. Beard, M. Wiescher: Rev. Mex. Fis. Suppl. **49**, 139 (2003),
27. H. Beer, F. Voss, R.R. Winters: Astrophys. J. Suppl. **80**, 403 (1992)
28. M. Bender et al.: Eur. Phys. J. **A8**, 59 (2000)
29. G.P.A. Berg, K. Hatanaka, M. Wiescher, H. Schatz, T. Adachi, A.D. Bacher, C.C. Foster, Y. Fujita, H. Fujita, K. Fujita, J. Görres, Ch. Herman, J. Kamiya, N. sakamoto, Y. Sakemi, Y. Shimbara, Y. Shimizu, E.J. Stephenson, T. Wakasa, M. Yosoi: Nucl.Phys. A **718**, 608c (2003)
30. H.A. Bethe, G.E. Brown, J. Applegate, J.M. Lattimer: Nucl. Phys. A **324**, 487 (1979)
31. H.A. Bethe: Rev. Mod. Phys. **62**, 801 (1990)
32. L. Bildsten, E.F. Brown: Astrophys.J. **477**, 897 (1997)
33. L. Bildsten: Astrophys.J. **501**, L89 (1998)
34. L. Bildsten, E.E. Salpeter, I. Wassermann: Astrophys.J. **384**, 143 (1992)
35. L. Bildsten, T. Strohmayer: Physics Today **52**, 40 (1999)
36. S. Bishop et al.: Phys. Rev. Lett. **90**, 162501 (2003)
37. J.M. Blatt, V.F. Weisskopf: *Theoretical Nuclear Physics* (Wiley, New York 1952)
38. K.H. Bockhoff, A.D. Carlson, O.A. Wasson, J.A. Harvey, D.C. Larson: Nucl. Sci. Eng. **106**, 192 (1990)
39. G. Bollen et al.: Phys. Rev. C **46**, R2140 (1992)
40. I.N. Borzov: Z. Phys. A **335**, 125 (1996); Nucl. Phys. A **621**, 307c (1997)
41. I.N. Borzov: Phys. Rev. C **67**, 025802 (2003)
42. I.N. Borzov, S. Goriely: Phys. Rev. C **62**, 5501 (2000)
43. V. Bouquelle, N. Cerf, M. Arnould, M. Tachibana, S. Goriely: Astron. and Astrophys. **305**, 1005 (1996)
44. F. Brachwitz, D.J. Dean, W.R. Hix, K. Iwamoto, K. Langanke, G. Martínez-Pinedo, K. Nomoto, M.R. Strayer, F.-K. Thielemann, H. Umeda: Astrophy. J. **536**, 934 (2000)
45. W. Bradfield-Smith et al., Phys. Rev. C **59**, 3402 (1999)
46. B.A. Brown, R.R.C. Clement, H. Schatz, A. Volya: Phys. Rev. C **65**, 04802 (2002)
47. E. Brown: Astrophys. J. **531**, 988 (2000)
48. L.S. Brown, R.F. Sawyer: Rev. Mod. Phys. **69**, 411 (1997)
49. S.W. Bruenn: Astrophys. J. Suppl. **58**, 771 (1985); A. Mezzacappa, S.W. Bruenn: Astrophys. J. **405**, 637 (1993); **410**, 740 (1993)
50. S.W. Bruenn, W.C. Haxton: Astr. J. **376**, 678 (1991)
51. L. Buchmann et al.: Phys. Rev. Lett. **70**, 726 (1993)
52. L. Buchmann: Astrophys. J. **468**, L127 (1996); Ap. J. **479**, L153 (1997)
53. L. Buchmann, R.E. Azuma, C.A. Barnes, J. Humblet, K. Langanke: Phys. Rev. C **54**, 393 (1996); Nucl. Phys. A **621**, 153 (1997)
54. R. Buras, M. Rampp, H.-T. Janka, K. Kifionidis: Phys. Rev. Lett. **90**, 241101 (2003)
55. E.M. Burbidge et al.: Rev. Mod. Phys. **29**, 547 (1957)
56. A. Burrows: Astrophys. J. **334**, 891 (1988)
57. A. Burrows: Ann. Rev. Nucl. Sci. **40**, 181 (1990)

58. A. Burrows, B.A. Fryxell: Science **258**, 430 (1992)
59. A. Burrows, R.F. Sawyer: Phys.Rev. C **58** 554 (1998)
60. A. Burrows, R.F. Sawyer: Phys. Rev. C **59**, 510 (1999)
61. A. Burrows, T. Young, P. Pinto, R. Eastman, T.A. Thompson: Astrophys. J. **539**, 865 (2000)
62. M. Busso et al.: Astrophys. J. **557**, 802 (2001)
63. J.A. Caggiano et al.: Phys. Rev. C **64**, 025802 (2001)
64. J.A. Caggiano, W. Bradfield-Smith, J.P. Greene, R. Lewis, P.D. Parker, K.E. Rehm, D.W. Visser: Phys. Rev. C **66**, 015804 (2002)
65. G.R. Caughlan, W.A. Fowler: At. Data Nucl. Data Tables **40**, 283 (1988)
66. G.R. Caughlan, W.A. Fowler, M.J. Harris, G.E. Zimmerman: At. Data Nucl. Data Tables **32**, 197 (1985)
67. A.G.W. Cameron: Atomic Energy of Canada, Ltd., CRL-**41** (1957)
68. A.G.W. Cameron: Nucl. Phys. A **688**, 289 (2001)
69. A.G.W. Cameron, R.M. Elkin: Can. J. Phys. **43**, 1288 (1965)
70. E. Caurier, K. Langanke, G. Martínez-Pinedo, F. Nowacki: Nucl. Phys. A **653**, 439 (1999)
71. G. Chabrier, E. Schatzman: *The Equation of State in Astrophysics*, IAU Coll. **147**, (Cambridge Univ. Press 1994)
72. A.E. Champagne, M. Wiescher: Ann. Rev. Nucl. Part. Sci. **42**, 39 (1992)
73. B. Chen et al.: Phys. Lett. B **355**, 37 (1995)
74. A. Chieffi, M. Limongi: Astrophys. J. **577**, 281 (2002)
75. J.A. Cizewski et al.: "Single-Particle Structure of Neutron-Rich Nuclei", In: *Proceedings of the International Conference on the Labyrinth in Nuclear Structure*, (AIP in press)
76. D.D. Clayton: *Principles of Stellar Evolution and Nucleosynthesis*, (Univ. of Chicago Press 1968, 1983)
77. J. Cooperstein, J. Wambach: Nucl. Phys. A **420**, 591 (1984)
78. M. Couder et al.: Nucl. Inst. Meth. A **506**, 26 (2003)
79. J.J. Cowan, A.G.W. Cameron, J.W. Truran: Astrophys. J., **265**, 429 (1983)
80. J.J. Cowan et al.: Phys. Rep. **208**, 267 (1991)
81. J.J. Cowan et al.: Astrophys. J. **521**, 194 (1999)
82. M. Danos: Nucl. Phys. 5, 23 (1958)
83. B. Davids, S.M. Austin, D. Bazin, H. Esbensen, B.M. Sherrill, I.J. Thompson, J.A. Tostevin: Phys. Rev. C **63**, 065806 (2001)
84. B. Davids, A.M. van den Berg, P. Dendooven, F. Fleurot, M. Hunyadi, M.A. de Huu, K.E. Rehm, R.E. Segel, R.H. Siemssen, H. Wilschut, H.J. Wörtche, A H. Wuosmaa: Phys. Rev. C **67**, 012801 (2003)
85. B. Davids, A.M. van den Berg, P. Dendooven, F. Fleurot, M. Hunyadi, M.A. de Huu, R H. Siemssen, H W. Wilschut, H.J. Wörtche, M. Hernanz, J. José, K.E. Rehm, A.H. Wuosmaa, R.E. Segel: Phys. Rev. C **67**, 065808 (2003)
86. T. Davinson et al.: Nucl. Instr. Meth. A **454**, 350 (2000)
87. D.J. Dean, S.E. Koonin, K. Langanke, P.B. Radha, Y. Alhassid: Phys. Rev. Lett. **74**, 2909 (1995)
88. T. Delbar et al.: Phys. Rev. C **48**, 3088 (1993)
89. P. Demetriou, S. Goriely: Nucl. Phys. A **695**, 95 (2003)
90. P. Demetriou, C. Grama, S. Goriely: Nucl. Phys. A **718**, 510c (2003)
91. I. Dillmann et al.: Phys. Rev. Lett. **91**, 162503 (2003)
92. J. Dobaczewski: Acta Phys. Pol. B **30**, 1647 (1999)

93. D. Eichler et al.: Nature **340**, 126 (1989)
94. J. Engel et al.: Phys. Rev. C **60**, 4302 (1999)
95. R.I. Epstein, S.A. Colgate, W.C. Haxton: Phys. Rev. Lett. **61**, 2038 (1988)
96. S.N. Ezhov, V. A. Plujko: Z. Phys. **346**, 275 (1993)
97. S. Fantoni, B.L. Friman, V.R. Pandharipande: Phys. Rev. Lett. **48**, 1089 (1981)
98. M. Fey et al.: Nucl. Phys. A **718**, 131
99. B.W. Filippone: Ann. Rev. Nucl. Part. Sci. **36**, 717 (1987)
100. B.W. Filippone, J. Humblet, K. Langanke: Phys. Rev. C **40**, 515 (1989)
101. J. Fisker, V. Barnard, J. Görres, K. Langanke, G. Martínez-Pinedo, M. Wiescher: At. Data Nucl. Data Tab. **79**, 241 (2001)
102. J. Fisker, F. Rembges, V. Barnard, M. Wiescher: In: *The influence of binaries on stellar population studies*, (Kluwer Academic, Astrophysics and space science library (ASSL), Brussels), **264**, 582 (2002)
103. J.L. Fisker, W.R. Hix, M. Liebendörfer et al.: Nucl. Phys. A **718**, 614 (2003)
104. J.L. Fisker, F.-K. Thielemann: Astrophys. J., submitted (2004)
105. W.A. Fowler, G. E. Caughlan, B. A. Zimmermann: Ann. Rev. Astron. Astrophys. **5**, 525 (1967)
106. W.A. Fowler, G.E. Caughlan, B.A. Zimmerman: Ann. Rev. Astron. Astrophys. **13**, 69 (1975)
107. W. Frank, A. Seeger: Appl. Phys. A **3**, 66 (1988)
108. C. Freiburghaus et al.: Astrophys. J. **516**, 381 (1999)
109. C. Freiburghaus et al.: Astrophys. J. **525**, L121 (1999)
110. C.L. Fryer, M.S. Warren: Astrophys. J. **574**, L65 (2002)
111. B. Fryxell, M. Zingale, F.X. Timmes, D.Q. Lamb, K. Olson, A.C. Calder, L.J. Dursi, P. Ricker, R. Rosner, J.W. Truran, P. MacNeice, H. Tufo: Nucl. Phys. A **688**, 172c (2001)
112. G. M. Fuller: Astrophys. J. **252**, 741 (1982)
113. G.M. Fuller, W.A. Fowler, M.J. Newman: Astrophys. J. Suppl. **42**, 447 (1980)
114. G.M. Fuller, W.A. Fowler, M.J. Newman: Astrophys. J. Suppl. **48**, 279 (1982)
115. G.M. Fuller, W.A. Fowler, M.J. Newman: Astrophys. J. **252**, 715 (1982)
116. G.M. Fuller, W.A. Fowler, M.J. Newman: Astrophys. J. **293**, 1 (1985)
117. G. Fuller, B.S. Meyer: Astrophys. J. **453**, 792 (1995), **464**, 521 (1996)
118. I. Fushiki, D.Q. Lamb: Astrophys. J. **317**, 368 (1987)
119. E. Gadioli, P.E. Hodgson: *Pre-Equilibrium Nuclear Reactions*, (Clarendon Press, Oxford 1992)
120. R. Gallino et al.: Astrophys. J. **497**, 388 (1998)
121. R.D. Gehrz, J.W. Truran, R.E. Williams, S. Starrfield: Publ. Astronom. Soc. Pacific **110**, 3 (1998)
122. A. Gilbert, A.G.W. Cameron: Can. J. Phys. **43**, 1446 (1965)
123. A. Gillitzer, T. Faestermann, K. Hartel, P. Kienle, E. Nolte: Z. Phys. A **326**, 107 (1987)
124. P. Gil-Pons, E. Garcia-Berro, J. Jose, M. Hernanz, J.W. Truran: eprint arXiv:astro-ph/0306197 (2003) and Astr. and Astrophys., to be published
125. S.A. Glasner, E. Livne, J.W. Truran: Astrophys. J. **475**, 754 (1997)
126. P. Goldreich, S.V. Weber: Astrophys. J. **238**, 991 (1980)
127. J. Görres, M. Wiescher, F.-K. Thielemann: Phys. Rev. C **51**, 392 (1995)
128. J. Görres et al.: Phys. Rev. Lett. **80**, 2554
129. S. Goriely, E. Khan: Nucl. Phys. A **706**, 217 (2002)

130. S. Goriely et al.: Phys. Rev. C **66**, 4326 (2002)
131. S. Goriely, J. José, M. Hernanz, M. Rayet, M. Arnould: Astrophys. and Astron. **383**, 27 (2002)
132. S. Goriely, M. Samyn, M. Bender, J.M. Pearson: Phys. Rev. C **68**, 054325 (2003)
133. J.-S. Graulich et al.: Phys. Rev. C **63**, 011302 (2001)
134. W. Greiner, D.N. Poenaru: 'Cluster Preformation in Closed- and Mid-shell Nuclei'. In: *Atomic and Nuclear Clusters, 2nd International Conference at Santorini, Greece, June 28–July 2, 1993*, ed. by G.S. Anagnostatos, W. von Oertzen (Springer, Heidelberg 1994) pp. 264–266
135. D. Groombridge et al.: Phys. Rev. C **66**, 055802 (2002)
136. A.V. Gruzinov, J.N. Bahcall: Astrophys. J. **504**, 996 (1998)
137. X. Gu et al.: Phys. Lett. B **343**, 31 (1995)
138. G. Hackman, S.M. Austin, T. Glasmacher, T. Aumann, B.A. Brown, R.W. Ibbotson, K. Miller, B. Pritychenko, L.A. Riley, B. Roeder, E. Spears: Phys. Rev. C **61**, 052801(R) (2000)
139. P. Haensel, J.L. Zdunik: Astron. Astrophys. **404**, L3 (2003)
140. M. Hannawald et al.: Phys. Rev. C **62**, 054301 (2000)
141. J.P. Hansen, G.M. Torrie, P. Veillefosse: Phys. Rev. A **16**, 2153 (1977)
142. B. Harss, C.L. Jiang, K.E. Rehm, J P. Schiffer, J. Caggiano, P. Collon, J.P. Greene, D. Henderson, A. Heinz, R.V.F. Janssens, J. Nolen, R.C. Pardo, T. Pennington, R.H. Siemssen, A.A. Sonzogni, J. Uusitalo, and I. Wiedenhöver, M. Paul, T.F. Wang, F. Borasi, R.E. Segel, J.C. Blackmon, M. Smith, A. Chen, P. Parker: Phys. Rev. C **65**, 035803 (2002)
143. W. Hauser, H. Feshbach: Phys. Rev. A **87**, 366 (1952)
144. P. Hauser, W.R. Hix, M. Liebendörfer, G. Martínez-Pinedo, A. Mezzacappa, F.-K. Thielemann: Astrophys. J., to be submitted (2004)
145. W.C. Haxton: Phys. Rev. Lett. **60**, 1999 (1988)
146. A. Heger, K. Langanke, G. Martínez-Pinedo, S.E. Woosley: Phys. Rev. Lett. **86**, 1678 (2001)
147. A. Heger, S.E. Woosley, G. Martinez-Pinedo, K. Langanke: Astrophys. J. **560**, 307 (2001)
148. A. Heger, SE. Woosley, T. Rauscher et al.: New Astron. Rev. **46**, 463 (2002)
149. A. Hektor et al.: Phys. Rev. C **61**, 5803 (2000)
150. R.L. Helmer et al.: Phys. Rev. C **55**, 2802 (1997)
151. M. Henchek et al.: Phys. Rev. **50**, 2219 (1994)
152. F. Herfurth et al.: Phys. Rev. Lett. **87**, 142501 (2001)
153. H. Herndl, J. Görres, M. Wiescher, B.A. Brown, L. van Wormer: Phys. Rev. C **52**, 1078 (1995)
154. W. Hillebrandt: New Astronomy Rev. **48**, 615 (2004)
155. M. Hirsch, A. Staudt, K. Muto, H.V. Klapdor-Kleingrothaus: Nucl. Phys. A **535**, 62 (1992)
156. W.R. Hix: Ph.D. thesis, (Harvard University, 1995)
157. W.R. Hix, F.-K. Thielemann: Astrophys. J. **460**, 869 (1996)
158. W.R. Hix, F.-K. Thielemann: Astrophys. J. **511**, 862 (1999)
159. W.R. Hix, F.-K. Thielemann; J. Comp. Appl. Math. (JCAM) **109**, 321 (1999)
160. W.R. Hix et al.: Phys. Rev. Lett. **91**, 201102 (2003)
161. P. Höflich, A. Khokhlov: Astrophys. J. **457**, 500 (1996)
162. P. Höflich, J.C. Wheeler, F.-K. Thielemann: Astrophys. J. **495**, 617 (1998)

163. R.D. Hoffman, S.E. Woosley, S.E. Fuller, B.S. Meyer: Astrophys. J. **460**, 478 (1996)
164. R.D. Hoffman et al.: Astrophys. J. **482**, 951 (1997)
165. R.D. Hoffman, S. E. Woosley, T.A. Weaver, T. Rauscher, F.-K. Thielemann: Astrophys. J. **521**, 735 (1999)
166. J.A. Holmes, S.E. Woosley, W.A. Fowler, B.A. Zimmerman: At. Data Nucl. Data Tables **18**, 306 (1976)
167. C.J. Horowitz: Phys. Rev. D **65**, 3001 (2002)
168. W.M. Howard, B.S. Meyer, D.D. Clayton: Meteoritics **27**, 404 (1992)
169. W.M. Howard, B.S.Meyer, S.E. Woosley: Astrophys. J. Lett. **373**, L5 (1991)
170. W.M. Howard, P. Möller: At. Data Nucl. Data Tables **25**, 219 (1980)
171. J. Hubbard: Phys. Lett. **3**, 77; R.D. Stratonovich: Sov. Phys. Dokl. **2**, 416 (1958)
172. C. Iliadis, A. Champagne, J. José, S. Starrfield, P. Tupper: Astrophys. J. Suppl. **142**, 105 (2002)
173. C. Iliadis, J.M. D'Auria, S. Starrfield, W.J. Thompson, M. Wiescher: Astrophys. J. Suppl. **134**, 151 (2001)
174. C. Iliadis, P.M. Endt, N. Prantzos, W.J. Thompson: Astrophys. J. **524**, 434 (1999)
175. S. Ichimaru, S. Tanaka, H. Iyetomi: Phys. Rev. A **29**, 2033 (1984)
176. S. Ichimaru: Rev. Mod. Phys. **65**, 255 (1993)
177. S. Ichimaru: 1996, Publ. Astr. Soc. Japan **48**, 613 (1996)
178. S. Ichimaru, K. Utsumi: Astrophys. J. **269**, L51 (1983)
179. S. Ichimaru, K. Utsumi: Astrophys. J. **286**, 363 (1984)
180. S. Ichimaru, S. Ogata, K. Tsuruta: Phys. Rev. E **50**, 2977 (1994)
181. A.V. Ignatyuk, K.K. Istekov, G.N. Smirenkin: Sov. J. Nucl. Phys. **29**, 450 (1979)
182. A.S. Iljinov et al.: Nucl. Phys. A **543**, 517 (1992)
183. Y. Ishimaru et. al.: IAU SYMP **187**, 117; MPA/P13, 224 (2002)
184. N. Itoh, H. Totsuji, S. Ichimaru: Astrophys. J. **218**, 477; Astrophys. J. **220**, 742 (1977)
185. N. Itoh, H. Totsuji, S. Ichimaru, H.E. DeWitt: Astrophys. J. **234**, 1079; Astrophys. J. **239**, 415 (1979)
186. N. Itoh, F. Kuwashima, H. Munakata: Astrophys. J. **362**, 620 (1990)
187. K. Iwamoto et al.: Astrophys. J. Suppl. **125**, 439 (1999)
188. A.N. James et al.: Nucl. Inst. Meth. A **267**, 144 (1988)
189. H.T. Janka, M. Rampp: Astrophys. J. **539**, L33 (2000)
190. H.-T. Janka et al: to be published
191. H.T. Janka, M. Ruffert: Astron. and Astrophys. **307**, L33 (1996)
192. J.P. Jeukenne, A. Lejeune, C. Mahaux: Phys. Rev. C **16**, 80 (1977)
193. C.W. Johnson, S.E. Koonin, G.H. Lang, W.E. Ormand: Phys. Rev. Lett. **69**, 3157 (1992)
194. J. José, A. Coc, M. Hernanz: Astrophys. J. **520**, 347 (1999)
195. J. José A. Coc, M. Hernanz: Astrophys. J. **560**, 897 (2001)
196. F. Käppeler et al.: Rep. Prog. Phys. **52**, 945 (1989)
197. F. Käppeler et al.: Astrophys. J. 437, 396 (1994)
198. F. Käppeler, F.-K. Thielemann, M. Wiescher: Ann. Rev. Nucl. Part. Sci. **48**, 175 (1998)
199. F. Käppeler: Prog. Part. Nucl. Phys. **43**, 419 (1999)

200. V. Kalogera et al.: Astrophys. J. **556**, 340 (2001)
201. W. Keil, H.-T. Janka: Astron. and Astrophys. **296**, 145 (1995)
202. A. Kercek, W. Hillebrandt, J.W. Truran: Astron. and Astrophys. **345**, 831(1999)
203. J. Kiener et al.: Nucl. Phys. A **552**, 66 (1993)
204. K. Kifionidis, T. Plewa, H-T. Janka, E. Müller: Astron. and Astrophys. **408**, 621 (2003)
205. H. Kitamura, S. Ichimaru: Astrophys. J. **438**, 300 (1995)
206. H.V. Klapdor, J. Metzinger, T. Oda: At. Data Nucl. Data Tables **31**, 81 (1984)
207. J.J. Kolata et al.: Phys. Rev. C **63**, 024616 (2001)
208. E. Kolbe, S. Krewald, K. Langanke, F.-K. Thielemann: Nucl. Phys. A **540**, 599 (1992)
209. E. Kolbe et al.: Phys. Rep. **227**, 37 (1993)
210. E. Kolbe, K. Langanke, F.-K. Thielemann, P. Vogel: Phys. Rev. C **52**, 3437 (1995)
211. E. Kolbe et al.: Eur. J. Phys. A **3**, 389 (1998)
212. E. Kolbe, K. Langanke, G. Martínez-Pinedo, P. Vogel: J. Phys. G **29**, 2569 (2003)
213. S.E. Koonin, D.J. Dean, K. Langanke: Phys. Rep. **278**, 1 (1997)
214. K.-L. Kratz, F.-K. Thielemann, W. Hillebrandt, P. Möller, V. Harms, J.W. Truran: J. Phys. G **14**, 331 (1988)
215. K.-L. Kratz et al.: Z. Phys. A **325**, 489 (1986)
216. K.-L. Kratz et al.: Astrophys. J. **403**, 216 (1993)
217. K.-L. Kratz, B. Pfeiffer, F.-K. Thielemann, W.B. Walters: Hyperfine Interactions **129**, 185 (2000)
218. A.M. Laird, S. Cherubini, A.N. Ostrowski, M. Aliotta, T. Davinson, A. Di Pietro, P. Figuera, W. Galster, J.S. Graulich, D. Groombridge, J. Hinnefeld, M. Lattuada, P. Leleux, L. Michel, A. Musumarra, A. Ninane, M.G. Pellegriti, A C. Shotter, C. Spitaleri, A. Tumino, J. Vervier, P. Woods: Phys. Rev. C **66** (2002) 048801
219. K. Langanke, C.A. Barnes: Adv. Nucl. Phys. **22**, 173 (1996)
220. K. Langanke, E. Kolbe: At. Data Nucl. Data Tables **79**, 293 (2001)
221. K. Langanke, E. Kolbe: At. Data Nuclear Data Tables **82**, 191 (2002)
222. K. Langanke, E. Kolbe, D.J. Dean: Phys. Rev. C **63**, 032801 (2001)
223. K. Langanke, G. Martínez-Pinedo: Nucl. Phys. A **673**, 481 (2000)
224. K. Langanke, G. Martínez-Pinedo: At. Data Nucl. Data Tables **79**, 1 (2001)
225. K. Langanke, G. Martinez-Pinedo: Rev. Mod. Phys. **75**, 819 (2003)
226. K. Langanke et al.: Phys. Rev. Lett. **90**, 241102 (2003)
227. K. Langanke, M. Wiescher, W.A. Fowler, J. Görres: Astrophys. J. **301**, 629 (1986)
228. N. Langer, C. Henkel: In: *Nuclei in the Cosmos III*, eds. M. Busso, R. Gallino, C.M. Raiteri, (AIP Press, 1995) p. 413
229. J.M. Lattimer et al.: Astrophys. J. **213**, 225 (1977)
230. M.-Y. Lee et al.: Nucl. Instr. Meth. A **422**, 536 (1999)
231. W.H.G. Lewin, J. van Paradijs, R.E. Taam: Space Sci. Rev. **62**, 233 (1993)
232. M. Liebendörfer, A. Mezzacappa, F.-K. Thielemann: Phys. Rev. D **63**, 4003 (2001)
233. M. Liebendörfer et al.: MPA/P **13**,126 (2002).
234. M. Liebendörfer, S. Rosswog, F.-K. Thielemann: Astrophys. J. Suppl. **S 141**, 229 (2002)

235. M. Liebendörfer, A. Mezzacappa, O.E.B. Messer et al.: Nucl. Phys. A **719**, 144 (2003)
236. M. Liebendörfer, O.E.B. Messer, A. Mezzacappa, S.W. Bruenn, C.Y. Cardall, F.-K. Thielemann: Astrophys. J. Suppl. **S 150**, 263 (2004)
237. M. Limongi, A. Chieffi: Astrophys. J. **592**, 404 (2003)
238. M. Livio, J.W. Truran: Astrophys. J. **425**, 797 (1994)
239. E. Livne, W.D. Arnett: Astrophys. J. **452**, 62 (1995)
240. E. Livne, A. Burrows, R. Walder, I. Lichtenstadt, T.A. Thompson: Astrophys. J., in press (2004)
241. M.J. Lopez-Jiminez et al.: Phys. Rev. C **66**, 025803 (2002)
242. D.R. Lorimer: Living Reviews in Relativity, in press (2002)
243. L. McFadden, G.R. Satchler: Nucl. Phys. **84**, 177 (1966)
244. C. Mahaux: Phys. Rev. C **82**, 1848 (1982)
245. C. Mahaux, H.A. Weidenmüller: Ann. Rev. Part. Nucl. Sci. **29**, 1 (1979)
246. R.A. Malaney, W.A. Fowler: Astrophys. J. **333**, 14 (1988)
247. R.A. Malaney, W.A. Fowler: Astrophys. J. **345**, L5 (1989)
248. A. Mamdouh et al.: Nucl. Phys. A **679**, 337 (2001)
249. F.M. Mann: Hanford Engineering HEDL-TME **78-83** (1978)
250. P. Mantica et al.: Phys. Rev. C **67**, 014311 (2003)
251. Z.Q. Mao, H.T. Fortune, A.G. Lacaze: Phys. Rev. C **53**, 1197 (1996)
252. G. Martinez-Pinedo, K. Langanke: Phys. Rev. Lett. **83**, 4502 (1999)
253. G. McLaughlin, G.M. Fuller: Astrophys. J. **464**, L143 (1996)
254. G.C. McLaughlin et al.: Phys. Rev. C **59**, 2873 (1999)
255. A. Mengoni, Y. Nakajima: J. Nucl. Sci. Techn. **31**, 151 (1994)
256. B.S. Meyer: Astrophys. J. **343**, 254 (1989)
257. B.S. Meyer et al.: Phys. Rev. C **39**, 1876 (1989)
258. B.S. Meyer et al.: Astrophys. J. **399**, 656 (1992)
259. B.S Meyer: Astrophys. J. **449**, L55 (1995)
260. B.S. Meyer et al.: Phys. Rev. C **58**, 3696 (1998)
261. A. Mezzacappa: Nucl. Phys. A **688**, 158c (2001)
262. A. Mezzacappa, A.C. Calder, S.W. Bruenn, J.M. Blondin, M.W. Guidry, M.R. Strayer, A.S. Umar: Astrophys. J. **495**, 911 (1998)
263. A. Mezzacappa et al.: Phys. Rev. Lett. **86**, 1935 (2001)
264. G. Michaud, W.A. Fowler: Phys. Rev. C **2**, 2041 (1970)
265. G. Michaud, W.A. Fowler: Astrophys. J. **173**, 157 (1972)
266. D. Mocelj, T. Rauscher, G. Martínez-Pinedo, Y. Alhassid: In: *Capture Gamma Ray Spectroscopy and Related Topics.* (World Scientific, Singapore 2003) p. 781
267. D. Mocelj, T. Rauscher, G. Martínez-Pinedo, Y. Alhassid: Nucl. Phys. A **718**, 650c (2003)
268. P. Möller et al.: At. Data Nucl. Data Tables **59**, 185 (1995)
269. P. Möller et al.: At. Data Nucl. Data Tables **66**, 131 (1997)
270. P. Möller, J. Randrup: Nucl. Phys. A **514**, 1 (1990)
271. P. Möller et al.: Nature **409**, 785 (2001)
272. P. Mohr, T. Rauscher, H. Oberhummer, Z. Maté, Zs. Fülöp, E. Somorjai, M. Jaeger, G. Staudt: Phys. Rev. C **55**, 1523 (1997)
273. P. Mohr, K.Vogt, M. Babilon et al.: Phys. Lett. B **488**, 127 (2000)
274. P. Mohr, M. Babilon, D. Galaviz, et al: Nucl. Phys. A **719**, 90c (2003)
275. J.A. Morgan: Astrophys. J. **238**, 674 (1980)
276. T. Motobayashi et al.: Phys. Rev. Lett. **73**, 2680-2683 (1994)

277. T. Motobayashi et al.: Phys. Lett. B **264**, 259 (1991)
278. E. Müller, H.-T. Janka: Astron. and Astrophys. **317**, 140 (1994)
279. M.J. Musolf et al.: Phys. Rep. **239**, 1 (1994); J. Ashman et al.: Nucl. Phys. B **328**, 1 (1989)
280. W.D. Myers, W.J. Swiatecki, T. Kodama, L.J. El-Jaick, E.R. Hilf: Phys. Rev. C **15**, 2032 (1977)
281. W.D. Myers, W.J. Swiatecki: Phys. Rev. C **60**, 4606 (1999)
282. S. Nagataki, K. Kohri: Publ. Astron. Soc. Japan **53**, 547 (2001)
283. D.K. Nadyozhin, I.V. Panov: In: *WEIN-92*. ed. T.D. Vylov (World Scientific, Singapore 1993) p. 479
284. H. Nakada, Y. Alhassid: Nucl. Phys. A **718**, 691c (2003)
285. T. Niksic et al.: Phys. Rev. C **66**, 4306 (2002)
286. K. Nomoto et al.: In: *Type Ia Supernovae: Theory and Cosmology*. eds. J. Niemeyer, J.W. Truran (Cambridge Univ. Press 2000) p. 63
287. K. Nomoto, F.-K. Thielemann, S. Miyaji: Astron. and Astrophys. **149**, 239 (1985)
288. P. Nugent et al.: Astrophys. J. **485**, 812 (1997)
289. T. Oda, M. Hino, K. Muto, M. Takahara, K. Sato: At. Data Nucl. Data Tabl. **56**, 231 (1994)
290. R. Oechslin et al.: Phys. Rev. D **65**, 3005 (2002)
291. R. Oechslin, K. Uryu, G. Poghosyan, F.-K. Thielemann: Mon. Not. Roy. Astron. Soc., in press (2004)
292. K. Otsuki et al.: Astrophys. J. **533**, 424 (2000)
293. V. Paar, R. Pezer: Phys. Lett. B **411**, 19 (1997)
294. R.D. Page et al.: Phys. Rev. Lett. **73**, 3066 (1994)
295. R.D. Page, P.J. Woods, R.A. Cunningham, T. Davinson, N.J. Davis, A.N. James, K. Livingston, P.J. Sellin, A.C. Shotter: Phys. Rev. C **49**, 3312 (1994)
296. I.V. Panov et al.: Nucl. Phys. A **688**, 587 (2001); I.V. Panov, S.I. Blinnikov, F.-K. Thielemann: Astron. Lett. **27**, 239 (2001)
297. I.V. Panov, F.-K. Thielemann: Astronomy Letters **29**, 510 (2003); I.V. Panov, F.-K. Thielemann: Nucl. Phys. A **718**, 647 (2003)
298. S. Pastor, G. Raffelt: Phys. Rev. Lett. **89**, 191101 (2002)
299. J.M. Pearson et al.: Phys. Lett. B **387**, 455 (1996)
300. R. Pezer, A. Ventura, D. Vretenar: Nucl. Phys. A **717**, 21 (2003)
301. B. Pfeiffer et al.: Nucl. Phys. A **693**, 282 (2001)
302. J.A. Pons et al.: Astrophys. J. 513, 780 (1999)
303. N. Prantzos, R. Diehl: Phys. Rep. **267**, 1 (1996)
304. W.H. Press, B.P. Flannery, S.A. Teukolsky, W.T. Vetterling: *Numerical Recipes*, (Cambridge University Press 1986)
305. Y.-Z. Qian et al.: Phys. Rev. C **55**, 1532 (1997)
306. Y.-Z. Qian, S.E. Woosley: Astrophys. J. **471**, 331 (1996)
307. Y.-Z. Qian et al.: Astrophys. J. **494**, 285 (1998)
308. Y.-Z. Qian: Astrophys. J. **534**, L67 (2000)
309. M. Rampp, H.T. Janka: Astrophys. J. **539**, L33 (2000)
310. T. Rauscher, J.H. Applegate, J.J. Cowan, F.-K. Thielemann, M. Wiescher: Astrophys. J. **429**, 499 (1994)
311. T. Rauscher et al.: Phys. Rev. C **57**, 2031 (1997)
312. T. Rauscher, F.-K. Thielemann: At. Data Nucl. Data Tables **75**, 1 (2000); **79**, 47 (2001)

313. T. Rauscher et al.: Nucl. Phys. A **675**, 695 (2000)
314. T. Rauscher, A. Heger, R.D. Hoffman et al.: Astrophys. J. **576**, 323 (2002)
315. T. Rauscher, C. Fröhlich, K.H. Guber: In: *Capture Gamma Ray Spectroscopy and Related Topics*, (World Scientific, Singapore 2003) p. 336
316. M. Rayet, N. Prantzos, M. Arnould: Astron. and Astrophys. **227**, 211 (1990)
317. M. Rayet, M. Arnould, M. Hashimoto, N. Prantzos, K. Nomoto: Astr. and Astrophys. **298**, 517 (1995)
318. S. Reddy, M. Prakash, J.M. Lattimer: Phys. Rev. D **58**, 3009 (1998)
319. S. Reddy, M. Prakash, J.M. Lattimer, S.A. Pons: Phys. Rev. C **59**, 2888 (1999)
320. K.E. Rehm et al.: Phys. Rev. C **53**, 1950 (1996)
321. K.E. Rehm et al.: Phys. Rev. Lett. **80**, 676 (1998)
322. P.G. Reinhard et al.: Hyperfine Interactions **127**, 13 (2000)
323. W. Reisdorf: Z. Phys. A **300**, 227 (1981)
324. F. Rembges, C. Freiburghaus, T. Rauscher, F.-K. Thielemann, H. Schatz, M. Wiescher; Astrophys. J. **484**, 412 (1997)
325. J. Ressler et al.: Phys. Rev. Lett. **84**, 2104 (2000)
326. C. Rolfs, W.S. Rodney: *Cauldrons in the Cosmos*, (University of Chicago Press, Chicago 1988)
327. C. Rolfs, H.P. Trautvetter, W.S. Rodney: Rep. Prog. Phys. **50**, 233 (1987)
328. R. Rosner, A. Alexakis, Y.-N. Young, J.W. Truran, W. Hillebrandt: Astrophys. J. **562**, L177 (2001)
329. S. Rosswog et al.: Astron. and Astrophys. **341**, 499 (1999); Astron. and Astrophys. **360**, 171 (2000)
330. S. Rosswog, M.B. Davies: Mon. Not. R. Astron. Soc. **334**, 481 (2002)
331. M. Ruffert, H.-T. Janka: Astron. and Astrophys. **380**, 544 (2001)
332. E.E. Salpeter, H.M. van Horn: Astrophys. J. **155**, 183 (1969)
333. J.M. Sampaio, K. Langanke, G. Marttínez-Pinedo: Phys. Lett. B **511**, 11 (2001)
334. J.M. Sampaio, K. Langanke, G. Martínez-Pinedo, D.J. Dean: Phys. Lett. B **529** (2002) 19
335. M. Samyn, S. Goriely, J.M. Pearson: Nucl. Phys. A **725**, 69 (2003)
336. H. Schatz, A. Aprahamian, J. Görres, M. Wiescher, T. Rauscher, J.F. Rembges, F.-K. Thielemann, B. Pfeiffer, P. Möller, K.-L. Kratz, H. Herndl, B.A. Brown, H. Rebel: Phys. Rep. **294**, 168 (1998)
337. H. Schatz, A. Aprahamian, V. Barnard, L. Bildsten, A. Cumming, M. Ouellette, T. Rauscher, F.-K. Thielemann, M. Wiescher: Phys. Rev. Lett. **86**, 3471 (2001)
338. H. Schatz, L. Bildsten, A. Cummings, M. Wiescher: Astrophys. J. **524**, 1014 (1999)
339. H. Schatz, R. Toenjes, B. Pfeiffer, T. Beers, J.-J. Cowan, V. Hill, K.L. Kratz: Astrophys. J. **579**, 626 (2002)
340. L. Scheck, T. Plewa, H.-T. Janka, K. Kifionidis, E. Müller: Phys. Rev. Lett. **92**, 011103 (2004)
341. H. Schlattl et al.: Phys. Rev. D **60**, 113002 (1999)
342. V. Schönfelder et al.: Astron. and Astrophys. Suppl., **143**, 145 (2000); V. Schönfelder, Nucl. Phys. News **11**, 17 (2001)
343. S. Schramm, S.E. Koonin: Astrophys. J. **365**, 296 (1990)
344. F. Schümann et al.: Phys. Rev. Lett. **90**, 232501 (2003)
345. P.A. Seeger et al.: Astrophys. J. Suppl. **97**, 121 (1965)

346. N.J. Shaviv, G. Shaviv: Astrophys. J. **558**, 925 (2001)
347. J. Shergur et al.: Phys. Rev. C **65**, 034313 (2002)
348. S. Shore et al.: Astrophys. J. **421**, 344 (1994)
349. K. Sonnabend, A. Mengoni, P. Mohr et al.: Nucl. Phys. A **719**, 123c (2003)
350. O. Sorlin et al.: Phys. Rev. Lett. **88**, 092501 (2002)
351. S. Starrfield, C. Iliadis, J.W. Truran, M. Wiescher, W.M. Sparks: Nucl. Phys. A **688**, 110c (2001)
352. S. Starrfield, J.W. Truran, M. Wiescher, W.M. Sparks: Mon. Not. R. Astron. Soc. **296**, 502 (1998)
353. H.E. Suess, H.C. Urey: Rev. Mod. Phys. **28** 53 (1956)
354. K. Sumiyoshi et al.: Astrophys. J. **562**, 880 (2001)
355. R. Surman et al.: Phys. Rev. Lett. **79**, 1809 (1997)
356. A. Staudt, E. Bender, K. Muto, H.V. Klapdor: Z. Phys. A **334**, 47 (1989)
357. A. Staudt, E. Bender, K. Muto, H.V. Klapdor: At. Data Nucl. Data Tables **44**, 79 (1990)
358. A. Staudt, H.V. Klapdor-Kleingrothaus: Nucl. Phys. A **549**, 254 (1992)
359. R.E. Taam, B.A. Fryxell: Astrophys. J. **294**, 303 (1985)
360. R. Taam, S.E. Woosley, T. Weaver, D. Lamb: Astrophys. J. **413**, 324 (1993)
361. M. Takahara, M. Nino, T. Oda, K. Muto, A.A. Wolters, P.W.M. Claudemans, K. Sato: Nucl. Phys. A **504**, 167 (1989)
362. K. Takahashi, M. Yamada, Z. Kondo: At. Data Nucl. Data Tables **12**, 101 (1973)
363. K. Takahashi, K. Yokoi: At. Data Nucl. Data Tables **36**, 375 (1988)
364. K. Takahashi et al.: Astron. and Astrophys. **286**, 857 (1994)
365. J. Taylor: Rev. Mod. Phys. **66**, 711 (1994)
366. J.W. Tepel, H.M. Hoffmann, H.A. Weidenmüller: Phys. Lett. B **49**, 1 (1974)
367. M. Terasawa et al.: Astrophys. J. **578**, L137 (2002)
368. F.-K. Thielemann, D. Argast, F. Brachwitz et al.: Nucl. Phys. A **718**, 139 (2003)
369. F.-K. Thielemann, W.D. Arnett, Astrophys. J. **295**, 604 (1985)
370. F.-K. Thielemann, M. Arnould, W. Hillebrandt: Astron. and Astrophys. **74**, 175 (1979)
371. F.-K. Thielemann, M. Arnould, J. W.Truran: In: *Advances in Nuclear Astrophysics*, ed. E. Vangioni-Flam (Editions Frontière, Gif sur Yvette 1987) p. 525
372. F.-K. Thielemann, F. Brachwitz, P. Höflich, G. Martínez-Pinedo, K. Nomoto: New Astronomy **48**, 65 (2004)
373. F.-K. Thielemann, J. Metzinger, H.V. Klapdor: Z. Phys. A **309**, 301 (1983)
374. F.-K. Thielemann et al.: In: *Fifty Years with Nuclear Fission*, ed. J.W. Behrens, A.D. Carlson (American Nuclear Society,1989) p. 592
375. F.-K. Thielemann, M. Hashimoto, K. Nomoto: Astrophys. J. **349**, 222 (1990)
376. F.-K. Thielemann, K.-L. Kratz, B. Pfeiffer, T. Rauscher, L. van Wormer, M. C. Wiescher: Nucl. Phys. A **570**, 329c (1994)
377. F.-K. Thielemann, K. Nomoto, M. Hashimoto: Astrophys. J. **460**, 408 (1996)
378. F.-K. Thielemann, K. Nomoto, K. Yokoi: Astron. and Astrophys. **158**, 17 (1986)
379. F.-K. Thielemann, J.W. Truran: In *Advances in Nuclear Astrophysics*, eds. E. Vangioni-Flam et al. (Editions Frontières, Gif sur Yvette 1987) p. 541
380. D. Thomas, D.N. Schramm, K.A. Olive, B.D. Fields: Astrophys. J. **406**, 569 (1993)

381. D. Thomas, D.N. Schramm, K.A. Olive: Astrophys. J. **430**, 291 (1994)
382. J. Thomas, M.R. Zirnbauer, K. Langanke: Phys. Rev. C **33**, 2197 (1986)
383. T.A. Thompson et al.: Astrophys. J. **562**, 887 (2001)
384. T.A. Thompson, A. Burrows, P.A. Pinto: Astrophys. J. **592**, 434 (2003)
385. S.E. Thorsett: Phys. Rev. Lett. **77**, 1432 (1996)
386. P. Tischhauser, R.E.Azuma, L. Buchmann, R. Detwiler, U. Giesen, J. Görres, M. Heil, J. Hinnefeld, F. Käppeler et al.: Phys. Rev. Lett. **88**, 072501 (2002)
387. J. Toivanen et al.: Nucl. Phys. A **694**, 395 (2001)
388. V. Trimble: Rev. Mod. Phys. **47**, 877 (1975)
389. V. Trimble: Astron. Astrophys. Rev. **3**, 1 (1991)
390. J.W. Truran: Astrophys. Space Sci. **18**, 308 (1972)
391. J.W. Truran: In: *Essays in Nuclear Astrophysics*, eds. C.A. Barnes, D.D. Clayton, D.N. Schramm (Cambridge University Press, Cambridge 1982) p. 467
392. J.W. Truran: Ann. Rev. Nucl. Part. Sci. **34**, 53 (1985)
393. J.W. Truran, A.G.W. Cameron, A. Gilbert: Can. J. Phys. **44**, 563 (1966)
394. J.W. Truran, J.J. Cowan, A.G.W. Cameron: Astrophys. J. **222**, L63 (1978)
395. H. Umeda, K. Nomoto: Astrophys. J. **565**, 385 (2002)
396. H. Utsunomiya, et al.: Phys. Rev. C **67**, 015807 (2003)
397. G. Vancraeynest et al.: Phys. Rev. C **57**, 2711 (1998)
398. S. van Eck, S. Goriely, A. Jorissen et al.: Nature **412**, 793 (2001)
399. S. van Eck, S. Goriely, A. Jorissen et al.: Astron. and Astrophys. **404**, 291 (2003)
400. L. van Wormer, J. Görres, C. Iliadis, M. Wiescher, F.-K. Thielemann: Astrophys. J. **432**, 326 (1994)
401. R.L. Varner, W.J. Thompson, T.L. McAbee, E.J. Ludwig, T.B. Clegg: Phys. Rep. **201**, 57 (1991)
402. J.J.M. Verbaatschot, H.A. Weidenmüller, M.R. Zirnbauer: Phys. Rep. **129**, 367 (1984)
403. T. von Egidy, A.N. Behkami, H.H. Schmidt: Nucl. Phys. A **376**, 405 (1986)
404. T. von Egidy, H.H Schmidt, A.N. Behkami: Nucl. Phys. A **481**, 189 (1988)
405. M.C. Vetterli et al.: Phys. Rev. C **45**, 997 (1992)
406. D. Vretenar et al.: Phys. Rev. C **63**, 7301 (2001)
407. D. Vretenar, N. Paar, P. Ring, G.A. Lalazissis: Phys. Rev. C **63**, 047301 (2001)
408. D. Vretenar, T. Niksic, P. Ring: Phys. Rev. C **68**, 024310 (2003)
409. R.V. Wagoner: Astrophys. J. Suppl. **18**, 247 (1969)
410. R.A. Wallace, S.E. Woosley: Astrophys. J. Suppl. **45**, 389 (1981)
411. G. Wallerstein et al.: Rev. Mod. Phys. **69**, 995 (1997)
412. S. Wanajo et al.: Astrophys. J. **554**, 578 (2001)
413. R.-P. Wang, F.-K. Thielemann, D.H. Feng, C.-L. Wu: Phys. Lett. B **284**, 196 (1992)
414. M. Wiescher, J. Görres, F.-K. Thielemann, H. Ritter: Astron. and Astrophys. **160**, 56 (1986)
415. M. Wiescher, V. Harms, J. Görres, F.-K. Thielemann, L.J. Rybarcyk: Astrophys. J. **316**, 162 (1987)
416. M. Wiescher, J. Görres: Z. Phys. A **329**, 121 (1988)
417. M. Wiescher, J. Görres, F.-K. Thielemann, Astrophys. J. **326**, 384 (1988)
418. M. Wiescher, J. Görres, F.-K. Thielemann: Astrophys. J. **363**, 340 (1990)
419. M. Wiescher, J. Görres, S. Graaf, L. Buchmann, F.-K. Thielemann: Astrophys. J. **343**, 352 (1989)

420. M. Wiescher, R. Steininger, F. Käppeler: Astrophys. J. **344**, 464 (1989)
421. M. Wiescher, J. Görres, H. Schatz, J. Phys. G: Nucl. Part. Phys. **25**, R133 (1999)
422. M. Wiescher, H. Schatz, A. Champagne: Phil. Trans. Roy. Soc. **356**, 2105 (1998)
423. L. Wilets, B.G. Giraud, M.J. Watrous, J.J. Rehr: Astrophys. J. **530**, 504 (2000)
424. J.R. Wilson: In *Numerical Astrophysics*, ed. by J.M. Centrella, J.M. LeBlanc, R.L. Bowers, (Jones and Bartlett, Boston 1985) p. 422
425. J.R. Wilson: In *Fermi and Astrophysics*, ed. R. Ruffin (Nuovo Cimento, to be published)
426. J.R. Wilson, R.W. Mayle: Phys. Rep. **227**, 97 (1993)
427. J.A. Winger et al.: Phys. Rev. C **48**, 3097 (1993)
428. K. Wisshak, F. Voss, F. Käppeler, I. Kerzakov: Nucl. Phys. A **621**, 270c (1997)
429. S.E. Woosley, W.D. Arnett, D.D. Clayton: Astrophys. J. Suppl. **26**, 231 (1973)
430. S.E. Woosley, W.A. Fowler, J.A. Holmes, B.A. Zimmerman: At. Data Nucl. Data Tables **22**, 371 (1978)
431. S.E. Woosley, D. Hartmann, R.D. Hoffman, W.C. Haxton: Astrophys. J. **356**, 272 (1990)
432. S.E. Woosley, A. Heger, T.A. Weaver: Rev. Mod. Phys. **74**, 1015 (2002)
433. S.E. Woosley, A. Heger, A. Cumming, R.D. Hoffman, J. Pruet, T. Rauscher, J.L. Fisker, H. Schatz, B.A. Brown, M. Wiescher: eprint arXiv:astro-ph/0307425 (2003); Astrophys. J. Suppl. **151**, 75 (2004)
434. S.E. Woosley, R.D. Hoffman: Astrophys. J. **395**, 202 (1992)
435. S.E. Woosley, W.M. Howard: Astrophys. J. Suppl. **36**, 285 (1978)
436. S.E. Woosley et al.: Astrophys. J. **433**, 229 (1994)
437. S.E. Woosley, T.A. Weaver: Ann. Rev. Astron. Astrophys. **24**, 205 (1986)
438. S.E. Woosley, T.A. Weaver: Astrophys. J. Suppl. **101**, 181 (1995)
439. T. Yoshida, M. Terasawa, T. Kajino, K. Sumiyoshi: Astrophys. J. **600**, 204 (2004)
440. Z. Zhao, R.H. France, K.S. Lai, S.L. Rugari, M. Gai, E.L. Wilds: Phys. Rev. Lett. **70**, 2066 (1993)
441. Z. Zhao, R.H. France, K.S. Lai, S.L.Rugari, M. Gai, E.L. Wilds, R.A. Kryger, J.A. Winger, K.B. Beard: Phys. Rev. C **48**, 429 (1993)
442. A. Zilges, S. Volz, M. Babilon, T. Hartmann, P. Mohr, K. Vogt: Phys. Lett. B **542**, 43 (2002)